7. SITE 900[1]

Shipboard Scientific Party[2]

HOLE 900A

Date occupied: 10 May 1993

Date departed: 22 May 1993

Time on hole: 11 days, 20 hr, 15 min

Position: 46°40.994'N, 11°36.252'W

Bottom felt (rig floor; m, drill-pipe measurement): 5048.5

Distance between rig floor and sea level (m): 11.72

Water depth (drill-pipe measurement from sea level, m): 5036.8

Total depth (rig floor; m): 5853.50

Penetration (m): 805.00

Number of cores (including cores having no recovery): 86

Total length of cored section (m): 805.0

Total core recovered (m): 519.61

Core recovery (%): 65

Oldest sediment cored:
Depth (mbsf): 739.86
Nature: claystone
Age: late Paleocene
Measured velocity (km/s): 2.40

Hard rock:
Depth (mbsf): 748.90
Nature: altered mafic igneous rocks
Measured velocity (km/s): 5.8

Principal results: Site 900 is situated in the Iberia Abyssal Plain within the ocean/continent transition (OCT) zone over an angular basement high that has some similarity to a tilted fault block. Geophysical modeling had indicated that this basement high lay within a part of the OCT having a very weak magnetization and thus was probably thinned continental crust. The site was one of a transect of sites across the OCT designed to study the petrologic changes in the basement rocks within the OCT to identify the processes that accompanied continental breakup and the onset of steady-state seafloor spreading. Cores were obtained from a hole that penetrated 748.9 m of Pleistocene to Paleocene sediments and 56.1 m of basement composed of retrograde metamorphosed mafic igneous rocks. Coring was terminated when the rate of penetration came close to 1 m/hr and bit failure was imminent. A total of 380 m of sonic, resistivity, and FMS logs was acquired from three separate intervals in the sediments and basement.

1. Basement is composed of mafic igneous rocks that underwent retrograde metamorphism to greenschist to amphibolite-grade facies. The history of these rocks is unclear at present; they may have originated as Paleozoic intrusive or metamorphic rocks, or pre-late Paleocene continental crust or subcontinental mantle that was invaded by gabbro. In any case, they were exposed at the seafloor prior to the late Paleocene, probably by Early Cretaceous rifting.

2. A 4-m.y. hiatus during middle/late Miocene time, which began at 11.7 Ma, is correlatable with a regional angular unconformity in seismic reflection profiles and may be related to northwest-southeast compression on this margin during a compressional phase in the formation of the Betic Mountains in southern Spain and structural inversion in the Lusitanian Basin of Portugal.

Two lithostratigraphic units were identified at Site 900.

1. Subunit IA (0-67.2 mbsf) is a Pleistocene to late Pliocene age nannofossil clay, clay, and nannofossil ooze. The subunit mainly consists of mud-dominated turbidites and hemipelagic/pelagic sediments.

Subunit IB (67.2-96.0 mbsf) is a late Pliocene to late Miocene age nannofossil claystone and nannofossil chalk. The subunit consists mainly of hemipelagic/pelagic sediments.

Subunit IC (96.0-181.5 mbsf) is a late Miocene to late early Miocene age nannofossil claystone, claystone, and nannofossil chalk with minor siltstone and fine sandstone. The subunit consists mostly of mud-dominated turbidites and hemipelagic/pelagic sediments.

2. Subunit IIA (181.5-234.3 mbsf) is an early Miocene age nannofossil claystone and chalk, with claystone and minor silty claystone to fine sandstone. The subunit consists mainly of contourites and turbidites with pelagic/hemipelagic sediments.

Subunit IIB (234.3-748.9 mbsf) is an early Miocene to Paleocene age silty claystone to clayey siltstone, nannofossil claystone, and claystone with calcareous silty claystone to clayey siltstone, siltstone, and fine sandstone. The subunit consists mainly of sediments, possibly including turbidites reworked by contour currents.

The sediments at this site reveal the history of development of the lower continental rise adjacent to the Iberia Abyssal Plain during Cenozoic time. The cores chronicle the deposition of silt and clay layers with laminated bases under the influence of bottom currents, which were probably contour-following currents and part of the general oceanic circulation. Mud turbidites were occasionally seen, too. These sediments were succeeded by carbonate-rich turbidites and then by mud-dominated turbidites as the abyssal plain sediments built upward and sideways onto the rise.

The cores provide a discontinuous fossil record from Pleistocene through late Paleocene time. Calcareous nannofossils generally are abundant to very abundant. Planktonic foraminifers generally are common to abundant in the upper section of the hole, but samples from the deeper sections contained fewer specimens. Two major hiatuses representing the early late Miocene and the early Eocene, as well as several minor hiatuses, have been identified.

The Matuyama, Gauss, and Gilbert chrons tentatively were identified from paleomagnetic measurements of the sediments above 145 mbsf. Below that depth, the sediments are very weakly magnetized and no chrons have been identified. The metamorphic basement rocks do not provide any reliable magnetic results, mainly because of weak magnetization. Magnetic susceptibility values generally follow the pattern of remanent magnetization values in both sediments and crystalline rocks.

Fifty-six meters of fine- to coarse-grained metamorphosed mafic rocks were drilled in the basement. The rocks are highly deformed and brecciated and veined by later calcite, epidote, and clinozoisite. A porphyroclastic texture having large porphyroclasts of plagioclase and clinopyroxene in a recycled matrix of the same minerals can be seen in thin section. Chemical

[1] Sawyer, D.S., Whitmarsh, R.B., Klaus, A., et al, 1994. *Proc. ODP, Init. Repts.,* 149: College Station, TX (Ocean Drilling Program).

[2] Shipboard Scientific Party is as given in list of participants preceding the contents.

Reproduced online: 15 October 2004.

analyses suggest that the rocks are relatively depleted in large ionic lithophile elements. These rocks may be (1) Paleozoic mafic rocks that were accreted onto continental basement during the Hercynian orogeny, (2) Cumulate gabbro (of any pre-late-Paleocene age) either formed in, or possibly underplated at the base of, continental crust. The rocks subsequently experienced a series of deformation and metamorphic events. In any case, they were exposed at the seafloor prior to the late Paleocene, probably by the Early Cretaceous rifting.

The sonic, resistivity, and Formation Microscanner (FMS) logging strings were run over three separate parts of the hole, including 36 m of basement. Hole conditions made logging difficult and forced us to use the conical side-entry sub. Eventually, logging had to be abandoned because of persistent obstructions in the hole and damage to the logging cable and FMS tool.

Measurements of physical properties in the sediments indicate a small but steady increase in bulk density, seismic velocity, formation factor, shear strength, and thermal conductivity, and a concomitant decrease in porosity with depth. The clay-rich sediments were notable for their significant seismic anisotropy in places (more than 7%) and relatively strong vertical velocity gradient (1 s^{-1}), compared to that at Sites 897, 898 and 899. The density of the basement rocks is about 2.6 to 2.9 g/cm^3, and their velocity ranges from 3.7 to 7.5 km/s, with a cluster of observations at 5.7 km/s.

Interstitial-water samples were obtained from lithologic Units I and II (13-722 mbsf). The principal result is a steady downward decrease in concentrations of sulfate throughout the hole, from a value near that of seawater concentration at 13 mbsf to a minimum of 1.9 mM at 702 mbsf. The profile is slightly convex upward, suggesting that some sulfate reduction has occurred within the sedimentary column. Concentrations of ammonia are consistent with this interpretation. A similarly shaped magnesium profile may result from clay mineral alteration. Concentrations of calcium and strontium suggest carbonate recrystallization at about 300 mbsf and below 636 mbsf.

Profiles of carbonate content vs. depth reflect a history of generally low biological productivity and deposition of hemipelagic sediments below the carbonate compensation depth (CCD), combined with delivery by turbidites of carbonate-rich material initially deposited above the CCD. An average 0.3% organic carbon was found in Unit I; this is much less than that found at Sites 897 and 898. Variable organic C/N ratios from Unit I indicate the fluctuating predominance of marine or terrigenous sources of organic matter. Concentrations of biogenic methane encountered in headspace gas analyses of lithostratigraphic Unit I to Subunit IIB generally are low, as were those found at Site 899. Methanogenesis may have been inhibited by interstitial sulfate, as indicated by the generally high sulfate concentrations in the pore waters.

BACKGROUND AND SCIENTIFIC OBJECTIVES

Site 900 (Fig. 1, "Site 897" chapter, this volume) was one of a series of sites drilled during Leg 149 to elucidate the nature of the top of the crust (acoustic basement) within the ocean/continent transition (OCT) beneath the Iberia Abyssal Plain. The regional background for this and the other Leg 149 sites is presented elsewhere (see "Introduction" chapter, this volume; Whitmarsh et al., 1990,1993). Site 900 is located about 23 nmi (43 km) east of Site 898, about 25 nmi (46 km) southwest of Vasco da Gama Seamount and 45 nmi (83 km) west-southwest of Site 398 (see Fig. 1 in "Introduction" chapter, this volume, and "Site Geophysics" section, this chapter). Site 900 was chosen to sample a basement high located near the western edge of a region of weakly magnetized, thinned continental crust that appears to extend from the OCT to the continental slope (see Fig. 4 in "Introduction" chapter, this volume). The basement high under the site is angular and only slightly asymmetric in profile, but appears as an isolated almost circular feature in plan view (Fig. 2 in "Site 897" chapter, this volume). We had interpreted the high as a fault block of continental crust. Should the acoustic basement under the site prove to be continental, then the almost 200-km-wide region of crust between the site and the base of the Portuguese continental slope might logically also be assigned a continental origin. Further, assuming symmetrical rifting, one could argue that a wide area of thinned continental crust might also exist under the conjugate Newfoundland margin, where conflicting views exist regarding the extent of thinned continental crust (Keen and de Voogd, 1988; Tucholke et al., 1989).

By analogy with Site 398, we expected to encounter ooze/chalk with turbidites over chalk, mudstone, and claystone (Sibuet, Ryan, et al., 1979). Seismic-reflection profiles traced back to Site 398 indicated that the basal sediments would be as old as Paleocene. The regional unconformity, which resulted from gentle folding that occurred during the Miocene northwest-southeast Rif-Betic compressional phase in southern Spain and North Africa, is not clearly seen in reflection profiles across the site. This may be because it is obscured by two unusual acoustic facies; the interval from 0 to 0.38 s two-way traveltime consists of hummocky sediment waves and the interval from 0.38 to 0.58 s two-way traveltime consists of a series of inclined reflectors (Fig. 1). The sediments thicken to about 1.7 s two-way traveltime (1.9 km) in the basin west of the site and to at least 2.3 s two-way traveltime (3.0 km) to the east. Although we anticipated that acoustic basement at Site 900 might contain continental rocks, the exact petrology of these rocks and the amount of any pre-rift sediments were completely unknown. Phyllites and meta-arkoses of unknown age have been dredged about 20 nmi (37 km) north of the site (Dredge C56-09; Capdevila and Mougenot, 1988).

OPERATIONS

Hole 900A

After completing drilling at Site 899, we moved the ship to 40°41.00'N, 11°36.25'W, Site 900 (IAP-5), and deployed a Datasonics beacon. The precision depth recorder indicated a water depth of 5045.4 mbsl. After the ship was stabilized in dynamic positioning mode over the primary beacon, a second backup Datasonics beacon was deployed.

A rotary core barrel (RCB) bottom-hole assembly (BHA) having a mechanical bit release (MBR) was assembled and run to the seafloor. The bit was positioned at 5048.5 mbrf, and Hole 900A was spudded at 0605 hr Universal Time Coordinated (UTC), 11 May 1993, by advancing 1.5 m. From Core 149-900A-1R, 1.36 m was recovered; therefore, the seafloor was assigned a depth of 5048.5 mbrf. Cores 149-900A-1R to -86R were taken from 5048.5 to 5853.5 mbrf (0-805.0 mbsf; Table 1), with 805.0 m cored and 519.61 m recovered (65% recovery). The first three cores were taken without rotating or pumping seawater; the weight-on-bit, rotation speed, and pump rate gradually were increased in response to increasing formation hardness and for maintaining good hole conditions and core recovery. The water sampler and temperature probe (WSTP) was successfully run at 5170.9 mbrf (122.4 mbsf), 5219.1 mbrf (170.6 mbsf), and 5267.3 mbrf (218.8 mbsf).

We conducted two wiper trips in the sedimentary section. The first was after Core 149-900A-39R, when we moved the pipe between 5412.0 to 5196.6 mbrf (363.7-148.1 mbsf). A second wiper trip was made after Core 149-900A-75R, when we moved the pipe between 5758.8 and 5600.0 mbrf (710.3-551.5 mbsf). We encountered a bridge at 5747.0 mbrf, washed and rotated the bit past it to total depth, and found no fill in the bottom of the hole.

Metamorphic basement rocks were encountered at 748.9 mbsf. After Core 149-900A-86R (805.0 mbsf), suspecting imminent failure of the bit, we decided to stop coring and prepare for logging. The hole was circulated clean, and a short trip was made to 5187 mbrf. Minor overpull was observed while pulling up, and the tight sections were reamed out while moving the pipe down. We then circulated clean the 10 m of fill at the bottom of the hole. The bit was released, and the end of the pipe was pulled to 5185.4 mbrf (136.9 mbsf) for logging.

Two logging runs were made. During the first run (dual induction tool [DIT], caliper tool [MCD], dipole shear imager [DSI], and natural gamma-ray spectrometry tool [NGT-C]), the tool would not pass 5286 mbrf (237.5 mbsf). The drill pipe was repositioned at 5378.5 mbrf (330.0 mbsf). No obstructions or drag were noted while running the drill string farther into the hole. The first logging combination was

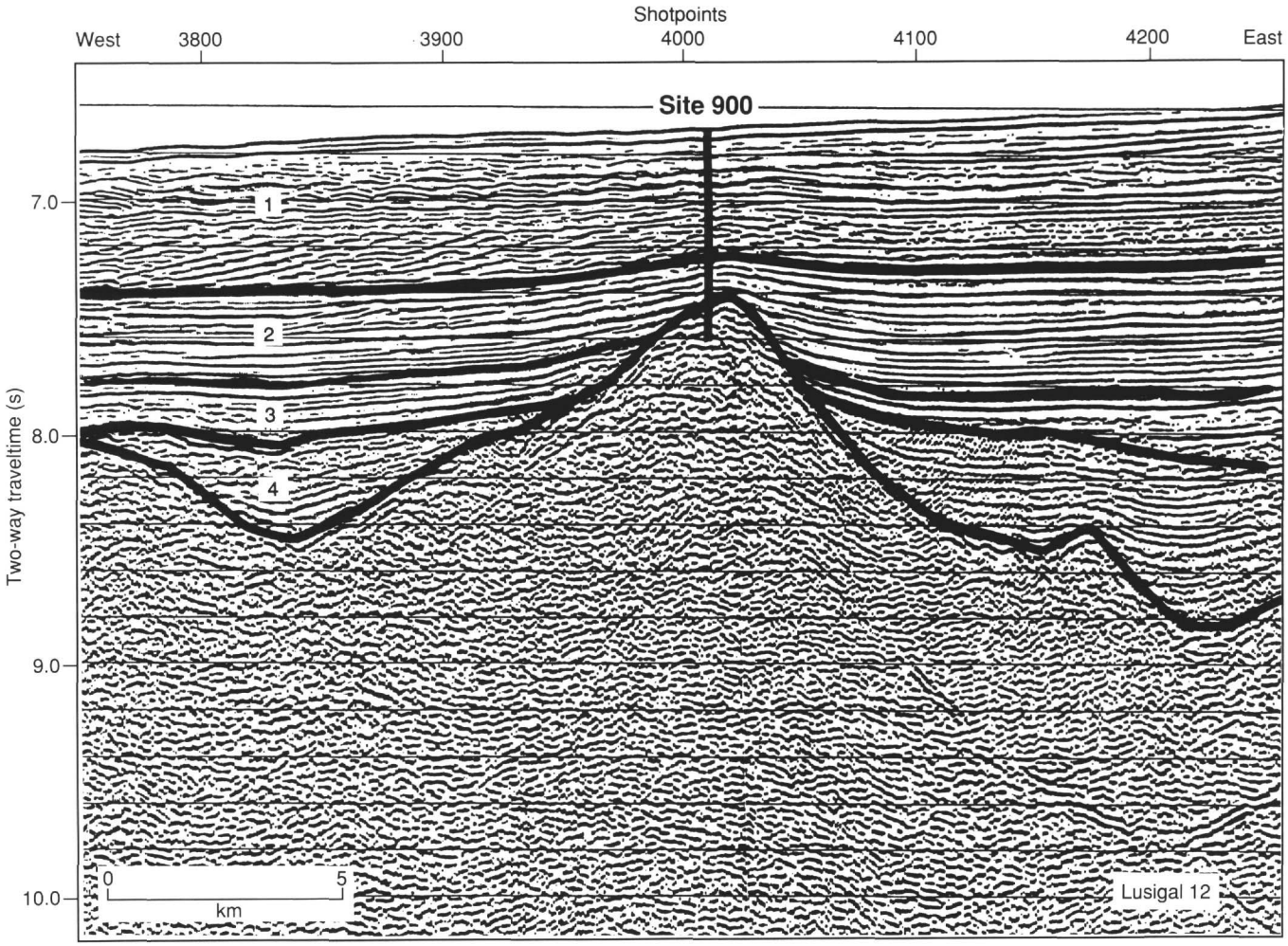

Figure 1. East-west Lusigal 12 multichannel seismic-reflection profile across Site 900 (see Fig. 2 for location). Thick vertical line indicates penetration of the borehole. Vertical exaggeration is about 5:1.

rerun; however, it would not pass 5500 mbrf (451.5 mbsf). After the logs were run, we pulled the drill pipe up to 5244 mbrf (195.5 mbsf) and picked up the conical side-entry sub (CSES).

A tool combination that included the Formation Microscanner (FMS) and NGT-C was loaded into the CSES, and the drill string was run to 5802.2 mbrf (753.7 mbsf); however, the tool would not pass 5837 mbrf (788.5 mbsf). The pipe was pulled up to 5742 mbrf (693.5 mbsf) in an effort to get above the collapsed hole. The combination was rerun from 5837 to 5695 mbrf (788.5-646.5 mbsf). The tool became stuck at 5695 mbrf (646.5 mbsf). The drill string was washed down to 5698 mbrf (649.5 mbsf) over the stuck tool. The logging tool came free, and the drill string and tool were pulled to 5528.9 mbrf (480.4 mbsf). This combination was run again and became stuck at 5613 mbrf (564.5 mbsf). We washed the drill pipe over the tool from 5528 to 5614 mbrf (478.5-565.5 mbsf). At this point, we abandoned logging because of poor hole conditions and damage to the logging cable and FMS tool. We recovered the drill string, recalled the two beacons, and terminated operations at Site 900 at 1518 hr, 22 May 1993.

SITE GEOPHYSICS

Geophysical Data near Site 900

Two migrated multichannel seismic-reflection profiles pass through Site 900 (Fig. 2). They are the north-south Sonne Line 75-21

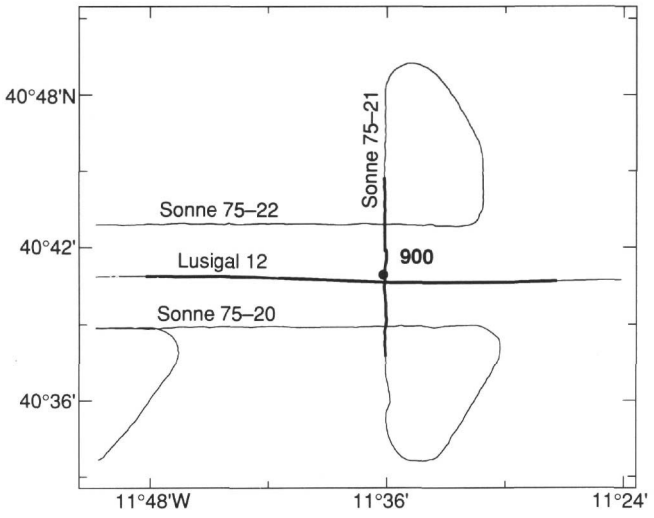

Figure 2. Track chart of multichannel seismic reflection profiles near Site 900. The bold lines indicate the portions of Lusigal Line 12 and Sonne Line 75-21 shown in Figures 1 and 3, respectively.

Table 1. Coring summary for Site 900.

Core no.	Date (1993)	Time (UTC)	Depth (mbsf)	Length cored (m)	Length recovered (m)	Recovery (%)
149-900A-						
1R	May 11	0515	0.0–1.5	1.5	1.36	90.6
2R	May 11	0630	1.5–11.1	9.6	0.45	4.7
3R	May 11	0730	11.1–20.8	9.7	2.29	23.6
4R	May 11	0835	20.8–30.4	9.6	6.99	72.8
5R	May 11	0945	30.4–40.0	9.6	7.02	73.1
6R	May 11	1105	40.0–49.6	9.6	9.01	93.8
7R	May 11	1230	49.6–59.3	9.7	8.22	84.7
8R	May 11	1345	59.3–64.5	5.2	4.06	78.1
9R	May 11	1450	64.5–74.1	9.6	3.66	38.1
10R	May 11	1605	74.1–83.7	9.6	6.19	64.5
11R	May 11	1735	83.7–93.4	9.7	6.58	67.8
12R	May 11	1900	93.4–103.0	9.6	4.92	51.2
13R	May 11	2015	103.0–112.7	9.7	0.03	0.3
14R	May 11	2150	112.7–122.4	9.7	9.69	99.9
15R	May 12	0110	122.4–132.0	9.6	5.18	53.9
16R	May 12	0230	132.0–141.6	9.6	8.88	92.5
17R	May 12	0410	141.6–151.3	9.7	3.85	39.7
18R	May 12	0535	151.3–160.9	9.6	6.69	69.7
19R	May 12	0700	160.9–170.6	9.7	2.40	24.7
20R	May 12	1055	170.6–180.3	9.7	9.84	101.0
21R	May 12	1230	180.3–189.9	9.6	8.74	91.0
22R	May 12	1415	189.9–199.5	9.6	8.62	89.8
23R	May 12	1600	199.5–209.2	9.7	9.59	98.8
24R	May 12	1740	209.2–218.8	9.5	8.86	93.2
25R	May 12	2110	218.8–228.4	9.6	8.77	91.3
26R	May 12	2240	228.4–238.1	9.7	8.19	84.4
27R	May 13	0010	238.1–247.8	9.7	8.61	88.7
28R	May 13	0135	247.8–257.5	9.7	9.04	93.2
29R	May 13	0255	257.5–267.1	9.6	9.02	93.9
30R	May 13	0425	267.1–276.7	9.6	8.90	92.7
31R	May 13	0540	276.7–286.4	9.7	8.21	84.6
32R	May 13	0655	286.4–296.0	9.6	8.05	83.8
33R	May 13	0810	296.0–305.6	9.6	9.58	99.8
34R	May 13	0935	305.6–315.3	9.7	5.61	57.8
35R	May 13	1115	315.3–324.9	9.6	6.84	71.2
36R	May 13	1250	324.9–334.5	9.6	8.67	90.3
37R	May 13	1415	334.5–344.2	9.7	8.31	85.7
38R	May 13	1555	344.2–353.8	9.6	8.55	89.0
39R	May 13	1730	353.8–363.5	9.7	8.81	90.8
40R	May 13	2205	363.5–373.2	9.7	8.54	88.0
41R	May 14	0010	373.2–382.9	9.7	9.15	94.3
42R	May 14	0230	382.9–392.6	9.7	8.94	92.1
43R	May 14	0435	392.6–402.3	9.7	9.14	94.2
44R	May 14	0635	402.3–412.0	9.7	7.22	74.4
45R	May 14	0830	412.0–421.6	9.6	7.75	80.7
46R	May 14	1030	421.6–431.1	9.5	9.07	95.5
47R	May 14	1250	431.1–440.6	9.5	8.96	94.3
48R	May 14	1455	440.6–450.2	9.6	9.31	97.0
49R	May 14	1725	450.2–459.9	9.7	9.84	101.0
50R	May 14	1930	459.9–469.6	9.7	7.77	80.1
51R	May 14	2150	469.9–479.2	9.3	8.72	93.7
52R	May 14	2355	479.2–488.9	9.7	8.44	87.0
53R	May 15	0150	488.9–498.6	9.7	8.85	91.2
54R	May 15	0345	498.6–508.3	9.7	5.59	57.6
55R	May 15	0540	508.3–518.0	9.7	0.00	0.0
56R	May 15	0735	518.0–527.6	9.6	7.08	73.7
57R	May 15	0940	527.6–537.2	9.6	8.08	84.1
58R	May 15	1145	537.2–546.9	9.7	4.45	45.9
59R	May 15	1355	546.9–556.6	9.7	9.10	93.8
60R	May 15	1605	556.6–566.2	9.6	7.35	76.5
61R	May 15	1830	566.2–575.9	9.7	5.72	58.9
62R	May 15	2100	575.9–585.6	9.7	3.57	36.8
63R	May 15	2310	585.6–595.1	9.5	2.67	28.1
64R	May 16	0130	595.1–604.6	9.5	3.06	32.2
65R	May 16	0400	604.6–614.1	9.5	2.87	30.2
66R	May 16	0650	614.1–623.8	9.7	2.99	30.8
67R	May 16	0905	623.8–633.4	9.6	3.81	39.7
68R	May 16	1130	633.4–643.1	9.7	4.67	48.1
69R	May 16	1425	643.1–652.7	9.6	3.24	33.7
70R	May 16	1735	652.7–662.4	9.7	2.80	28.8
71R	May 16	2040	662.4–672.1	9.7	4.13	42.6
72R	May 16	2345	672.1–681.7	9.6	2.90	30.2
73R	May 17	0250	681.7–691.4	9.7	3.37	34.7
74R	May 17	0600	691.4–701.1	9.7	2.54	26.2
75R	May 17	0845	701.1–710.4	9.3	2.68	28.8
76R	May 17	1515	710.4–720.0	9.6	2.86	29.8
77R	May 17	1910	720.0–729.7	9.7	3.65	37.6
78R	May 17	2235	729.7–739.4	9.6	2.28	23.7
79R	May 18	0250	739.4–748.9	9.5	0.46	4.8
80R	May 18	0900	748.9–758.5	9.6	2.13	22.2
81R	May 18	1425	758.5–767.8	9.3	2.67	28.7
82R	May 18	2025	767.8–774.0	6.2	6.23	100.0
83R	May 19	0010	774.0–777.5	3.5	3.08	88.0
84R	May 19	0735	777.5–786.7	9.2	4.98	54.1
85R	May 19	1710	786.7–795.7	9.0	7.88	87.5
86R	May 20	0215	795.7–805.0	9.3	0.74	8.0
Coring totals				805.0	519.61	64.6

(Fig. 3), and the east-west Lusigal Line 12 (see Fig. 1). Site 900 is located over a basement high that is 14 km wide on Lusigal Line 12 (west to east) and 10 km wide on Sonne Line 75-21 (south to north). The high is triangular in west-east cross section (Fig. 1). The apparent dip of the basement on the west side of the high is 7° and on the east side of the high is 16°. At its shallowest known point, the top of the high is at 750 ms two-way traveltime below the seafloor or 720 mbsf. Site 900 is located slightly to the west of the top of the basement high, where the basement is predicted to be at 770 mbsf. Sediments thought to be Paleocene in age cover the basement high; older sediments onlap this high, and the basin section to the east is thicker than that to the west. The sedimentary section at Site 900 consists of three main seismic units (Fig. 1). The, topmost unit (0-380 ms two-way traveltime below seafloor, 0-360 mbsf) consists of discontinuous undulating reflectors. The second unit (380-580 ms two-way traveltime below seafloor, 360-540 mbsf) consists of parallel inclined reflectors that dip to the west or southwest. We mapped the regional distribution of these inclined reflectors during Leg 149 (Fig. 4, "Site 898" chapter, this volume). The third unit (580-800 ms two-way traveltime below seafloor, 540-770 mbsf) consists of parallel, continuous, high-amplitude reflectors.

A magnetic anomaly map (Fig. 7, "Site 897" chapter, this volume; P.R. Miles, J. Verhoef, and R. MacNab, pers. comm., 1993) shows that Site 900 is located on the western side of a roughly circular, about 20-km diameter, magnetic anomaly low. Beslier et al. (1993) and Whitmarsh, Miles, and Mauffret (1990) interpreted seismic and magnetic data, respectively, to indicate that Site 900 is located over extended continental crust.

LITHOSTRATIGRAPHY

Introduction

Hole 900A penetrated a 749-m-thick sedimentary succession consisting of a lower carbonate-rich contourite-turbidite-pelagite sequence (Unit II) and an upper turbidite-pelagite sequence (Unit I). The two sequences contrast sharply in terms of evidence for reworking by contour currents (which is present only in the lower sequence) and in the abundance of siliceous allochems (which are virtually absent in the upper sequence). In the light of the results at Site 900, the shipboard sedimentologists realised that they could recognize the same twofold division at Sites 897, 898, and 899 as summarized in Figure 4.

Rotary coring (RCB) was employed in Hole 900A. Coring began at the seafloor in Unit I and penetrated basement rocks at 748.9 mbsf at the base of Unit II. Figure 5 summarizes the core recovery, lithologies, and ages of the lithostratigraphic units recognized in Hole 900A. The ages, averaged lithologic compositions, overall colors, facies and depositional environments, boundary depths, and cored intervals of Units I and II are summarized in Table 2; Tables 3 and 4 show the color variations exhibited by the lithologies in Units I and II, respectively.

Unit I, though containing turbiditic and hemipelagic/pelagic facies, contains little siliciclastic sand in comparison to its counterparts at Sites 897, 898, and 899. The unit is divided into three subunits. Subunits IA and IC contain turbiditic and hemipelagic/pelagic sediments and are separated by hemipelagic/pelagic nannofossil clays and oozes that comprise Subunit IB.

Unit II is more indurated than Unit I and is dominated by claystone, claystone with silt/silty claystone, nannofossil claystone, and

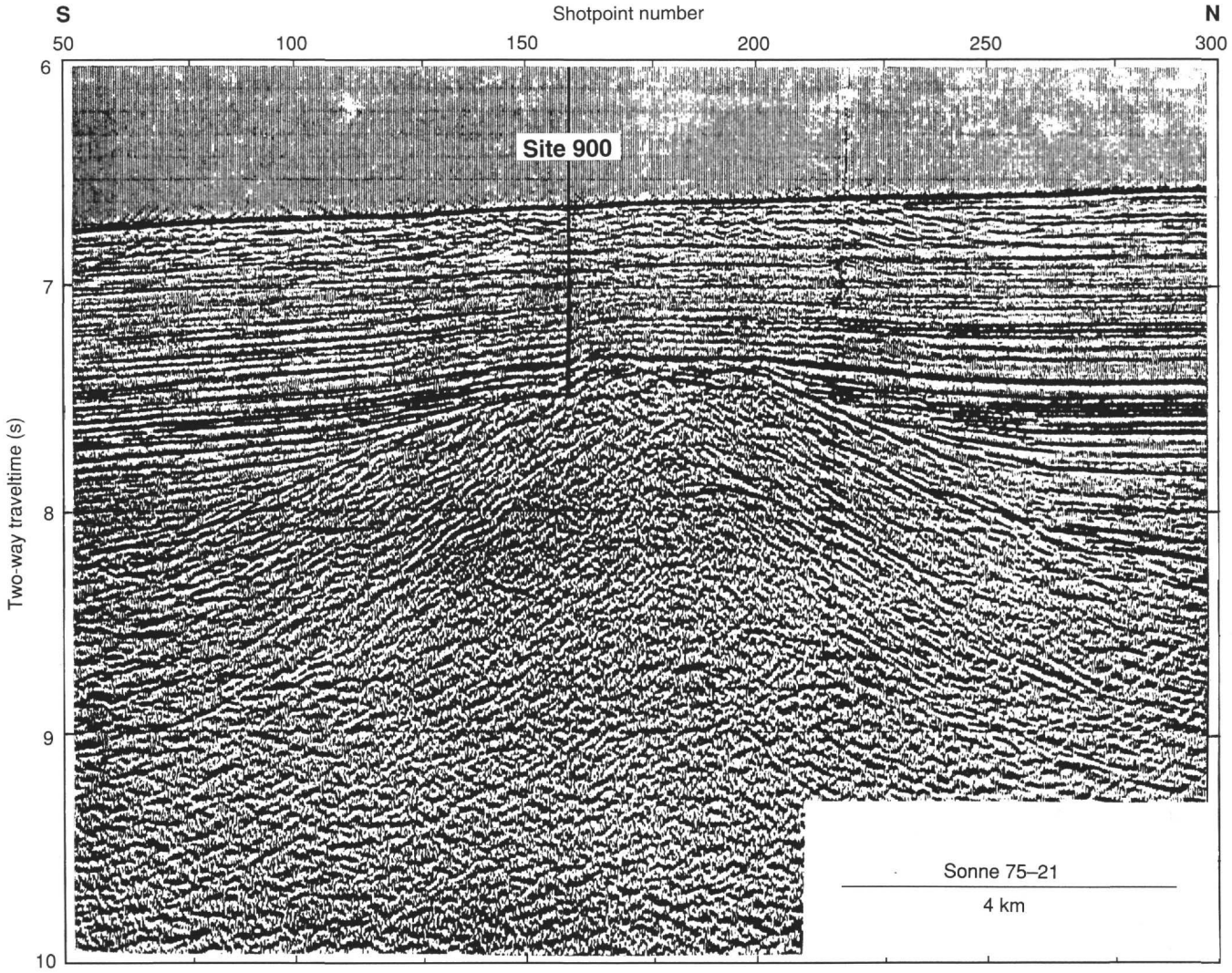

Figure 3. Migrated multichannel seismic profile Sonne Line 75-21 near Site 900. The location of this profile is shown in Figure 2. The location of Site 900 is indicated by vertical line. Vertical exaggeration is about 3:3.

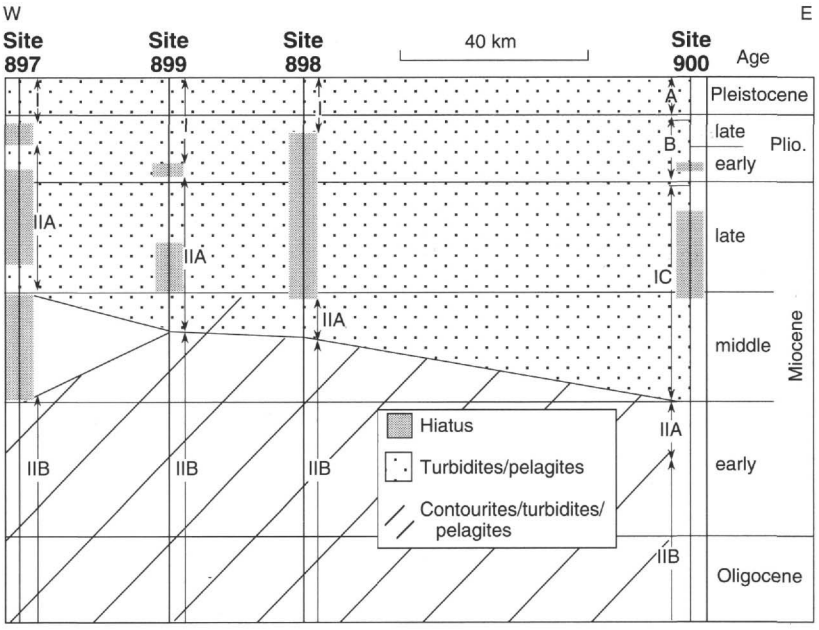

Figure 4. Regional stratigraphic correlation chart for Sites 897 to 900. The lower contourite-turbidite-pelagite sequence contains abundant siliceous allochems and reworked carbonate grains. The upper turbidite-pelagite sequence shows no evidence of reworking by contour currents.

Table 2. Lithostratigraphic summary for Site 900.

Unit	Age	Thickness (m)	Lithology	Percentage (%)	Color	Facies and *environment* (total meters described)	Intervals (mbsf)	Occurrence
IA	Pleistocene to late Pliocene	67.2	Nannofossil ooze Nannofossil clay Clay Silt and fine sand	21 48 30 1	Brown at top; olive gray, greenish gray	Mud dominated turbidites and hemipelagic/pelagic *Base of continental rise* (42.12)	0.0 to 67.2	1R-1, 0 cm, to 9R-2, 122 cm
IB	late Pliocene to late Miocene	28.8	Nannofossil ooze Nannofossil clay Clay	50 49 1	Pale orange, moderate brown	Hemipelagic/pelagic *Base of continental rise* (16.31)	67.2 to 96.0	9R-2, 122 cm, to 12R-2, 110 cm
IC	late Miocene to late early Miocene	85.5	Nannofossil ooze Nannofossil clay Clay Silt and fine sand	23 48 25 4	Gray, yellow brown,olive gray,greenish gray	Mud dominated turbiditesand hemipelagic/ pelagic *Base of continental rise* (50.13)	96.0 to 181.5	12R-2, 110 cm, to 21R-1, 125 cm
IIA	early Miocene	52.75	Nannofossil chalk Nannofossil claystone Claystone Silty clayst. to clayey siltst. Siltstone and fine sandstone	24 45 17 8 6	Gray, greenish gray	Contourites/turbidites Hemipelagic/pelagic *Base of continental rise/ Edge of abyssal plain* (49.18)	181.5 to 234.3	21R-1, 125 cm, to 26R-4, 135 cm
IIB	early Miocene to Paleocene	514.61	Nannofossil chalk Nannofossil claystone Claystone Calc. silty clayst. to clayey siltst. Silty clayst. to clayey siltst. Silt and fine sandstone	<1 24 22 15 27 11	Greenish gray Moderate brown Yellowish brown	Contourites/turbidites Hemipelagic/pelagic *Base of continental rise/ Edge of abyssal plain* (334.16)	234.3 to 748.9	26R-4, 135 cm, to 79R-CC

Table 3. Summary of colors exhibited by lithologies in Unit I at Site 900.

Color	Munsell code	Sand	Silty sand	Sandy silt; silt	Clayey silt; silty clay	Clay	Calcareous or Nannofossil clay/silty clay	Nannofossil clay	Nannofossil ooze
White	N2,3			●			#		#
Dark gray	N4	●	●		●				
Medium light gray	N6						o ●		
Light gray	N7						o ●		o
Very light gray	N8								●
Dark yellowish brown	10YR 4/2	o							●
Mod. yellowish brown	10YR 5/4							o #	#
Yellowish brown	10YR 5/2							o	
Pale yellowish brown	10YR 6/2							●	●
Very pale orange	10YR 8/2							#	#
Reddish orange	5YR 4/2							#	#
Olive black	5Y 2/1		●						
Olive gray	5Y 4/1		●	o	o	o ●		o ●	
Light olive gray	5Y 5/1,5/2				●		o ●		
Light olive gray	5Y 6/1							o ●	o
Yellowish gray	5Y 8/1							o # ●	o #
Greenish black	5GY 2/1			●					
Dark greenish gray	5GY 4/1	o	o ●		o	●		●	
Greenish gray	5GY 5/1	●				●			
Greenish gray	5GY 6/1							●	
Greenish black	5G 2/1,2/2			●					
Dark greenish gray	5G 4/1					●			
Greenish gray	5G 6/1,7/1				●		●		
Light greenish gray	5G 7/1,8/1						●		

Note: Subunit IA = o; Subunit IB = #; Subunit IC = ●.

nannofossil chalk. Foraminifer-rich sandstones and calcarenites occur as a distinctive minor lithology in Subunit IIA, and form up to 20% to 30% of some cores in Subunit IIB, where they are often calcite-cemented. Both subunits contain upward-darkening sequences of nannofossil claystone and claystone/calcareous claystone with silt, sometimes with siliciclastic/bioclastic sandy bases. Upward-lightening sequences also are present in Subunit IIA. Both subunits are interpreted as the deposits of turbidity flows and contour currents.

Figure 6 is a plot of ages vs. depths presented in Table 5 for the sedimentary sequence penetrated at Site 900. Sediment accumulation rates, generalized from Figure 6, show less variation between Units I and II than rates observed for the corresponding lithostratigraphic units and

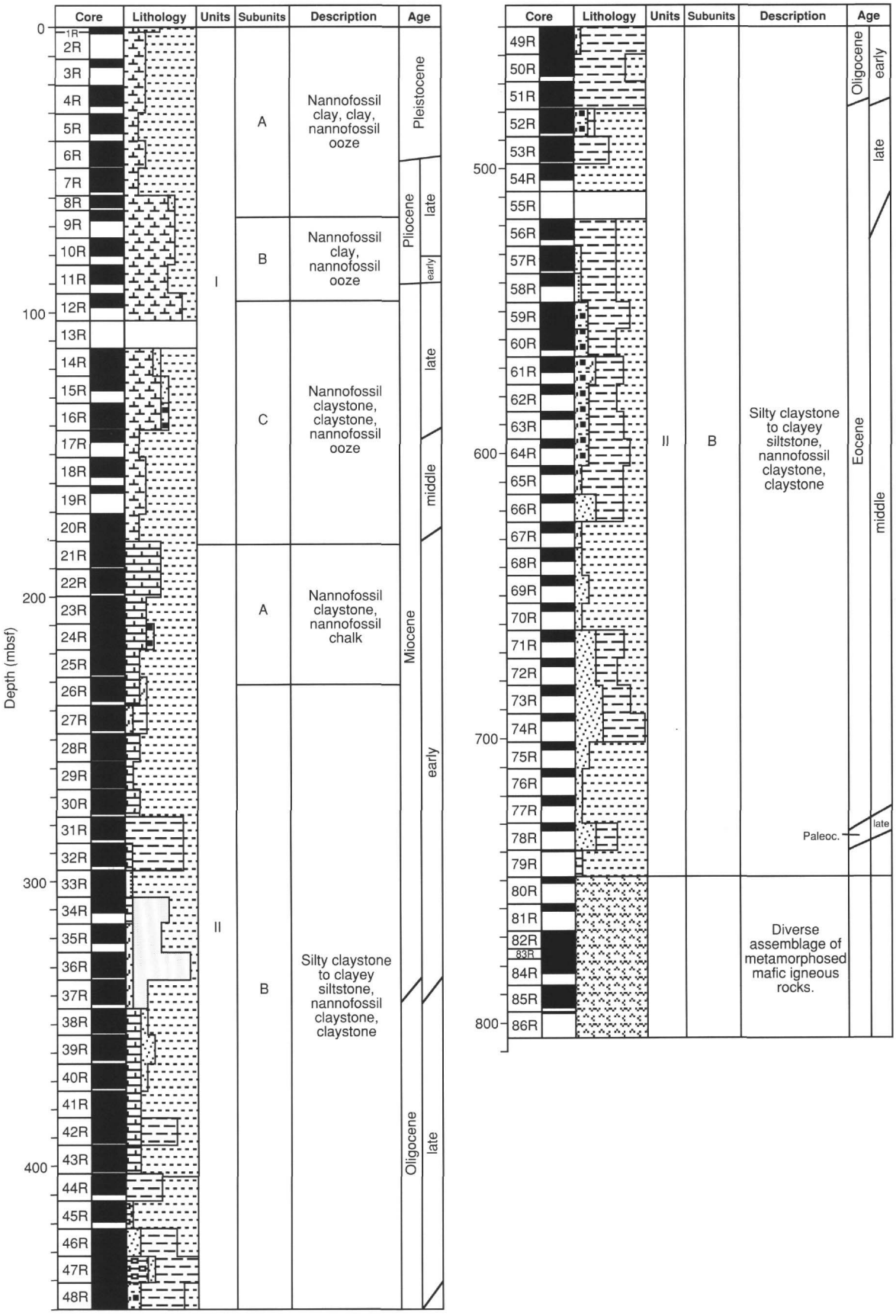

Figure 5. Master column for Site 900.

Table 4. Summary of colors exhibited by lithologies in Unit II at Site 900.

Color	Munsell code	Calc. silty sandstone	Clayey siltstone; silty claystone	Claystone	Calc./nanno. claystone	Nannofossil claystone	Nannofossil chalk
Medium gray	N3			■			
Dark gray	N4	+ ■					
Medium gray	N5	+ ■			■		
Light gray	N6	■	■				
Light gray	N7	+ ■	■		■	+ ■	+ ■
Very light gray	N8	■				■	■
White	N9						+
Grayish brown	5 YR 3/4			■			
Moderate brown	5YR 3/4		■	■			
Dark yellowish brown	10YR 4/2		■	■			
Mod. yellowish brown	10YR 5/4		■	■	■		
Pale yellowish brown	10YR 6/2		■		■		
Grayish orange	10YR 7/4		■		■		
Olive gray	5Y 4/1	+ ■	+ ■	+ ■	■	+ ■	
Light olive gray	5Y 5/1,5/2	■	■				
Light olive gray	5Y 6/1	+ ■			■	■	
Yellowish gray	5G 8/1					■	■
Dark greenish gray	5GY 4/1	■	+ ■	+ ■			
Greenish gray	5GY 5/1	■	+ ■	■		■	
Greenish gray	5GY 6/1	+ ■	+ ■	+ ■	■	+ ■	+
Light greenish gray	5GY 8/1	■	■		■	+ ■	+ ■
Greenish black	5G 2/1,2/2	+					
Dark greenish gray	5G 4/1	■	■	+ ■	■		
Dark greenish gray	5G 5/1	■	■	■		■	
Greenish gray	5G 6/1	+ ■	+ ■	■	■	■	■
Medium bluish gray	5B 5/1	■		■		■	
Light bluish gray	5B 7/1	■					

Note: Subunit IIA = +; Subunit IIB = ■.

Table 5. Biostratigraphic data used to constrain sediment accumulation rates for Site 900.

Code	Datum[a]	Age (Ma)	Depth range (mbsf)
1	B. *Emiliania huxleyi*	0.26	1.78–1.95
2	T. *Reticulofenestra* sp. A (>6.5 µm)	0.81	1.95–11.93
3	B. *Gephyrocapsa omega* (>3.8 µm)	0.92	13.39–24.60
4	T. common *Helicosphaera sellii*	1.19	27.79–32.08
5	T. *Cacidiscus tropicus* (cir., ≥11.5 µm)	1.54	43.20–46.15
6	B. *Gephyrocapsa caribbeanica* (> 4.0 µm)	1.64	46.15–47.56
7	TA. *Discoaster triradiatus*/ common *Discoaster brouweri*	1.88	46.15–47.56
8	T. *Discoaster surculus*	2.40	63.36–65.49
9	T. *Discoaster tamalis*	2.60	65.49–68.16
10	T. *Reticulofenestra pseudoumbilica*	3.56	79.88–80.29
11	T. *Triquetrorhabdulus rugosus*	5.30	80.29–89.13
12	T. *Discoaster quinqueramus*	5.38	89.13–90.28
13	B. *Amaurolithus delicatus*	7.01	103.03–120.15
14	B. *Discoaster quinqueramus*	7.60	138.86–140.88
15	T. *Cyclicargolithus floridanus*	11.71	140.88–145.14
16	B. *Triquetrorhabdulus rugosus*	12.50	145.45–155.27
17	TA. *Discoaster deflandrei*	16.05	189.04–191.12
18	B. *Sphenolithus heteromorphus*	18.42	227.57–231.93
19	T. *Triquetrohabdulus carinatus*	20.00	227.57–231.93
20	B. *Discoaster druggii*	22.80	305.58–311.21
21	T. *Sphenolithus ciperoensis*	24.60	352.75–358.27
22	T. *Sphenolithus distentus*	27.60	358.27–362.61
23	B. *Sphenolithus ciperoensis*	29.40	409.52–413.97
24	B. *Sphenolithus distentus*	33.10	449.91–460.04
25	T. *Discoaster barbadiensis*	35.60	477.33–478.52
26	B. *Isthmolithus recurvus*	37.10	504.19–508.30
27	T. *Chiasmolithus solitus*	40.80	541.65–556.00
28	T. *Nannotetrina* spp.	42.80	617.09–627.61
29	T. *Chiasmolithus gigas*	45.60	638.07–646.34
30	T. *Discoaster lodoensis*	48.10	693.94–703.78
31	B. *Discoaster multiradiatus*	57.50	723.65–731.98

[a] T = top; B = bottom; TA = top acme.

ages at Sites 897, 898, and 899. The rate for Unit I ranges from 12.9 m/m.y. over the lower part of Subunit IC, to 22.5 to 24.0 m/m.y. for the remainder of the unit; this is significantly lower than the rates for Unit I at Sites 897 (60 m/m.y.), 898 (90 m/m.y.), and 899 (35 m/m.y.). The sediment accumulation rates in Unit II (13-27 m/m.y.) are comparable to those seen over the same age range at the other sites.

Unit I

Cores 149-900A-1R through 149-900A-21R-1, 125 cm
Depth: 0-181.5 mbsf
Age: Pleistocene to late early Miocene

General Description

Core recovery averaged 65% in Unit I with 108.56 m being described. Core disturbance in the unit is soupy in Core 149-900A--1R, severe to moderate down to Core 149-900A-5R, and slight to moderate in the remaining cores.

Much of the unit consists of siliciclastic muddy turbidites (a few are carbonate-rich) containing some thin basal silty or sandy intervals and associated pelagic/hemipelagic sediments. The turbidites range in thickness from about 10 cm to more than 1 m and often are capped by pelagic nannofossil oozes up to 60 cm thick. Major lithologies are olive gray, yellowish brown, pale orange, and light gray nannofossil clay and nannofossil ooze. Minor lithologies include olive black, dark gray, olive gray, and greenish gray clay, clayey silt/silty clay, sandy silt/silty sand, and sand. Many occurrences of the sandy lithologies are foraminifer-rich and light gray.

Three types of turbidite sequence are present in Unit I:

1. Sand-mud siliciclastic sequences are the most common type. They consist of a very thin (<1 cm) normally graded basal sand or silty sand layer that passes upward into silty clay overlain by nannofossil clay (upper turbidite shown in Fig. 7).
2. Sand-mud calcareous sequences contain a basal siliciclastic foraminifer-rich fine sand layer overlain by nannofossil clay followed by a hemipelagic clay (lower turbidite shown in Fig. 7).
3. Siliciclastic silt-mud sequences contain a basal interval of silty clay followed by clay. In most sequences, bioturbation is pervasive and affects the contacts between the turbiditic clay and the overlying pelagic nannofossil oozes; no identifiable ichnofauna is visible.

Three subunits were recognized in Unit I on the basis of the proportions of different facies. In Subunit IA, the three types of turbidite sequence described above occur throughout and most are overlain by pelagic nannofossil ooze. The base of this subunit was placed at the last

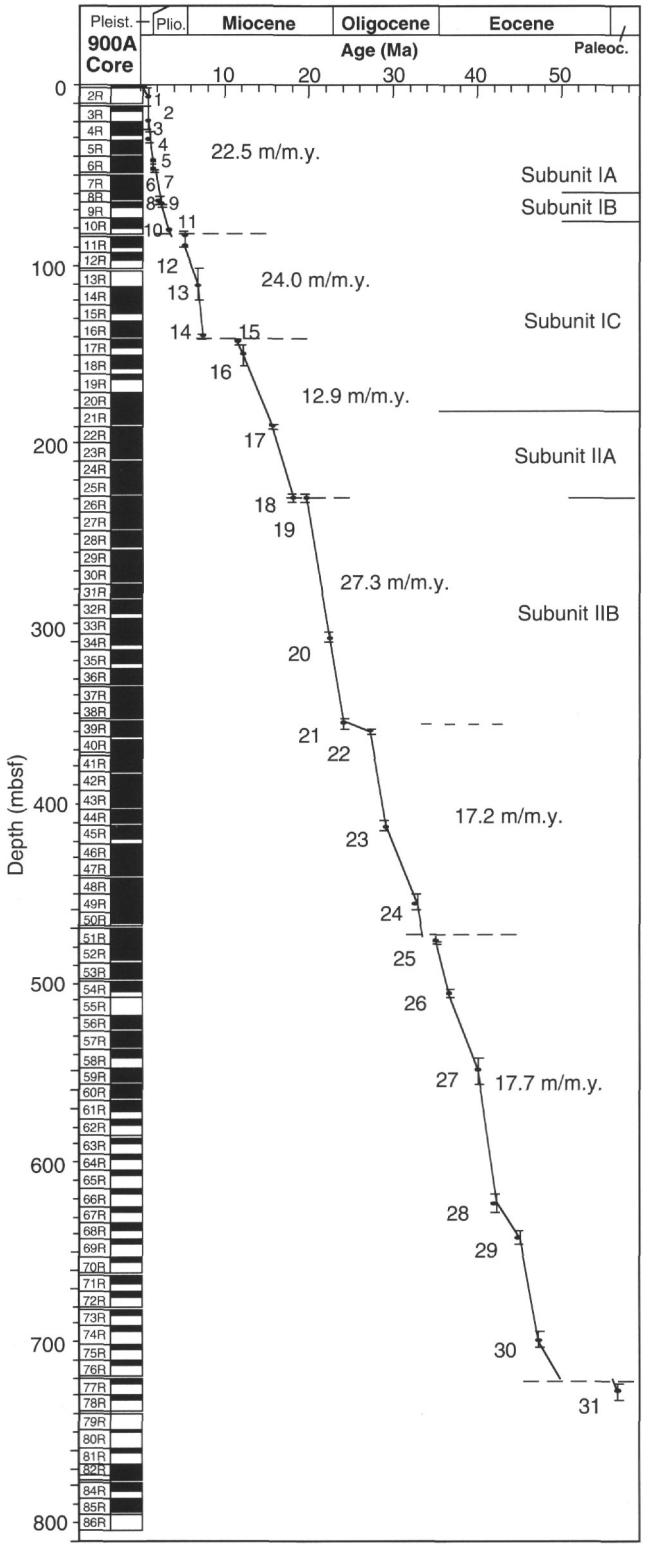

Figure 6. Depth vs. age curve for Site 900, plotted from data in Table 5 (see "Biostratigraphy" section, this chapter). Each data point is shown with a depth error bar. Dashed horizontal lines indicate hiatuses or condensed sections. Continuous horizontal lines are lithostratigraphic unit boundaries. Slopes of lines connecting adjacent data points are sediment accumulation rates for that time or depth interval. In contrast to Sites 897, 898, and 899, no significant difference was seen between the sediment accumulation rates for Units I and II.

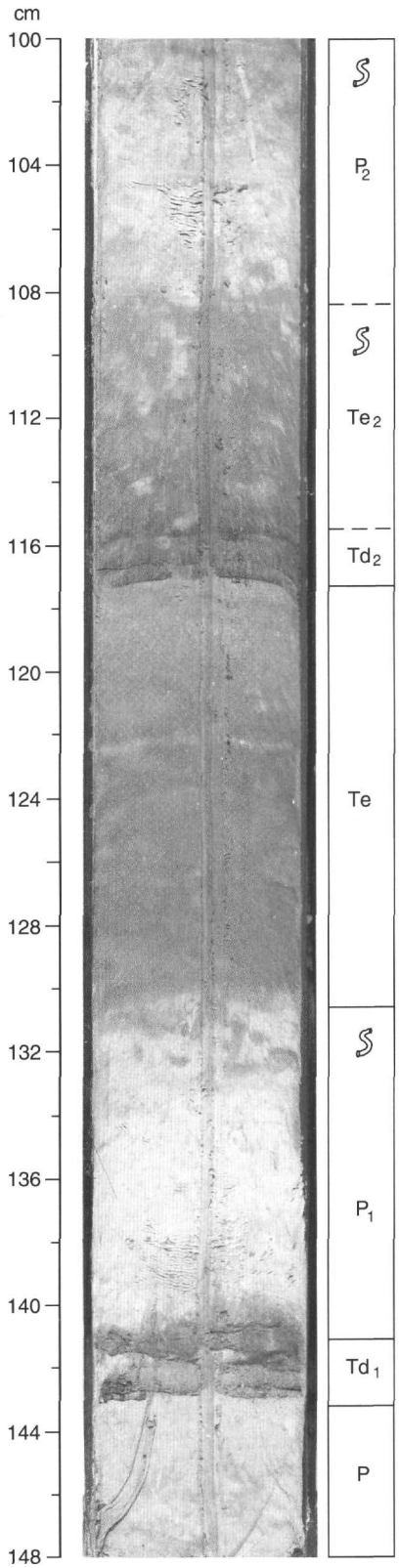

Figure 7. Two mud-dominated turbidite sequences in Subunit IC (Interval 149-900A-18R-4, 100-148 cm). In the upper one, the sandy base (Td_2) grades upward to terrigenous clay (Te_2) overlain by nannofossil clay (pelagite, P_2). In the lower sequence, the Te interval is cut out, and the sand (Td_1) is capped by nannofossil clay overlain by terrigenous clay (pelagite, P_1). Te corresponds to a muddy turbidite composed of silty clay.

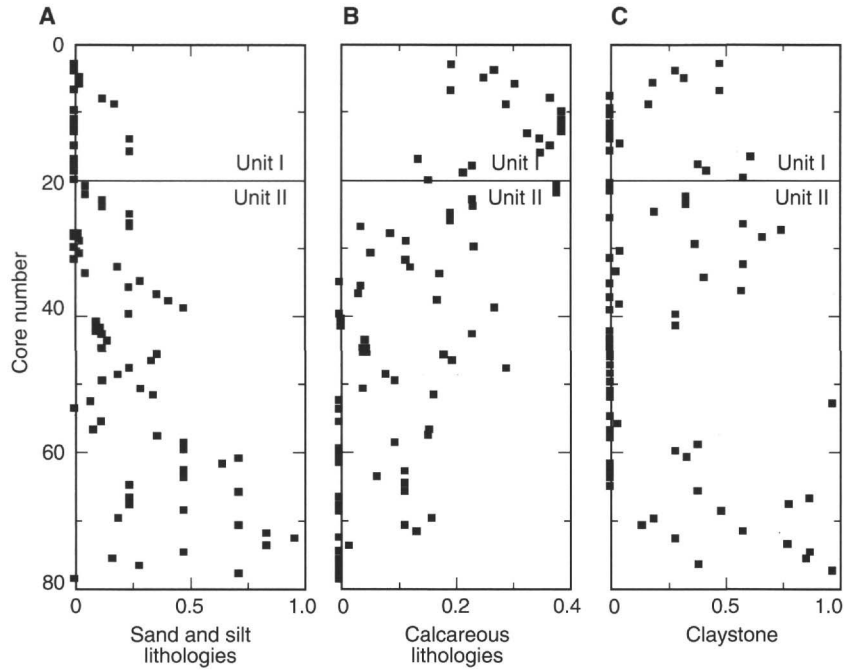

Figure 8. Plots of sand and silt lithologies (**A**), calcareous lithologies (**B**), and claystone lithologies (**C**) vs. depth. Lithologies are plotted as a fraction of the total lithologic assemblage present in each core. Calcareous lithologies include nannofossil oozes and chalks and nannofossil clays and claystones. Sand and silt lithologies include siltstone and sandstone and their unlithified equivalents. Depth trends for these various lithologies show that compositional variations through Unit II are gradational.

turbidite sequence with a basal sand interval at 149-900A-9R-2, 122 cm. Subunit IB consists entirely of pale orange and yellowish brown nannofossil claystones and oozes mixed to varying degrees by bioturbation. Its lower boundary is defined at the top of the first turbidite sequence at Sample 149-900A-12R-2, 110 cm. Subunit IC shows a gradual change in color from the pale orange and yellowish brown typical of Subunit IB, to olive and greenish gray. All three types of turbidite sequence occur throughout this subunit, and most of them are overlain by pelagic nannofossil oozes. The top of Subunit IC is dominated by nannofossil clays (in Cores 149-900A-12R and -14R), but the proportion of nannofossil ooze increases down the subunit.

Petrography

Applying the classification of Folk (1980), sands and silts of Unit I are subarkoses to arkoses. Grain types in Unit I indicate derivation from a source area that exposed mostly sedimentary, metamorphic, and, possibly, granitic rocks. The detailed petrography of the sediments in Unit I is identical to that described for Site 898 (see "Lithostratigraphy" section, "Site 898" chapter, this volume).

Depositional Processes

The location of Site 900, at the foot of the gently sloping continental rise, provides an explanation for the absence of significant amounts of siliciclastic sand at the base of the turbidite sequences in Unit I. The velocity of the turbidity flows would have been higher on the continental rise than on the nearly flat abyssal plain. The flows would also have had higher mud contents as they flowed over the rise, which would have increased their competency to transport sand. Therefore, most of their sand component would have remained in turbulent suspension and so would have bypassed the continental rise to be deposited later on the abyssal plain. This would have resulted in the fine-grained sediment being carried in the "tails" of the flows, with the nepheloid layer being the dominant part of the turbidite sequences.

The presence of both siliciclastic and carbonate bases to the turbidites suggests two distinct provenances for the sediments transported by the turbidity flows. The carbonate sediment was probably derived by the reworking of nannofossil oozes deposited higher on the continental rise or slope, whereas the siliciclastic sand, silt, and mud originated from more distant sources on the shelf or on land. The thick intervals of nannofossil clay and ooze characteristic of Subunit IB indicate the absence of siliciclastic sand- or mud-laden turbidity flows, although carbonate-rich flows and/or nepheloid layers could have supplemented the pelagic influx.

Unit II

Cores 149-900A-21R-1, 125 cm to 149-900A-79R-CC
Depth: 181.50-748.9 mbsf
Age: early Miocene to Paleocene

General Description

Core recovery within Unit II averaged 68% and ranged from 0% to 101%; it remained above 70% down to Core 149-900A-53R, whence it began to deteriorate, to rise only once above 40% below Core 149-900A-61R. From the top of the unit, the sediments are significantly more indurated, and so the cores were cut using a saw.

Unit II was divided into two subunits. Both are dominated by olive gray and light greenish gray colors, but from Core 149-900A-69R to the base of Subunit IIB, brown colors dominate nearly all the sections. Figure 8 shows downhole variations in the proportions of calcareous lithologies, sand and silt, and claystones. This figure indicates that downhole changes in composition are gradational, so that further subdivision of Unit II would be difficult.

The major lithologies in Unit II are claystone, silty claystone/claystone with silt, and nannofossil claystone (Table 2). Foraminifer-rich siliciclastic sandstones and calcarenites form up to 20% to 30% of some cores in Subunit IIB, where they are often calcite-cemented; these lithologies are a minor component of Subunit IIA. Nannofossil chalk forms about a quarter of the sediment in Subunit IIA, but in Subunit IIB it occurs only rarely in intervals up to 10 cm thick into which overlying darker lithologies usually have been mixed by bioturbation. In Subunit IIA and the upper part of Subunit IIB, a significant biogenic silica component is present in the sandstones and silty claystones (Fig. 9), but it is not present below Core 149-900A-47R (440.6 mbsf), except for a trace in Core 149-900A-51R.

The transition from Unit I to Unit II coincides with a change from greenish-gray turbidites to an interval containing upward-darkening and upward-lightening sequences. The division of Unit II into two subunits is based on changes in color, composition, and the nature of

repetitive lithologic sequences. Subunit IIA consists mostly of lighter greenish-gray nannofossil claystones and claystones, which occur in both upward-darkening and upward-lightening sequences. Subunit IIB contains a greater variety of lithologies and colors, mostly arranged in upward-darkening sequences, and slumped sediments occur at the top of it. The boundary between the two subunits was placed at 149-900A-26R-4, 135 cm. A fault of unknown displacement occurs 2 cm below this boundary. The sediments beneath the boundary are fractured, and those in Sections 149-900A-27R-1 and -2 show maximum bedding dips of 35°, whereas the remaining sections contain almost horizontal bedding. These features suggest that the boundary occurs at a fault or fault zone having a significant but unknown displacement (see "Structural Geology" section, this chapter).

Subunit IIA

Core recovery from Subunit IIA averaged 92%. It is composed predominantly of greenish gray to light gray nannofossil claystone, claystone, and silty claystone. Minor lithologies include calcareous and siliciclastic silty sandstone/sandy siltstone, locally foraminifer-rich, and nannofossil chalk. The proportion of silty claystone increases, and nannofossil chalk decreases, downhole (Fig. 8), with the latter lithology forming 50% of Core 149-900A-22R. Bioturbation is pervasive and commonly mixes different lithologies; *Planolites, Chondrites,* and *Zoophycos* are common.

Subunit IIA consists of both upward-darkening and upward-lightening sequences; bioturbation is concentrated at the top of both types of sequence. Individual upward-lightening sequences are 5 to 30 cm thick and begin with a claystone overlain by a nannofossil claystone and/or nannofossil chalk. Fine siliciclastic sandstone or siltstone intervals, generally less than 5 cm thick, sometimes underlie the basal claystone. Upward-darkening sequences 5 to 15 cm thick are similar to those described in Subunit IIB at Sites 898 and 899 (see "Lithostratigraphy" sections, "Site 898" and "Site 899" chapters, this volume). They consist of a nannofossil claystone to chalk gradationally overlain by darker claystone to silty claystone. The base of these couplets frequently is composed of an uncemented to poorly cemented siliciclastic to foraminifer-rich sandstone or siltstone.

Sandstone and siltstone layers range up to 3 cm thick and show parallel to cross laminations, sharp bases, and sharp to gradational tops (Fig. 10). Bioturbation occurs in some of these layers. Sandstones and siltstones do not exceed 10% of any core. Boundaries of drilling biscuits coincide with the sandstone/siltstone intervals, indicating that some of these lithologies may have been washed out. Consequently, the sandstone/siltstone proportions shown in Figure 8 may be underestimated.

Subunit IIB

Subunit IIB was cored over an interval of 505.61 m., with an average recovery of 65%. The unit consists predominantly of light-colored nannofossil claystone and dark greenish to brownish claystone with silt and claystone (see Tables 2 and 4). Minor lithologies include nannofossil chalk and calcite-cemented to poorly indurated siliciclastic to bioclastic sandstones and calcarenites or silty sandstone. Sandstones and calcarenites form 20% to 30% of the cores in the lower part of the subunit below Core 149-900A-60R (Fig. 8).

Downhole variations in color, degree of sandstone cementation, bioturbation, and bedding dips occur in this subunit. Brownish colors first appear in Core 149-900A-50R; above this level, the darker colors consist mostly of greenish gray and olive gray. Calcite-cemented sandstones appear in Core 149-900A-33R and are present in most cores below this level. They become thicker (up to 12 cm) and more abundant (up to 35% of a core) below Core 149-900A-53R.

Trace fossils become more prominent below the top of Core 149-900A-52R, and in this core, well-preserved and abundant *Zoophycos* burrows occur. Below this core, structural dips of about 15° are

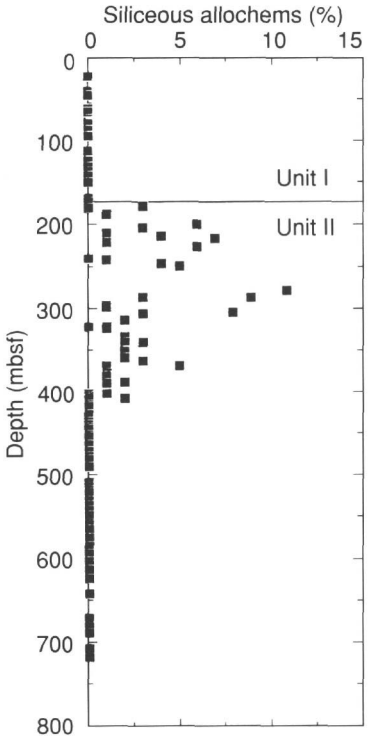

Figure 9. Variation in the content of biogenic siliceous material (sponge spicules, radiolarians, and diatoms) with depth, as revealed by smear slide analyses of dominant lithologies.

visible which, together with the existence of a hiatus at this level (Fig. 6), suggest the presence of an unconformity.

Upward-darkening sequences are common in Subunit IIB (Fig. 11) and are similar to those described in Subunit IIB at Sites 898 and 899 (see "Lithostratigraphy" sections, "Site 898" and "Site 899" chapters, this volume). They begin with an irregular, basal, thin bed (up to 5 cm thick, but more commonly 0.5 to 3 cm thick) of mixed biogenic and terrigenous fine sandstone to siltstone. The basal silt- and sand-rich intervals of the upward-darkening sequences have been overlain by claystones, claystones with silt, or nannofossil claystones. Sometimes, intervals in these lithologies contain zones up to 1 to 2 cm thick of sand-filled burrows 1 to 3 mm in diameter. The boundary with the overlying darker-colored silty claystones and claystones is transitional as a result of mixing by bioturbation. Clearly identifiable ichnofauna *(Zoophycos, Planolites,* and *Chondrites)* are concentrated (or more clearly visible) in the light-colored carbonate-rich lithologies in the lower part of each individual sequence. Usually, the burrowing extends down to the basal calcareous sandstone/calcarenite bed.

The sharp-based siliciclastic sandstones and bioclastic calcarenites are thicker (1-20 cm) than those in Subunit IIA and occur both as normally graded and sharp-topped beds. The sandstones and calcarenites are common in Cores 149-900A-35R to -51R, and from Core 149-900A-58R to the bottom of the hole. They often show parallel- and cross-lamination (Fig. 12) and frequently contain a few burrows filled with overlying lithologies. Where the tops of the sandstones or calcarenites are gradational, the transition to the upper nannofossil claystone is sometimes characterized by a wavy, parallel, or lenticular lamination between both lithologies, as well as by burrow mottling between them.

In the lower part of the subunit (Core 149-900A-66R and below), well-cemented calcareous sandstones occur that contain features not encountered in the sandstones at higher levels such as ball and pillow structures (Fig. 13), isolated ripples, flaser and wavy bedding, and

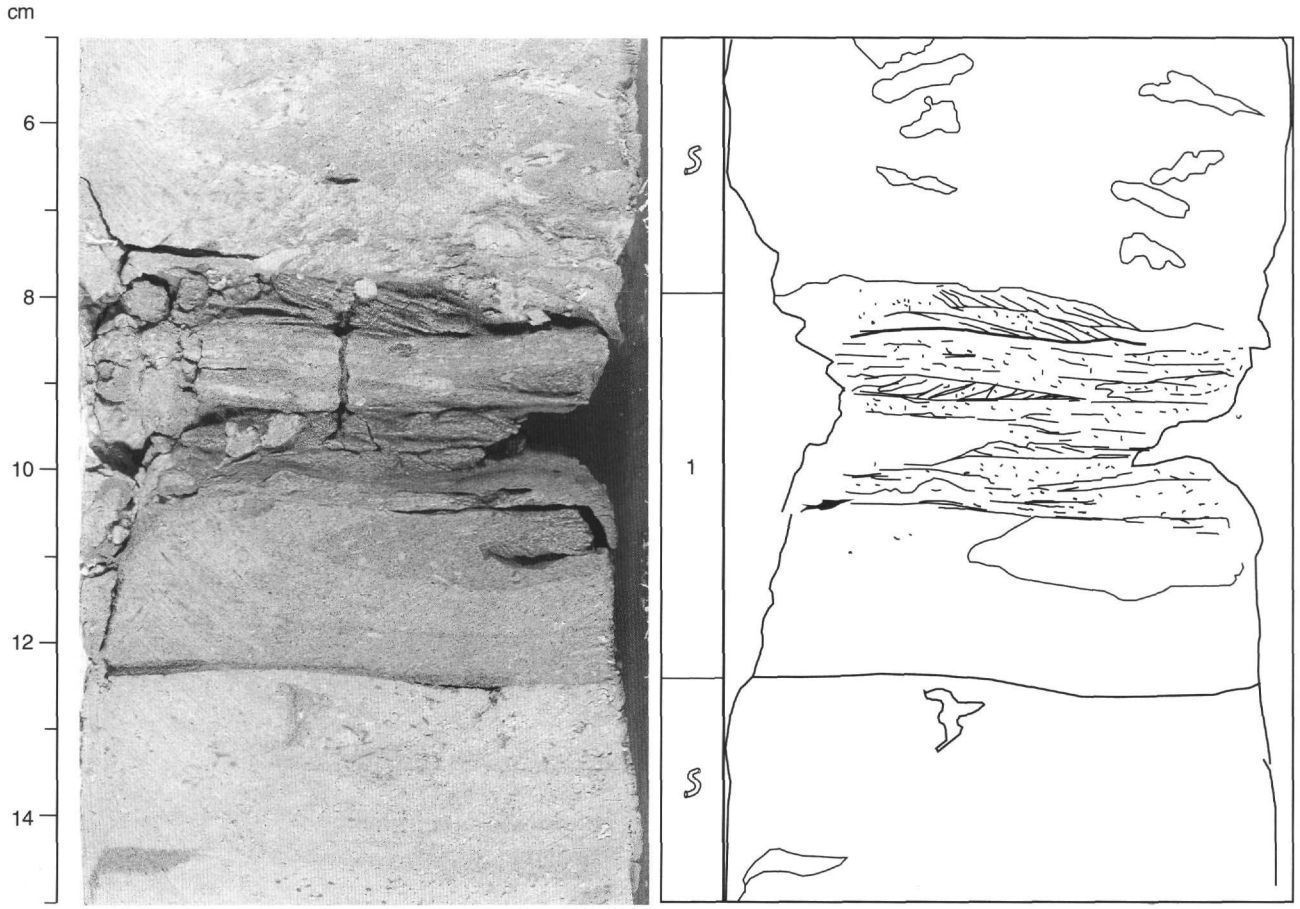

Figure 10. Foraminifer-rich sandstone bed (1) in Subunit IIA (Interval 149-900A-21R-2, 5-15 cm), showing a sharp base and top, and parallel- and cross-laminated layers with scattered burrows. The bed is probably a contourite.

sole marks. These sandstones also show parallel- and cross-lamination, rippled tops, siltstone and claystone laminae, and are lenticular to discontinuous and commonly bioturbated (Fig. 14).

Unit II Petrography

Sand- and silt-sized detritus in Unit II includes detrital components similar to the assemblage observed in Unit I. In addition, a substantial diagenetic component first appearing downhole in Core 149-900A-38R in the form of calcite cement in the sandstones and siltstones is present at this site. The cement is equant, sparry calcite that fills primary porosity (including intraskeletal porosity in carbonate allochems), but shows scant evidence of grain replacement.

Unit II also contains clay-rich lithologies that are similar to those in Unit I, except that the Type 2 (oriented clays in carbonate-poor lithologies) clay-rich lithologies (defined in the "Lithostratigraphy" section, "Site 897" chapter, this volume) are a more persistent and volumetrically significant part of the lithologic assemblage.

Clay minerals examined in Units I and II at Site 897 contained an expandable clay, discrete illite, and kaolinite (see "Lithostratigraphy" section, "Site 897" chapter, this volume). Preliminary examination of XRD data for two samples at Site 900 revealed the presence of mixed-layer illite/smectite in the deeper, more lithified portions of Subunit IIB (Samples 149-900A-67R-2, 44-16 cm and -69R-1, 33-34 cm). These mixed-layer clays contain around 40% illite layers. We are not sure if the appearance of these clays is related to provenance variation or to diagenetic effects. The increased degree of lithification in the claystones is at least circumstantial evidence that the mixed-layer clay is diagenetic in origin. Other phases within the clay mineral assemblage at this site are discrete illite and kaolinite.

Another possible diagenetic effect observed at this site is the possible alteration of the siliceous allochems. Samples from Cores 149-900A-44R to -47R contain sponge spicules showing pitted surfaces suggestive of dissolution. However, there is no evidence of replacement of spicules by crystalline silica or of precipitation of other authigenic silica mobilized through dissolution of the spicules.

Depositional Processes

Subunit IIA

Sedimentation during deposition of Subunit IIA resulted from turbidity and contour current deposition near the foot of the continental rise. Upward-lightening sequences are similar to those described in the turbiditic parts of Unit I, suggesting that turbidity currents periodically deposited sediment. Upward-darkening sequences contain siliciclastic to bioclastic sandstone/siltstone layers that show evidence (sharp bases and tops, cross- and planar-laminations) of transport by traction currents, which suggests deposition from contour currents. High biogenic carbonate contents in hemipelagic intervals plus pervasive bioturbation suggest that deposition occurred in a dysaerobic environment above the carbonate compensation depth (CCD). Shifts from bioclastic to siliciclastic sands may result from changes in sediment source areas, with the siliciclastic sediments derived from the continental shelf, and the bioclastic sands from local highs. Alternatively, some of the foraminifer-rich sands could result from current winnowing of turbidites.

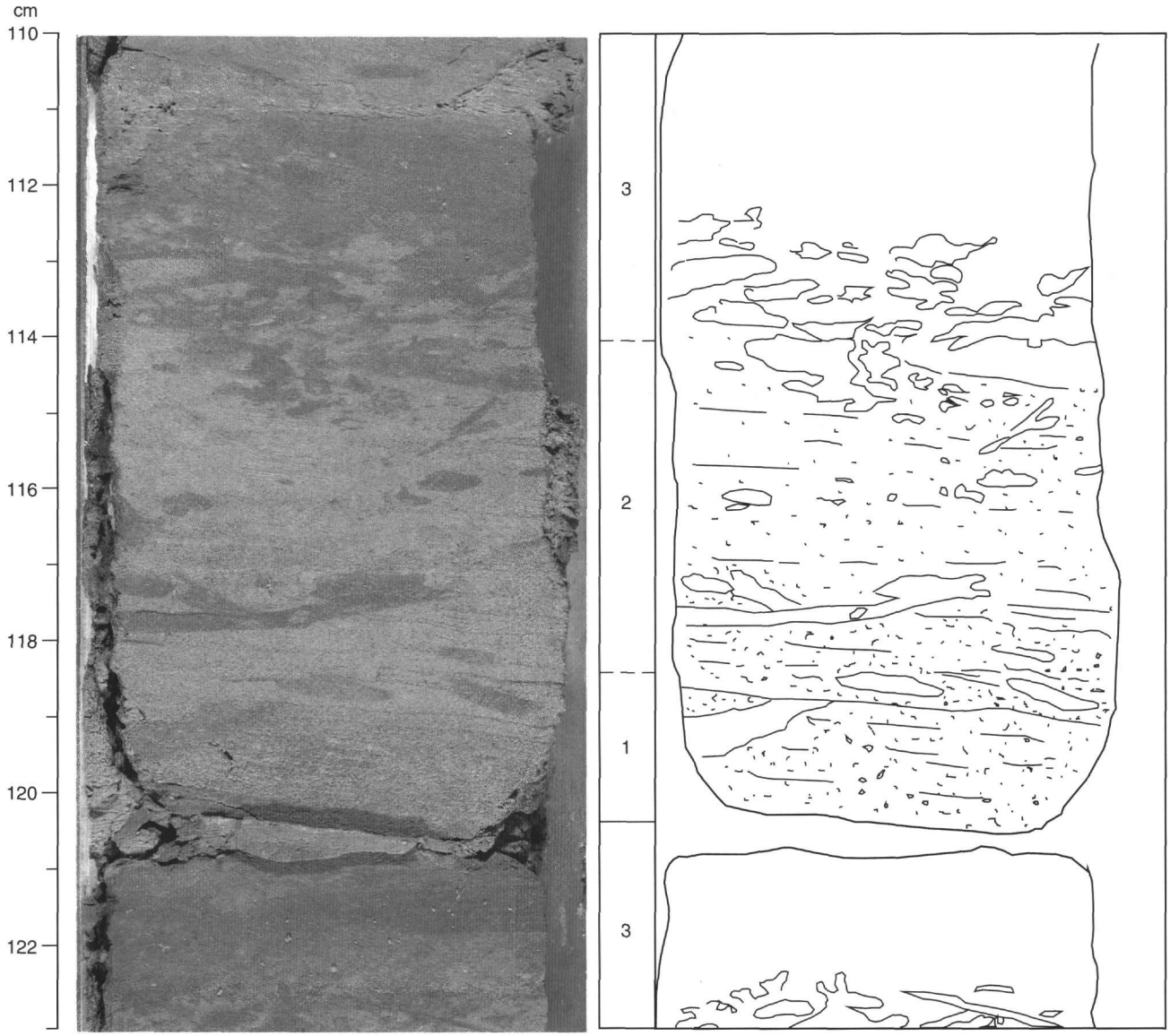

Figure 11. Upward-darkening sequence in Subunit IIB (Interval 149-900A-42R-6, 110-123 cm), consisting of a basal, slightly bioturbated parallel-laminated foraminifer-rich sandstone (1) passing upward into laminated sandy siltstone (2) and capped by darker moderately bioturbated claystone (3). The sequence is interpreted as a turbidite.

Subunit IIB

Repetitive upward-darkening sequences, which occur through most of the upper part of Subunit IIB (above Core 149-900A-53R), do not show sequences that can unequivocally be associated with deposition from turbidity currents. Thin, silty sandstone and siltstone intervals at the bases of many of the upward-darkening sequences lack clear normal grading. Furthermore, these silty sandstones and siltstones contain small-scale parallel and cross-lamination, and sharp bases and some sharp tops, indicating bottom current activity. These features point to reworking by contour currents as described by Stow and Piper (1984). The homogeneous, carbonate-poor terrigenous silty claystone and claystone couplets may be mud turbidites or contourites.

Continuous to lenticular calcite-cemented sandstones in the lower half of Subunit IIB may also reflect a combination of turbidity and contour current deposition. Scour and fill structures, cross, wavy, and parallel laminations, are more representative of turbidity than contour current deposition (Fig. 15). The occurrence of isolated ripples of sandstone enclosed in claystone that occur near the base of the subunit may have resulted from a combination of low clastic influx and bottom-current reworking. These features occur in thicker sandstones than those present in the upper part of the subunit, and so it is possible that they were deposited in a lobe fringe setting where turbidity flows and contour currents were operative at the same time.

BIOSTRATIGRAPHY

Sediments recovered from Hole 900A provide a discontinuous record for Pleistocene through the upper Paleocene. Calcareous nannofossils generally are abundant to very abundant, and preservation varies throughout the recovered successions. Planktonic foraminifers generally are common to abundant in the upper sections of Hole 900A, but samples from the deeper sections contained fewer specimens.

Calcareous Nannofossils

Site 900 is located near the eastern edge of the Iberia Abyssal Plain at a water depth of 5037 m. The calcareous nannofossils define four

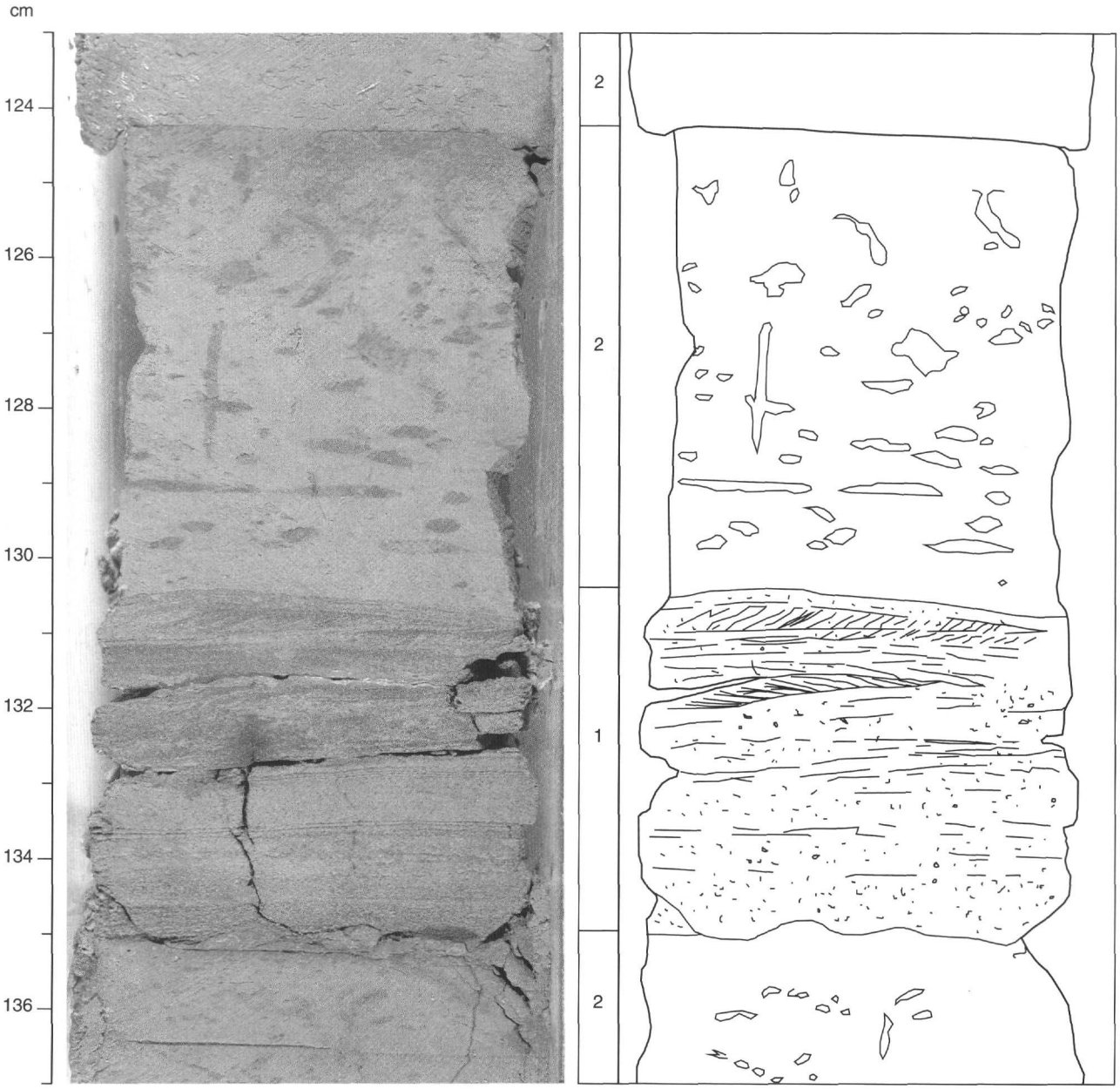

Figure 12. Ungraded sandstone (1) and nannofossil claystone (2) couplet in Subunit IIB (Interval 149-900A-36R-4, 123-137 cm). The lower foraminifer-rich sandstone interval (1) has a sharp base and top, with parallel-lamination at the base and cross- and parallel-lamination at the top. The sequence is interpreted as a contourite.

major stratigraphic successions within the Cenozoic sediments; one succession from the upper Pleistocene (Zone NN21 of Martini, 1971) to the upper lower Pliocene (Zone NN15), a second from the uppermost Miocene (base Zone NN12) to the upper Miocene (Zone NN11), a third from the middle Miocene (NN7) to the middle Eocene (NP14), and a fourth restricted to the upper Paleocene (NP9). Two major hiatuses, representing most of the lower Pliocene and the lower upper Miocene, correspond to those observed at Sites 897, 898, and 899.

In the interval from the upper Pleistocene to the upper lower Pliocene, calcareous nannofossils are abundant and well preserved. Nannofossils are generally abundant and moderately well preserved from the Miocene to the Oligocene. The Eocene succession is characterized by fewer, moderately preserved calcareous nannofossils, or by barren samples. From Core 149-900A-78R, upper Paleocene sediments were recovered that contain abundant and well-preserved nannofossils. No sediments were recovered below Core 149-900A-79R. Ages of calcareous nannofossils are summarized in Figure 16.

Pleistocene

Section 149-900A-1R contains rare to few *Emiliania huxleyi* and very abundant small *Gephyrocapsa* spp. (<2.5 µm), indicating the lower part of Zone NN21. Samples 149-900A-2R-1, 28 cm, and -2R-CC were assigned to Zone NN20 by the absence of *Emiliania huxleyi* and *Pseudoemiliania lacunosa.* Intervals 149-900A-3R-1, 83 cm, highest occurrence (HO) *of Pseudoemiliania lacunosa,* to -6R-4, 15 cm, lowest occurrence (LO) *of Gephyrocapsa caribbeanica* (>4.0 µm), were placed in Zone NN19. Mediterranean subzones of Rio, Fornaciari et al. (1990) were used within this succession. Samples 149-900A-3R-1, 83 cm, and -3R-CC include *Pseudoemiliania lacu-*

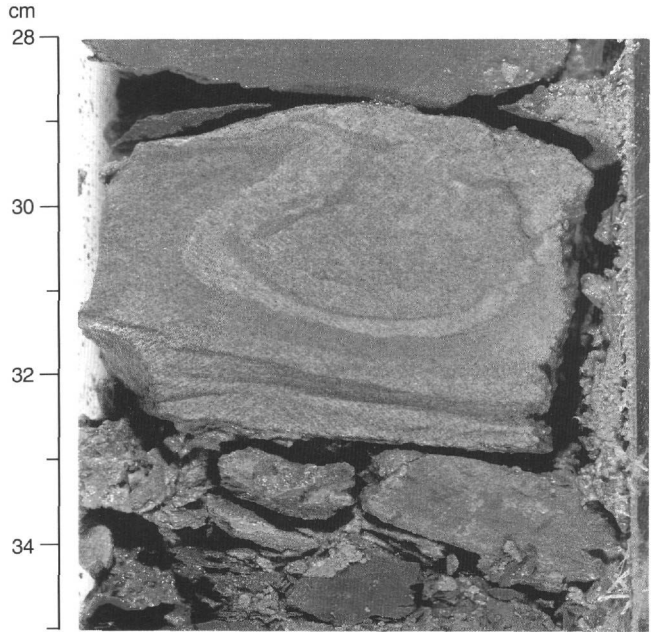

Figure 13. Ball and pillow structure in calcite-cemented sandstone in Subunit IIB (Interval 149-900A-67R-2, 28-35 cm).

nosa and *Reticulofenestra* sp. A (>6.5 µm), indicating Zone NN19F. The LO of small *Gephyrocapsa omega* (>3.8 µm) in Sample 149-900A-3R-CC indicates the lower part of Zone NN19F. The presence of very abundant small *Gephyrocapsa* spp. (<2.5 µm) and common *Reticulofenestra* sp. A (>6.5 µm) place Sample 149-900A-4R-3, 80 cm, in Zone NN19E. Sample 149-900A-5R-2, 17 cm, contains few *Helicosphaera sellii* and common *Gephyrocapsa* spp. (>5.5 µm), indicating the upper part of Subzone NN19C. The absence of large *Gephyrocapsa* spp. (>5.5 µm) in Sample 149-900A-5R-CC indicates the lower part of Zone NN19C. Sample 149-900A-6R-4, 15 cm, contains the HO of *Calcidiscus macintyrei* (cir.; >10.0 µm), few *Gephyrocapsa oceanica* (>4.0 µm) and *Gephyrocapsa caribbeanica* (>4.0 µm). This assemblage indicates Zone NN19B.

Pliocene

The Pliocene/Pleistocene boundary was placed between Samples 149-900A-6R-4, 15 cm (LO of *Gephyrocapsa oceanica* [>4.0 µm]) and 149-900A-6R-6, 6 cm (HOs of *Discoaster brouweri* and *Discoaster triradiatus).* A few *Discoaster brouweri* and *Discoaster triradiatus* co-occur in Samples 149-900A-6R-6, 6 cm, and -6R-CC, indicating the upper part of Zone NN18. Intervals 149-900A-7R-CC to -8R-CC contain only rare *Discoaster brouweri* and *Discoaster triradiatus.* The co-occurrence of *Discoaster pentaradiatus* and *Discoaster surculus* in Sample 149-900A-9R-1, 99 cm, defines the top of Zone NN16. *Discoaster tamalis* appears in Sample 149-900A-9R-CC**.** The HO of *Reticulofenestra pseudoumbilica* was observed in Sample 149-900A-10R-CC, together with abundant *Discoaster asymmetricus,* indicating Zone NN15. The upper/lower Pliocene boundary, equivalent to the zonal boundary NN15/NN16, lies between Samples 149-900A-10R-4, 128 cm, and -10R-CC. Most of the lower Pliocene succession is missing in Hole 900A.

Miocene

Sample 149-900A-11R-4, 93 cm, contains *Amaurolithus delicatus, Triquetrorhabdulus extensus,* but lacks *Discoaster quinqueramus.* This assemblage indicates the lower part of Zone NN12, which has been placed in the uppermost Miocene. An unconformity, representing most of the lower Pliocene sequence, lies between Samples 149-900A-10R-CC (acme in *Discoaster asymmetricus*) and -11R-4, 93 cm (pres-

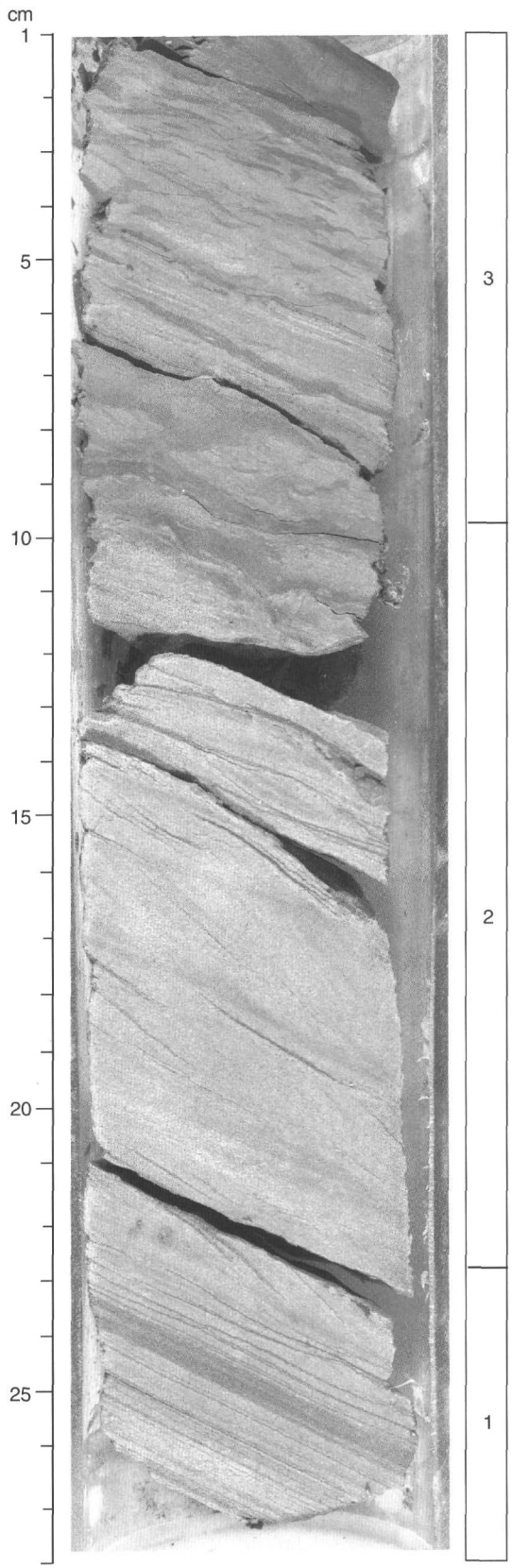

Figure 14. Calcareous sandstone sequence near the base of Subunit IIB (Interval 149-900A-77R-CC, 1-28 cm), showing planar lamination (1) at the base, faint cross-lamination in the lower half (2), and discontinuous to continuous, wavy lamination at the top (3). This sequence is interpreted as a turbidite, possibly deposited in a lobe-fringe setting.

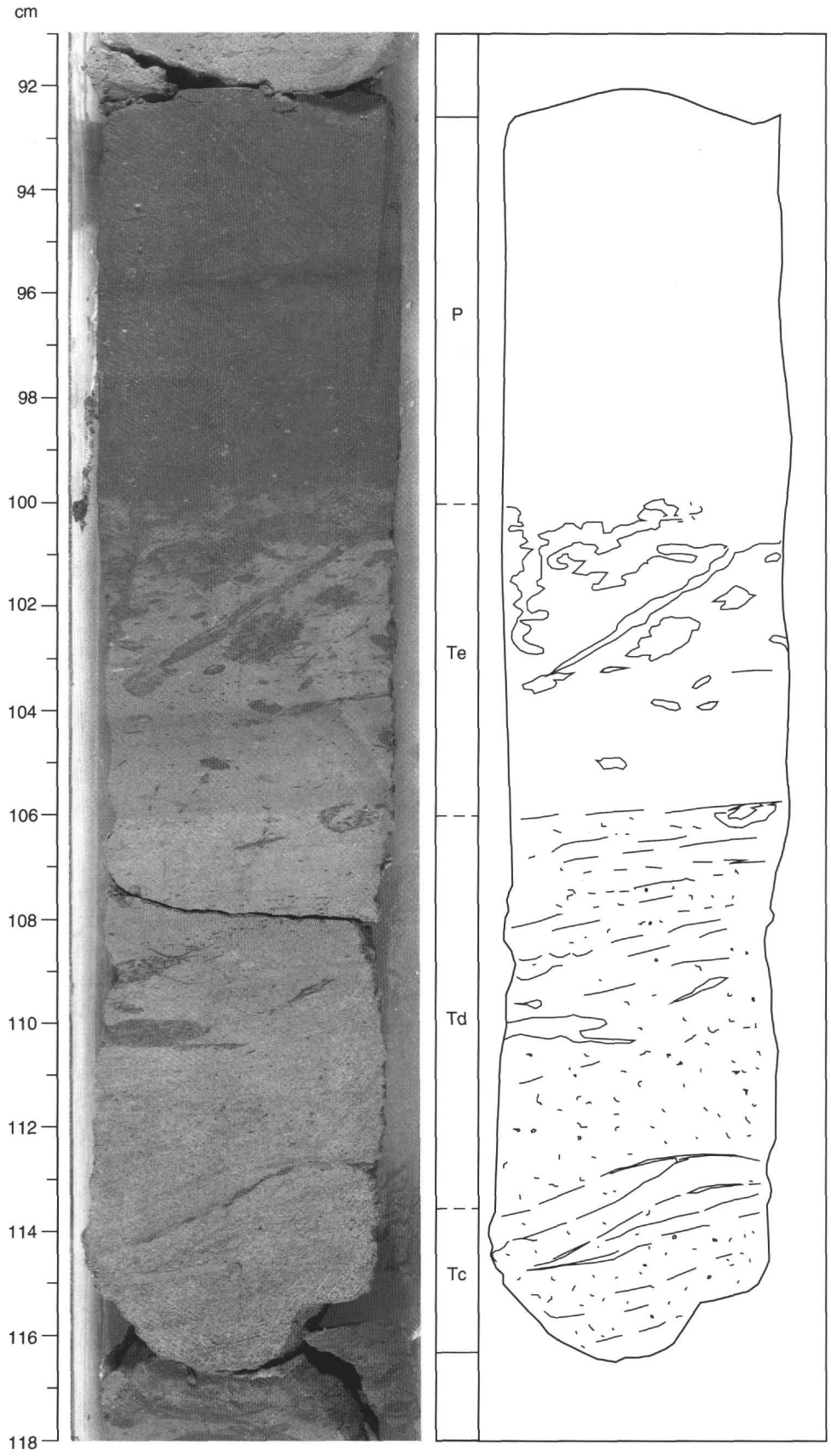

Figure 15. Upward-darkening calcareous sand-to-mud turbidite sequence in Subunit IIB (Interval 149-900A-46R-1, 91-118 cm). A Tc-Te sequence is capped by a dark claystone pelagite (P). Note the sole mark and ripple cross-lamination in the sandy interval. The sequence dips slightly.

ence of *Triquetrorhabdulus extensus)*. Samples 149-900A-11R-CC to -16R-5, 86 cm, contain *Discoaster quinqueramus,* the total range of which defines Zone NN11. The LO of *Amaurolithus delicatus* was observed in Sample 149-900A-13R-CC and defines the NN11a/NN11b boundary. The LO of *Discoaster berggrenii* can be observed in Sample 149-900A-16R-CC, indicating the lower part of Zone NN11 or the upper part of Zone NN10. The absence of *Discoaster bollii, Discoaster hamatus,* and *Catynaster calyculus* between this sample and Sample 149-900A-17R-3, 54 cm (HO of *Cyclicargolithus floridanus*) indicates an unconformity representing Zones NN8 to NN10. Samples 149-900A-17R-3, 54 cm, and -17R-CC were placed in Zone NN7 on the basis of the presence of rare *Cyclicargolithus floridanus* and common *Coccolithus miopelagicus* and *Triquetrorhabdulus rugosus.* The NN6/NN7 zonal boundary was difficult to define because of only a rare occurrence of *Discoaster kugleri;* however, it was placed between Samples 149-900A-17R-CC and -18R-3, 97 cm, on the basis of the LO of *Triquetrorhabdulus rugosus.* The interval 149-900A-19R-CC to -20R-CC contains rare to few *Discoaster deflandrei,* few *Calcidiscus premacintyrei,* and rare *Reticulofenestra umbilica,* which indicate Zone NN5. The HO of *Sphenolithus heteromorphus* occurs in Sample 149-900A-20R-2, 89 cm. In the absence of *Helicosphaera ampliaperta,* the NN4/NN5 boundary may be approximated by the end of the *Discoaster deflandrei* acme (Rio, Raffi, et al., 1990) (Sample 149-900A-22R-1, 122 cm), by the LOs of *Discoaster formosus* and *Discoaster moorei* (Sample 149-900A-21R-1, 94 cm), and by the LO of *Discoaster exilis* (Sample 149-900A-20R-CC). This boundary was placed above the LO of *Discoaster exilis.* The LO of *Sphenolithus heteromorphus* occurs in Sample 149-900A-25R-CC and marks the NN4/NN3 boundary. The HO *Triquetrorhabdulus carinatus* was observed in Sample 149-900A-26R-3, 53 cm, and indicates the NN3/NN2 boundary. From Samples 149-900A-26R-3, 53 cm, to -31R-CC, the nannofossil assemblages include *Sphenolithus dissimilis* and the *S. dissimilis-S. belemnos* Intergrade. The LO of the rare *Discoaster druggii* was difficult to place because of the occurrence of overgrowth specimens, which were slightly smaller than 15 µm, between Sample 149-900A-32R-CC and -34R-CC. Therefore, the NN2/NN1 boundary was placed by the LO of *Helicosphaera elongata* (Sample 149-900A-34R-CC). The interval from Samples 149-900A-35R-CC to -38R-CC was assigned to Zone NN1. The calcareous nannofossil assemblages in this interval are characterized by rare *Triquetrorhabdulus carinatus* and few *Reticulofenestra bisecta, Clausicoccus fenestratus, Clausicoccus tasmaniae, Helicosphaera perch-nielseniae, Helicosphaera intermedia, Helicosphaera euphratis, Discoaster woodringii,* and *Zygrhablithus bijugatus. Sphenolithus conicus* was present from Samples 149-900A-36R-CC to -37R-CC.

Oligocene

The Oligocene/Miocene boundary, situated in the middle of Zone NN1, lies between Samples 149-900A-36R-CC and -37R-CC and was identified by the occurrence of common *Reticulofenestra bisecta, Zygrhablithus bijugatus,* and by the HO of *Pontosphaera enormis* in Sample 149-900A-37R-CC. The HO of *Sphenolithus ciperoensis* in Sample 149-900A-39R-3, 147 cm, defines the top of Zone NP25. The interval from this sample to Sample 149-900A-44R-CC was placed in Zone NP25. Sample 149-900A-39R-CC contains common *Sphenolithus ciperoensis* and very rare *Sphenolithus distentus;* the absolute HO of *Sphenolithus distentus* was not used at Site 900 to define the top of Zone NP24, because of its very rare, sporadic occurrence throughout Zone NP25. Instead, the zonal NP24/NP25 boundary was defined by the highest common occurrence of *Sphenolithus distentus* in Sample 149-900A-44R-CC. The NP23/NP24 boundary was placed between Samples 149-900A-47R-CC and -48R-CC on the basis of the change in dominance from common *Sphenolithus distentus* to common *Sphenolithus predistentus.* This event was substituted for the LO of *Sphenolithus ciperoensis* (Sample 149-900A-44R-CC), the common marker for this boundary. The LO of *Sphenolithus distentus* was observed in Sample 149-900A-48R-CC. The interval below, down to Sample 149-900A-51R-4, 143 cm, was assigned to Zone NP23 on the presence of a few, large *Helicosphaera compacta,* common *Sphenolithus predistentus,* and on the absence of *Reticulofenestra umbilica.* The LO of *Coronocyclus nitescens* occurs in Sample 149-900A-49R-CC. Zones NP22 and NP21 from the lower Oligocene were not observed, and an unconformity was interpreted as existing between Samples 149-900A-51R-4, 143 cm (Zone NP23), and -51R-CC at 7 cm (Zone NP19/20).

Eocene

The interval 149-900A-51R-CC, 7 cm, to -54R-CC was assigned to Zone NP19/20, as indicated by the highest co-occurrence of rare *Discoaster saipanensis,* very rare *Discoaster barbadiensis, Cyclococcolithus formosus, Reticulofenestra hillae, Reticulofenestra umbilica,* and by the acme of *Clausicoccus subdistichus.* The HOs of *Discoaster saipanensis* and *Discoaster barbadiensis* were used to define the Eocene/Oligocene boundary. Zones NP19 and NP20 were not separated because the LO of *Sphenolithus pseudoradians,* the zonal marker for the base of NP20, could not be used at Hole 900A because it was also observed in Zone NP17. *Sphenolithus pseudoradians* was not observed at other sites during Leg 149. The LO of *Isthmolithus recurvus* occurs in Sample 149-900A-54R-CC and marks the NP18/NP19 boundary. The NP17/NP18 boundary was defined by the HO of *Sphenolithus obtusus* in Core 149-900A-54R-CC. The LO of large *Reticulofenestra bisecta* occurs in Sample 149-900A-57R-CC. *Chiasmolithus solitus, Sphenolithus spiniger,* and *Clausicoccus vanheckae* appear in Sample 149-900A-59R-CC and indicate the top of Zone NP16. Sample 149-900A-60R-CC contains the HOs of *Neococcolithes dubius, Pseudotriquetrorhabdulus inversus, Pyrocyclus inversus,* and numerous species of genera *Micrantholithus, Pemma,* and *Braarudospohaera.* The HOs of *Nannotetrina alata* and *Discoaster wemmelensis* were observed in Sample 149-900A-67R-CC. Sample 149-900A-68R-CC was assigned to Zone NP15, as indicated by the absence of *Reticulofenestra umbilica. Chiasmolithus gigas* occurs in Sample 149-900A-69R-CC. The HO of *Discoaster lodoensis* in Sample 149-900A-75R-CC defines the top of Zone NP14.

The early Eocene Zones NP13 to NP10 have not yet been observed at Site 900. The sediments in Cores 149-900A-76R and-77R are composed mostly of noncalcareous brown claystone layers separated by rare calcareous claystones that contain few-to-common calcareous nannofossils.

Paleocene

Upper Paleocene sediments from Zone NP9 occur in Sample 149-900A-78R-CC and represent the oldest Cenozoic sediments containing calcareous nannofossils that were recovered during Leg 149. The assemblage contains abundant and well-preserved calcareous nannofossils. The presence of common *Discoaster multiradiatus,* few *Fasciculithus bobii, F. hayii, Prinsius martinii,* and *Campylosphaera eodela* (>7.0 µm) indicates the middle of Zone NP9.

Foraminifers

Planktonic foraminifers in core-catcher samples from Hole 900A were examined to establish preliminary ages for the sediments (Fig. 16). The number of planktonic foraminifers was generally high in the upper sections of the hole; most of the samples yielded a high-diversity planktonic foraminiferal assemblage having good to moderate preservation (Table 6). Fewer, and more poorly preserved, planktonic foraminifers were present in the lower sections of Hole 900A. Similar patterns were observed in the benthic foraminiferal assemblages.

Hole 900A

Samples 149-900A-1R-CC and -2R-CC are characterized by the presence of *Globorotalia truncatulinoides* and can be assigned to

Table 6. Distribution of planktonic foraminifers in Hole 900A.

Age	Zone	Core	Abundance	Preservation	*Beela digitata*	*Globigerinoides extremus*	*G. ruber alba*	*G. trilobus*	*Globorotalia crassaformis crassaformis*	*G. hirsuta*	*G. inflata*	*G. punticulata*	*G. scitula scitula*	*G. truncatulinoides*	*Neogloboquadrina acostaensis*	*N. pachyderma*	*Orbulina universa*	*Globigerinoides conglobatus*	*Sphaeroidinella dehiscens*	*Globorotalia tosaensis*	*Orbulina suturalis*	*Neogloboquadrina dutertrei*	*Pulleniatina obliquiloculata*	*Globigerinoides obliquus*	*Beela praedigitata*	*Globigerina decoraperta*	*G. nepenthes*	*Globigerinita naparimaensis*	*Sphaeroidinellopsis paenedehiscens*	*Globigerinoides subquadratus*	*Globorotalia incompta*	*Sphaeroidinellopsis seminulina*	*Globorotalia conoidea*	*Globoquadrina dehiscens*	*G. venezuelana*	*Sphaeroidinellopsis disjuncta*	*Globorotalia menardii* s.l.	*Globorotalia acrostoma*	*G. mayeri*	*G. miozea*	*G. siakensis*	*Globorotalia archeomee nardi*	*G. praescitula*	*Praeorbulina glomerosa curva*	*P. glomerosa glomerosa*
Ple.	N23	1R	A	G	R	F	F	R	R	R	C	F	F	F	F	C	F																									
		2R	A	M	R		F				C	F	R	F	F	C	F	R	R																							
l. Pli. to e. Ple.	N22–N23	3R	A	G	R		F		R		C	F		R	F	C	C			R	R																					
		4R	A	G		R	F		F		F			F	F	C	F	R		F		R	R																			
		5R	A	G		R	R		R		C		R	R		C	C	R		R		R	R																			
		6R	A	M					R		C		R	R		F	R	R				R																			
l. Pli.	N19–N21	7R	C	M			R									F	R					R		R																	
		8R	F	M				R									R			R	R	R		R																	
		9R	C	M				R	F		F	F				F	R					R																			
Pli.	N19	10R	F	M			R	R	R			F				R		R			R		R	R	R	R	R	R													
late Mio.	N16–N17	11R	F	G												R					R					R															
		12R	C	M												F	R									F															
		13R	C	M												F					R			R		F				R	R									
		14R	C	M												F	R									F					R									
		15R	C	M												R										F						F								
		16R	A	M												R										F	R	R					F	F	R	R				
ml. Mio.	N14–N17	17R	A	P																	R					F						R	F	R	R	R				
m. Mio.	N9–N11	18R	C	M																							R					R	F	R			R		R		
m. Mio.	N8	19R	A	M																							R				R		F				F	F		R	R	R	R
early Mio.	N7	20R	A	M				F																			R		R				F	R					C			
		21R	A	M				R																					R				F					F			
		22R	C	M				R																									R								
	N5–N6	23R	C	M																							R										F				
		24R	B																																						
		*25R	F	M																																					
		26R	R	M																																					
		*27R	C	M																																					
		28R	F	M																													R				R				
l. Oli. to e. Mio.	"N4"	29R	F	M																																	R				
		30R	C	M																													R				R				
		31R	A	G				F																										F			F		F		
		32R	F	M																																	R	R			
?	?	*33R	F	M																																					
		34R	C	M																																	R				
		*35R	R	M																																					
		*36R	R	M																																					
		*37R	F	M																																					
		38R	B																																						
late Oli.	P22	39R	C	M																																	R				
		40R	C	M																														R			R				
		41R	R	P																																					
		42R	F	M																														R				R			
		43R	F	P																														R			R				
		44R	F	M																																					
		45R	F	P																																					
le. Oli.	P21	46R	F	M																																					
?	?	*47R	F	M																																					
		48R	B																																						
		49R	F	M																																					
		50R	B																																						
		51R	R	M																																					
l. Eoc.–e. Oli.	P15–P19/20	52R	F	M																																					
		53R	F	M																																					
		54R	F	P																														R							

Zone N23, which is of Pleistocene to Holocene age. The co-occurrence of *Globorotalia truncatulinoides* and *Globorotalia tosaensis* in the interval 149-900A-3R-CC to -6R-CC enables us to place it in Zone N22 or the lower part of Zone N23, which is of latest Pliocene to early Pleistocene age. The interval 149-900A-7R-CC to -9R-CC is characterized by the presence of *Globorotalia inflata* and the absence of *Globorotalia tosaensis.* It can be assigned to the interval from the top of Zone N19 to Zone N21, which is of late Pliocene age. Sample 149-900A-10R-CC is characterized by the presence of *Globorotalia crassaformis crassaformis* and *Sphaeroidinellopsis paenedehiscens* and the absence of *Globorotalia inflata* and *Globigerina nepenthes;* this sample can be assigned to the upper part of Zone N19, which is of late early to early late Pliocene age. Abyssal and reworked shallow-water benthic foraminifers were present in all these samples.

The interval 149-900A-11R-CC to -16R-CC contains *Globigerina nepenthes* and *Neogloboquadrina pachyderma,* while every species variant of the *Globorotalia crassaformis* group is absent. This interval can be assigned to Zones N16 to N17, which are of late Miocene age. A hiatus was interpreted between Samples 149-900A- 10R--CC and -11R-CC, where the latest Miocene to early Pliocene age sediments (Zone N18 and the early part of Zone N19) are missing.

Sample 149-900A-17R-CC contains only the marker species *Globigerina nepenthes,* which ranges from Zone N14 to the lower part of N19. As Zone N17 had already been reached in Sample 149-900A-11R-CC, Sample 149-900A-17R-CC was assigned to Zones N14 to N17, which are of late middle to late Miocene age. Sample 149-900A-18R-CC is characterized by the presence of *Globorotalia acrostoma, Globorotalia siakensis,* and *Globorotalia mayeri* and the absence of *Praeorbulina* spp. It can be assigned to Zones N9-N11, which are of middle Miocene age. Although Zones N12 and N13 were not identified in core-catcher samples, calcareous nannofossil evidence does not support an unconformity between Samples 149-900A-17R-CC and -18R-

Table 6 (continued).

Age	Zone	Core	*Catapsydrax stainforthi*	*Globigerinoides altiaperturus*	*Globoquadrina altispira altispira*	*Praeorbulina sicana*	*Catapsydrax dissimilis*	*C. unicavus*	*Globorotalia nana/continuosa* transition	*Globigerina angustiumbilicata*	*G. tripartita*	*Globorotalia kugleri*	*Globoquadrina baroemoenensis*	*Globigerinoides* spp.	*G. praedehiscens*	*Cassigerinella chipolensis*	*Globigerina praebulloides* s.l.	*Globigerinoides primordius*	*Globorotaloides suteri*	*Globigerina ciperoensis angulisuturalis*	*Globorotalia opima nana*	*Globigerina ciperoensis ciperoensis*	*Globorotalia nana*	*Globigerina cryptomphala*	*G. eocaena*	*Globigerina corpulenta*	*G. yeguaensis*	*Globorotalia increbescens*	*Globigerinatheka index* s.l.	*Globorotalia cerroazulensis cocoaensis*	*G. cerroazulensis cerroazulensis*	*G. cerroazulensis pomeroli*	*Globorotalia centralis*	*Morozovella spinulosa*	*Truncorotaloides rohri*	*T. topilensis*	*Globigerina senni*	*Globigerinatheka mexicana barri*	*Acarinina bullbrooki*	*Morozovella lehneri*	*Pseudohastigerina micra*	*Globigerinatheka index index*	*Morozovella aragonensis*	*Acarinina pentacamerata*	*A. broedermanni*	*Globigerina triloculinoides*	*Acarinina mckannai*	*A. primitiva*	*Morozovella aequa*	*Planorotalites pseudomenardii*
Ple.	N23	1R																																													
		2R																																														
l. Pli. *to* e. Ple.	N22–N23	3R																																													
		4R																																													
		5R																																													
		6R																																													
l. Pli.	N19–N21	7R																																												
		8R																																													
		9R																																													
Pli.	N19	10R																																													
late Mio.	N16–N17	11R																																													
		12R																																													
		13R																																													
		14R																																													
		15R																																													
		16R																																													
ml. Mio.	N14–N17	17R																																													
m. Mio.	N9–N11	18R																																												
m. Mio.	N8	19R																																												
early Mio.	N7	20R	R	R	R	R																																									
		21R																																													
		22R																																													
	N5–N6	23R			R		F	R																																						
		24R																																													
		*25R																																													
		26R						R	R																																					
		*27P																																													
		28R																																													
l. Oli. to e. Mio.	"N4"	29R					R		R	R	R																																			
		30R											R	R																																
		31R					R	R	C				F		F	R	R	R	F	R																										
		32R							R				R					R																												
?	?	*33R																																												
		34R								R						R																														
		*35R																																													
		*36R																																													
		*37R																																													
		38R																																													
late Oli.	P22	39R							R	R							R	R																												
		40R							R	F								F																												
		41R						R																																						
		42R								R								R			R	R																								
		43R					R											R				R																								
		44R							R									R		R			R	R																						
		45R																F		R			R	R																						
le. Oli.	P21	46R					R													R	R		R		R	R																		
?	?	*47R																																												
		48R																																													
		49R						R																		R																				
		50R																																													
		51R																								R																				
l. Eoc.–e. Oli.	P15–P19/20	52R																								F	R	R																		
		53R									R															R			R																	
		54R									R						R									R																				

CC. Sample 149-900A-19R-CC is characterized by the presence of *Praeorbulina glomerosa curva* and *P. glomerosa glomerosa* and can be assigned to Zone N8, which is of early middle Miocene age.

The co-occurrence of *Praeorbulina sicana* and *Catasydrax stainforthi* and the absence of *Praeorbulina glomerosa glomerosa* in Sample 149-900A-20R-CC allow us to assign this sample to the upper part of Zone N7, which is of early Miocene age. Samples 149-900A-21R-CC and -22R-CC do not contain *Praeorbulina sicana,* thus these samples were placed in the lower part of Zone N7. The interval 149-900A-23R-CC to -27R-CC is marked by the presence of *Catapsydrax dissimilis* and *Catapsydrax unicavus,* thereby allowing us to assign it to Zones N5 to N6, which are of early Miocene age. Within this interval, Sample 149-900A-24R-CC is barren of planktonic foraminifers.

The interval 149-900A-28R-CC to -32R-CC contains *Globorotalia kugleri.* This species defines Zone "N4," which is of latest Oligocene to early Miocene age. The interval 149-900A-33R-CC to -38R-CC contains primarily very small planktonic foraminifers, none of which is a marker species. Within this interval, Sample 149-900A-34R-CC contains *Globigerinoides* spp., and Sample 149-900A-38R-CC is barren of planktonic foraminifers.

The interval 149-900A-39R-CC to -41R-CC is characterized by the absence of both *Globorotalia kugleri* and *Globigerinoides* spp. and has been assigned to the upper part of Zone P22, which is of late Oligocene age. The top of the interval 149-900A-42R-CC to -45R-CC is marked by the presence of *Globorotalia opima nana* and *Globigerina ciperoensis angulisuturalis;* this interval can be placed in the lower part of Zone P22, which is of late Oligocene age. Sample 149-900A-46R-CC contains *Globigerina cryptomphala* and *Globigerina ciperoensis angulisuturalis* and was assigned to Zone P21, which is of late early to early late Oligocene age. Samples 149-900A-47R-CC, -49R-CC, and -51 R-CC contain no zonal markers. Samples 149-900A-48R-CC and -50R-CC are barren of planktonic foraminifers.

The interval 149-900A-52R-CC to -54R-CC contains an assemblage of *Globorotalia increbescens, Globigerina yeguaensis, Glo-*

Table 6 (continued).

Age	Zone	Core	Abundance	Preservation	*Beela digitata*	*Globigerinoides extremus*	*G. ruber alba*	*G. trilobus*	*Globorotalia crassaformis crassaformis*	*G. hirsuta*	*G. inflata*	*G. puncticulata*	*G. scitula scitula*	*G. truncatulinoides*	*Neogloboquadrina acostaensis*	*N. pachyderma*	*Orbulina universa*	*Globigerinoides conglobatus*	*Sphaeroidinella dehiscens*	*Globorotalia tosaensis*	*Orbulina suturalis*	*Neogloboquadrina dutertrei*	*Pulleniatina obliquiloculata*	*Globigerinoides obliquus*	*Beela praedigitata*	*Globigerina decoraperta*	*G. nepenthes*	*Globigerinita naparimaensis*	*Sphaeroidinellopsis paenedehiscens*	*Globigerinoides subquadratus*	*Globorotalia incompta*	*Sphaeroidinellopsis seminulina*	*Globorotalia conoidea*	*Globoquadrina dehiscens*	*G. venezuelana*	*Sphaeroidinellopsis disjuncta*	*Globorotalia menardii* s.l.	*Globorotalia acrostoma*	*G. mayeri*	*G. miozea*	*G. siakensis*	*Globorotalia archeomee nardi*	*G. praescitula*	*Praeorbulina glomerosa curva*	*P. glomerosa glomerosa*
lm. Eoc.	P15–P17	55R	F	M																													R								
middle	P14	56R	C	M																																					
Eocene		57R	C	M																																					
		58R	F	P																																					
	?	59R	B																																						
		60R	B																																						
		61R	B																																						
	P12–P13	62R	F	P																																					
		63R	B																																						
		*64R	R	P																																					
		65R	F	M																																					
		66R	F	P																																					
		*67R	R	P																																					
		68R	B																																						
		69R	R	P																																					
	?	70R	B																																						
	P11	71R	F	M																																					
		72R	F	P																																					
	P10	73R	C	M																																					
		74R	F	P																																					
?	?	75R	B																																						
		76R	B																																						
		77R	X																																						
l. Pal	P4	78R	C	P																																					
?	?	79R	X																																						
			X																																						

Notes: Age:1. Pal. = late Paleocene; lm. Eoc. =late to middle Eocene;1. Eoc.-e. Oli = middle Eocene to early Oligocene; le. Oli = late early to early late Oligocene; late Oli. = late Oligocene; 1. Oli. to e. Mio. =late Oligocene to early Miocene; early Mio. = early Miocene; m. Mio. = middle Miocene; ml. Mio. =late middle to late Miocene; late Mio. = late Miocene; Pli. = Pliocene; 1. Pli. = late Pliocene; 1. Pli. to e. Ple. = late Pliocene to early Pleistocene; Ple. = Pleistocene. A "*" in the "Core" column indicates that core-catcher sample contained only juvenile planktonic foraminifers or no marker species. Abundance: A = abundant; C = common; F = few; R = rare; B = barren; X = core-catcher sample was sandstone; XX = sample contained downhole contaminants. Preservation: G = good; M = moderate; P = Poor.

bigerina tripartita, Globigerina corpulenta, and relatively few *Globigerina eocaena.* The presence of *Globorotalia increbescens* allows us to assign this interval to somewhere within Zone P15 to the lower part of Zones P19/20, which are of latest middle Eocene to early early Oligocene age.

The presence *of Globorotalia cerroazulensis cocoaensis* and *Globigerinatheka index* s.1. in Sample 149-900A-55R-CC restricts it to Zones P15 to P17, which are of latest middle to late Eocene age. The first downhole occurrence of species belonging to the *Globorotalia cerroazulensis* group, which are markers for the top of the Eocene, may be depressed in this section. The interval 149-900A-56R-CC to -58R-CC is marked by the presence of *Truncorotaloides rohri* and *Truncorotaloides topilensis* at the top, *Globigerina tripartita* near the base, and *Globorotalia cerroazulensis cerroazulensis* at the base. This interval can be assigned to Zone P14, which is of late middle Eocene age. Samples 149-900A-59R-CC, -60R-CC, and -61R-CC are barren of planktonic foraminifers. The interval 149-900A-62R-CC to -69R-CC contains *Truncorotaloides rohri* and *Truncorotaloides topilensis,* but no *Globorotalia cerroazulensis cerroazulensis. Morozovella aragonensis* has not yet been observed. This interval can be assigned to Zones P12 and P13, which are of middle Eocene age. Within this interval, Samples 149-900A-63R-CC and -64R-CC are barren of planktonic foraminifers.

Sample 149-900A-70R-CC is barren of planktonic and calcareous benthic foraminifers. Relatively rare arenaceous benthic foraminifers (*Glomospira* spp. and *Bathysiphon* spp.) and ichthyoliths are present.

The interval 149-900A-71R-CC to -72R-CC is marked by the presence of *Morozovella aragonensis* at the top and *Morozovella lehneri* at the base; this interval can be placed in Zone P11, which is of middle Eocene age. *Acarinina pentacamerata* was first observed in Sample 149-900A-72R-CC. The interval 149-900A-73R-CC to -74R-CC is characterized by the presence of *Morozovella aragonensis* and the absence of *Morozovella lehneri. Acarinina soldadoensis* was not recorded. This interval can be assigned to Zone P10, which is of early middle Eocene age. Samples 149-900A-75R-CC and -76R-CC are barren of planktonic foraminifers. Sample 149-900A-77R-CC is a hard sandstone and could not be disaggregated.

Sample 149-900A-78R-CC contains *Planorotalites pseudomenardii,* which defines Zone P4 and is of late Paleocene age. Sample 149-900A-79R-CC contains relatively few arenaceous benthic foraminifers (*Glomospira charoides* and *Ammodiscus* spp.), one specimen of a calcareous benthic foraminifer (*Cibicidoides* spp.), and relatively rare radiolarians and ichthyoliths. The presence of younger planktonic foraminiferal species in this core-catcher sample is the result of downhole contamination; thus, no age was assigned to this sample.

PALEOMAGNETISM

We drilled about 740 m of sediment at Site 900. However, only from 30.4 to 145.3 mbsf, which was composed of the nannofossil ooze and clay of Unit I (see "Lithostratigraphy" section, this chapter), were the recovered cores sufficiently magnetized to permit alternating field (AF) demagnetization and measurements using the cryogenic magnetometer. Below 151.3 mbsf (Cores 149-900A-18R through -79R), sediments are very weakly magnetized (generally between 1×10^{-4} and 2×10^{-4} A/m). Consequently, only natural remanent magnetization was measured in these cores. We measured sections of the basement rocks at 2- to 5-cm intervals, using the pass-through cryogenic magnetometer. Thus far, a total of nine discrete samples has been progressively AF demagnetized to verify the reversed magnetizations indicated by the cryogenic magnetometer measurements.

Magnetic Properties

The quality of paleomagnetic data depends strongly on the lithology of the recovered material; thus, the discussion here of magnetic

Table 6 (continued).

Age	Zone	Core	*Catapsydrax stainforthi*	*Globigerinoides altiaperturus*	*Globoquadrina altispira altispira*	*Praeorbulina sicana*	*Catapsydrax dissimilis*	*C. unicavus*	*Globorotalia nana/continuosa* transition	*Globigerina angustiumbilicata*	*G. tripartita*	*Globorotalia kugleri*	*Globoquadrina baroemoenensis*	*Globigerinoides* spp.	*G. praedehiscens*	*Cassigerinella chipolensis*	*Globigerina praebulloides* s.l.	*Globigerinoides primordius*	*Globorotaloides suteri*	*Globigerina ciperoensis angulisuturalis*	*Globorotalia opima nana*	*Globigerina ciperoensis ciperoensis*	*Globorotalia nana*	*Globigerina cryptomphala*	*G. eocaena*	*Globigerina corpulenta*	*G. yeguaensis*	*Globorotalia increbescens*	*Globigerinatheka index* s.l.	*Globorotalia cerroazulensis cocoaensis*	*G. cerroazulensis cerroazulensis*	*G. cerroazulensis pomeroli*	*Globorotalia centralis*	*Morozovella spinulosa*	*Truncorotaloides rohri*	*T. topilensis*	*Globigerina senni*	*Globigerinatheka mexicana barri*	*Acarinina bullbrooki*	*Morozovella lehneri*	*Pseudohastigerina micra*	*Globigerinatheka index index*	*Morozovella aragonensis*	*Acarinina pentacamerata*	*A. broedermanni*	*Globigerina trilocultinoides*	*Acarinina mckannai*	*A. primitiva*	*Morozovella aequa*	*Planorotalites pseudomenardii*
lm. Eoc.	P15–P17	55R									R							R						R				R	R																
middle	P14	56R																R					R	R				R	R	R	R	R	R	F	R										
Eocene		57R									R																					R	R		R										
		58R																							R										R		R								
	?	59R																																												
		60R																																												
		61R																																												
	P12–P13	62R																															R	R	R		R	R	R						
		63R																																												
		*64R																																												
		65R																																										R		
		66R																															R	R		R			R	R	R				
		*67R																																												
		68R																																												
		69R																															R	R		R		R							
	?	70R																																												
	P11	71R																										R					R					R				R				
		72R																															F					R	R	F		R				
	P10	73R																															F	R				R		R		R	R	R		
		74R																															F			R		R				R	R	R		
?	?	75R																																												
		76R																																												
		77R																																												
l. Pal	P4	78R																																										R	R	R	R
?	?	79R																																												

properties at Site 900 is organized on the basis of lithology. From Cores 149-900A-1R to -4R, we recovered mud-dominated turbidites. These cores were too mechanically disturbed by drilling to allow for meaningful measurements.

Cores 149-900A-5R through -17R are mainly nannofossil clay and ooze and have a strong magnetic signal (NRM intensities typically in the range 1 to 10 mA/m) that was easily measured. The whole-core pass-through measurements agree well with those from the discrete samples. Figure 17 shows typical examples of AF demagnetization diagrams for the discrete samples. The magnetic behavior of these sediments is relatively straightforward, with easily identified characteristic magnetizations in the orthogonal demagnetization diagrams.

Except for two short intervals, the sediments from 181.5 to 748.9 mbsf in Unit II (see "Lithostratigraphy" section, this chapter) were almost entirely characterized by weak magnetic remanence (<0.5 mA/m). We could not measure these sediments accurately on board the ship. We hope that land-based studies can successfully analyze the weak remanence in these sediments.

Below 748.9 mbsf, the recovered cores are fine-grained, metamorphosed' mafic rocks (see "Igneous and Metamorphic Petrology and Geochemistry" section, this chapter) and have not yet provided any reliable magnetic results, mainly because of their weak magnetizations.

Magnetostratigraphy

The best evidence for polarity reversals occurs in the interval from the upper part of Core 149-900A-5R to the top section of Core 149-900A-17R (30.4-145.3 mbsf). The combined shipboard paleomagnetic and biostratigraphic data (see "Biostratigraphy" section, this chapter) have enabled us to construct a tentative magnetostratigraphy for the sediments in this interval (Fig. 18). The Brunhes/Matuyama boundary was not observed in Hole 900A. However, because biostratigraphic samples between 12.0 and 65.5 mbsf have been tentatively assigned ages in the range from 0.8 to 2.6 Ma, the observed predominantly negative inclinations in this interval suggest that these sediments were deposited within the Matuyama Chron. Thus, the shift in polarity from reversed to normal at about 65.0 mbsf may represent the Matuyama/Gauss boundary (2.6 Ma). In addition, the preliminary biostratigraphic data suggest that sediments at 46.9 mbsf may be of late Pliocene age. This information suggests that the shift of polarity from reversed to normal at about 49.0 mbsf corresponds to the upper Olduvai boundary (1.88 Ma). Finally, the upper boundaries of both nannofossil Zone NN15 and foraminiferal Zone N19 have been tentatively placed at about 80 mbsf, which would suggest that the Gauss/Gilbert boundary (3.5 Ma) should occur in the vicinity of this depth. As mentioned above, there are two exceptions within Unit II where the sediments are not too weakly magnetized. These occur in Cores 149-900A-51R (469.9 mbsf) and -77R (720.0 mbsf). Interestingly, pass-through measurements revealed that sediments at both these two depths are reversely magnetized. Although biostratigraphic evidence suggests that they may be of early Oligocene and early Eocene age, respectively, so far we have been unable to relate the reversed polarities to the geomagnetic reversal time scale.

Magnetic Susceptibility

The magnetic susceptibility of all cores for Hole 900A was measured at intervals of 3 cm (Fig. 19). In general, the whole-core susceptibility measurements vary in similar fashion to the NRM signals. For Unit I, the magnetic susceptibilities have average values consistently above 4×10^{-4} SI units, similar to those observed at earlier Leg 149 sites. Average susceptibilities of the weakly magnetized sediments of Unit II and the metamorphosed mafic rocks in the basement are only about 2×10^{-4} SI units. The two peaks of susceptibility at about 470 and 720 mbsf correspond to Cores 149-900A-51R and -77R, respectively, which also displayed relatively high magnetizations.

IGNEOUS AND METAMORPHIC PETROLOGY AND GEOCHEMISTRY

Introduction

Drilling at Site 900 encountered the top of a series of metamorphosed and brecciated mafic rocks at 748.9 mbsf, beneath sediments of Pleistocene to late Paleocene age. A total of 56.1 m of these mafic

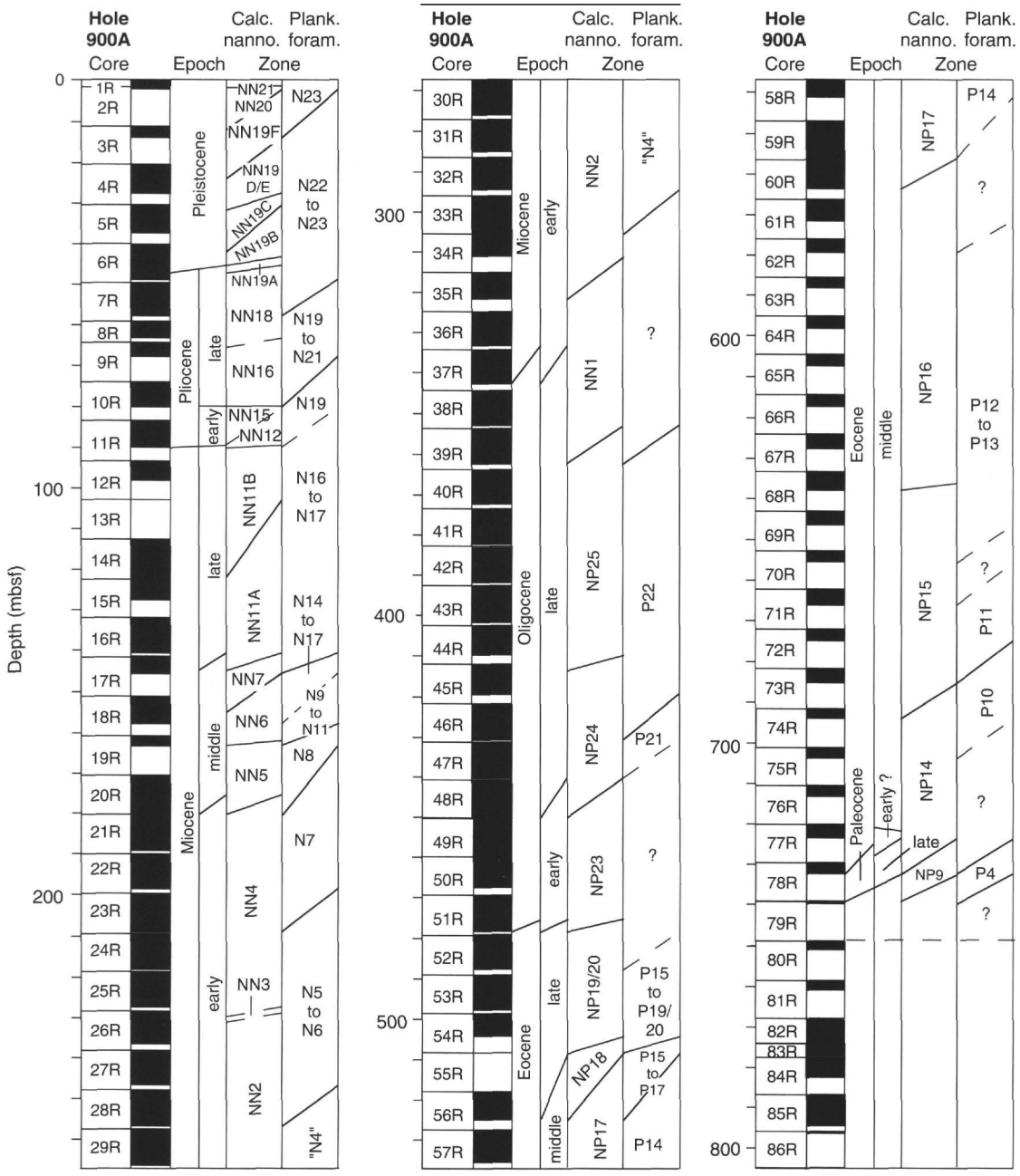

Figure 16. Summary of planktonic microfossil zones from Site 900. The calcareous nannofossil zonations are from Martini (1971), with subzones of Rio, Fornaciari, et al. (1990) for the late Pliocene/Pleistocene. All cores below Core 149-900A-79R were metamorphosed mafic rocks.

rocks was drilled and 27.71 m of material was recovered before the hole was abandoned at a depth of 805 mbsf, giving a recovery in the basement section of the hole of 49.4%.

This succession is composed of mainly fine-grained metamorphosed mafic rocks showing intense deformational features. Many sections are now highly brecciated, separated from nonbrecciated parts by sharp contacts (Fig. 20). The age of the rocks is uncertain beyond the obvious fact that they are pre-late Paleocene.

Macroscopic Core Descriptions

Core recovery in Core 149-900A-79R was poor, and the nature of the sediments and their contact relationships to the underlying mafic rocks in Core 149-900A-80R are unknown. The first hard-rock sample recovered in Section 149-900A-80R-1 is a fragment of amphibolite (drilling dropstone?). Below this, extending downward to the base of the drilled section, is a succession of fine- and coarse-grained mafic rocks that have been cut by veins and 1-cm to 4-m (Core 149-900-84R) zones of brecciation. The color of the whole section varies from a light to a more frequently dark greenish gray grading toward brownish gray at the bottom.

Intervals 149-900A-82R-5, 0-38 cm, and -83R-2, 50-90 cm, display a marked planar fabric that is the result of alternating discontinuous mafic and felsic bands, each having a maximum thickness of 8 mm. This banding gives these intervals a distinctive "flasered" appearance (Fig. 21). Though less obvious, this same planar fabric characterizes the fine-grained massive-appearing material, in bands less than 1 mm thick (Fig. 22).

The coarser-grained intervals grade rapidly over a few millimeters into finer-grained banded zones, or are limited by brecciated zones or

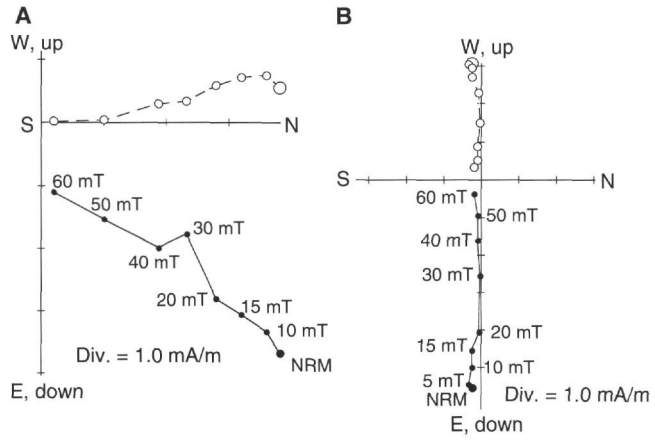

Figure 17. Representative vector end-point diagram showing the results of AF demagnetization for discrete Samples 149-900A-5R-1, 96-98 cm (**A**), and -8R-3, 72-74 cm (**B**). Open and solid circles represent vector end points projected onto the vertical and horizontal planes, respectively.

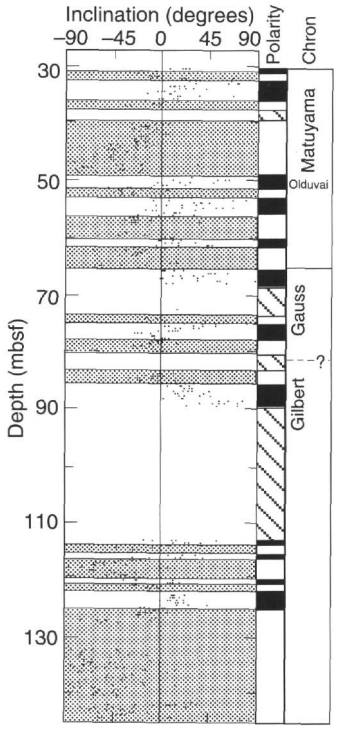

Figure 18. Plot of magnetic inclinations for Cores 149-900A-5R to -17R (after AF demagnetization at 15 mT). Gray shaded areas outline reversed polarity intervals. The tentative interpretation of the polarity, aided by biostratigraphic dates, is shown at right; zones in black (white) correspond to normal (reversed) polarity; hachured zones represent uncertain polarity intervals.

a sharp contact with a matrix that displays differently oriented dipping layers (Interval 149-900A-83R-2, 105-115 cm). These grain-size variations might result from varying degrees of deformation.

Late-stage brecciated zones disrupt approximately 37% of the recovered core. Their distribution is not homogeneous and Cores 149-900A-80R, -81R, and -84R are the most intensely brecciated with, respectively, 68%, 53%, and 70% of their length brecciated (vs. 16% to 38% for the remaining cores). This brecciation may be progressive: the first stage shows little displacement of blocks (Interval 149-900A-84R, 45-80 cm) and corresponds to an increase in veining frequency.

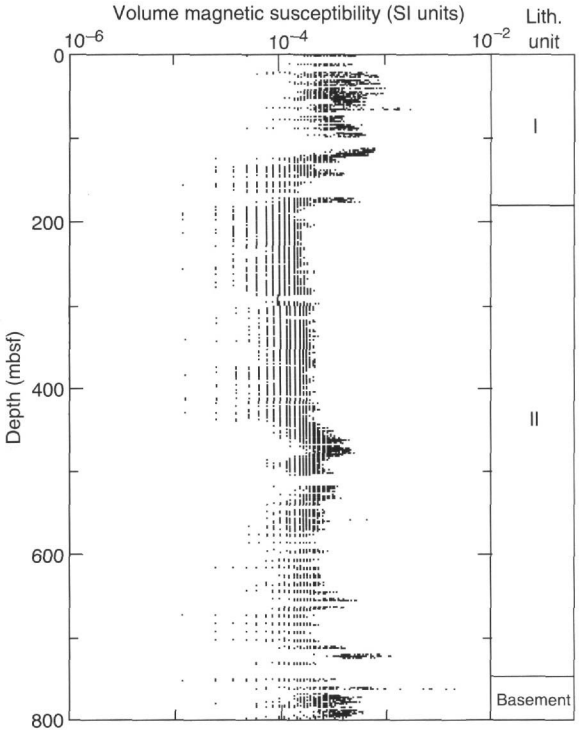

Figure 19. Magnetic susceptibility measurements in Hole 900A.

More highly brecciated zones contain sparse clasts set in an ultrafine varicolored matrix (Fig. 23).

Veining

The cores are cut by a large number of veins and fractures that in places represent more than 20% of the rock. Although some variation is visible, one can observe the same paragenetic sequence of veins throughout this section of the core. This sequence is listed here, starting with the earliest veins:

1. Fine, hairlike fractures with marked marginal zones of black (iron-oxide?) alteration having overall width of 1 to 5 mm.
2. Abundant yellow brown epidote occurring in well defined veins 1 to 10 mm wide, and in more diffuse irregular patches that replace the groundmass mineralogy.
3. Narrow (typically 1-3 mm) veins of white or pinkish zoisite or clinozoisite.
4. Clearly defined glassy appearing veins of gray calcite, often associated with the late-stage brecciation of the matrix.

The most recent veining and brecciation associated with calcite (Type 4 above) is preferentially developed in the upper part and base of the basement section, but extends more rarely through the entire mafic interval. The other vein-types are more uniformly developed throughout this section.

The breccia is frequently deformed, particularly near the contact of blocks. In that case, the epidote and some chlorite veining clearly has been deformed, sheared, and broken. Rarely, even the calcite veining has been sheared (Interval 149-900A-82R-3, 74-78 cm). No intrusive or crosscutting relationships were observed, other than the late zones of brecciation and fracturing.

Petrography

Thirty-one thin sections were made of the metamorphosed mafic rocks from Hole 900A. The recovered rocks include granoblastic and cataclastic microgabbro, small amounts of cataclastic norite, plagio-

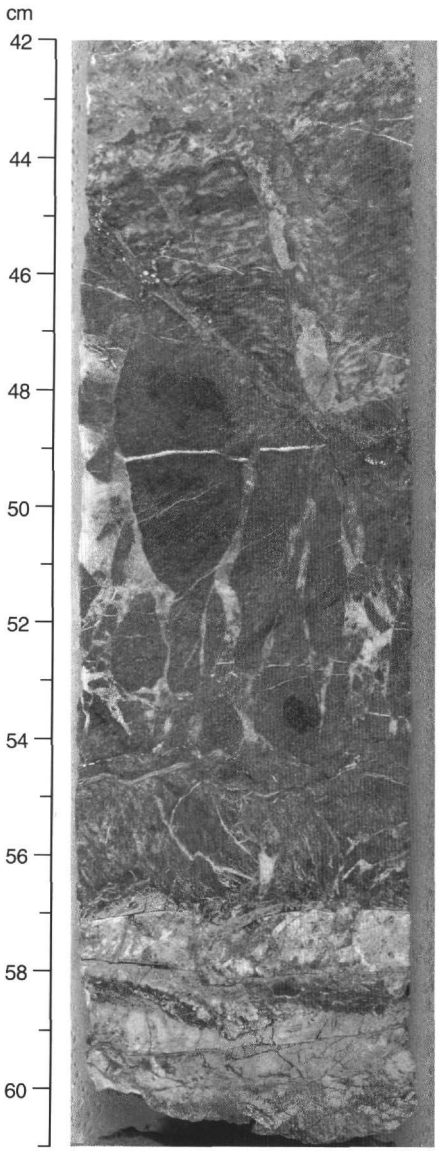

Figure 20. Fine-grained mafic metamorphic rock cut by a breccia zone with unusual rounded blobs, showing abundant late-stage veining (149-900A-82R-1, 42-61 cm).

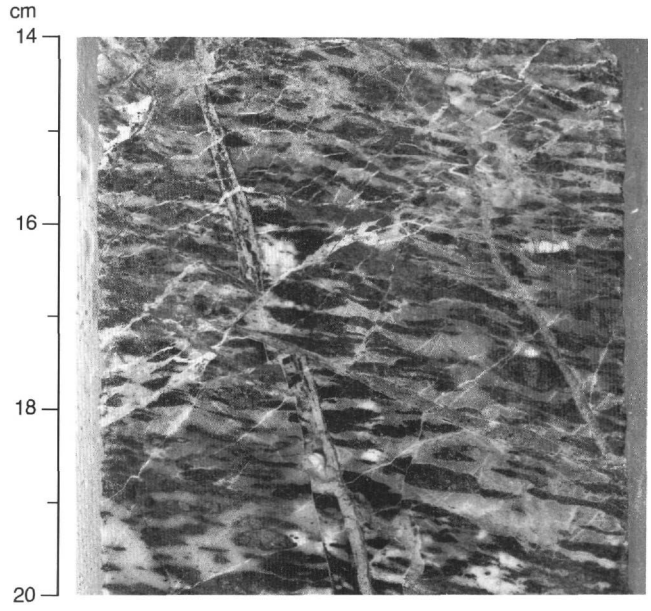

Figure 21. Coarse-grained flasered gabbro (149-900A-82R-5, 14-20 cm). Dark areas represent strained pyroxene that has been replaced by amphibole.

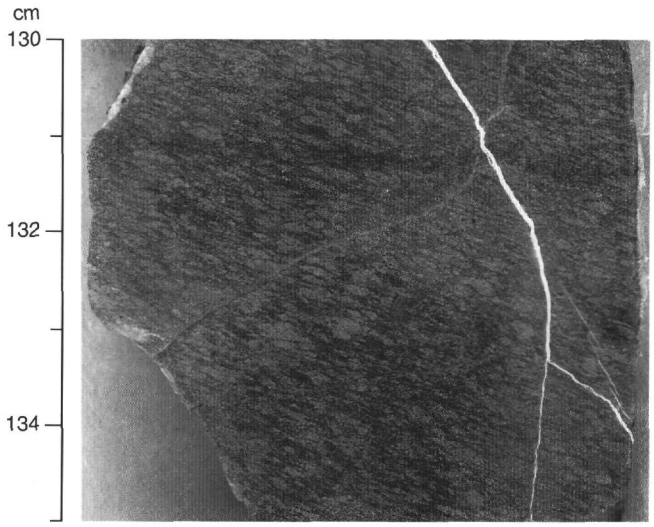

Figure 22. Discontinuous foliation in fine-grained granoblastic mafic metamorphic rock (149-900A-85R-6, 130-135 cm).

clasite, and a single (dropstone?) of garnet-bearing amphibolite. Most of the massive rocks have a porphyroclastic texture and discontinuous foliation bands (Fig. 21). Porphyroclasts of plagioclase (up to 4 mm in size) have been strongly stretched and bent (Fig. 24), and porphyroclasts of clinopyroxene (up to 1.8 mm), and sometimes orthopyroxene, have been bent and sometimes kinked. Smaller (0.1-0.2 mm) granular crystals of the same minerals mark foliation planes. The fine-grained minerals show typical recrystallization textures (i.e., triple junction boundaries and little or no strain). This kind of structure is developed in coarser-banded intervals (149-900A-83R-2, 67-70 cm), as well as in finer-grained intervals (149-900A-82R-3, 11-15 cm). In the latter, porphyroclasts may be absent, giving the rock a granoblastic texture (Sample 149-900A-85R-5, 30-32 cm).

A rough estimate of the ratio of plagioclase to pyroxene in these rocks is 60:40, but may reach 40:60. In most rocks, this mineralogy has been partially overprinted by amphibolite or greenschist facies metamorphic minerals, mainly fibrous tremolite and/or hornblende, chlorite, epidote, and zoisite or clinozoisite. The greenish cast of most of these rocks reflects this metamorphism. However, a striking feature of nearly all these rocks is the freshness of the recrystallized plagioclase, which is unaltered except in brecciated zones and in the bottom of the hole (Sections 149-900A-85R-6 and -86R-1).

Green hornblende has partially or totally replaced clinopyroxene crystals with a clear obliquity of the cleavage to the compositional banding. Because no granulation or deformation of the amphiboles is seen, this replacement post-dates the strain recrystallization (Interval 149-900A-82R-5, 0-15 cm). At the base of the recovered section, fibrous green and colorless amphiboles become major constituents of the rock (Intervals 149-900A-85R-6, 135-139cm, and-86R-1, 1-4 cm). Only in these intervals does the amphibole show some deformation.

Chlorite often has replaced what may have been orthopyroxene, surrounds the plagioclase grains, and occurs in veinlets that crosscut these layers. It clearly post-dates the green hornblende. Epidote and clinozoisite or zoisite are also ubiquitous, but more often restricted to veins. Prehnite occurs in the interval at 149-900A-84R-1, 131-132

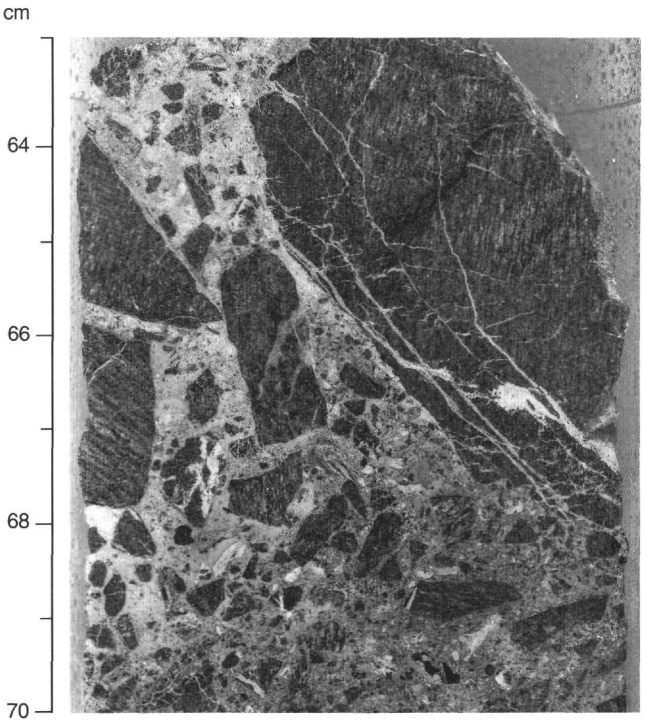

Figure 23. Brecciated zone with fine-grained, angular, mafic clasts (149-900A-81R-2, 63-70 cm).

cm. Calcite is the latest mineral to crystallize, occurring mainly in veins. It may have been preceded by zeolite (phillipsite), as in Interval 149-900A-85R-2, 60-64 cm.

Geochemistry

Major element determinations for nine metamorphosed mafic rocks are given in Table 7 and confirm the mafic nature of these rocks. However, the abundances of TiO_2 and P_2O_5 are unusually low and abundances of Al_2O_3 are high, with four samples containing more than 20% Al_2O_3. The loss-on-ignition values reflect the generally hydrated nature of the rocks and the presence of some carbonate veining.

Results of trace element analyses for 21 samples, given in Table 8, are particularly revealing in that they show the rocks contain very low concentrations of incompatible elements zirconium and yttrium. Basalts having comparable low concentrations of these elements are very rare. For example, typical mid-ocean ridge basalts contain approximately 74 ppm zirconium, whereas these rocks contain an average of 16 ppm zirconium.

The relative consistency of trace elements within the suite of analyzed samples suggests that large-scale mineralogical layering is generally absent and elemental mobility during metamorphism has been limited. The only significant vertical variation in the composition of the rocks is in the concentrations of yttrium, vanadium, and TiO_2. These elements and TiO_2 have higher abundances in Core 149-900A-81R (Fig. 25) that corresponds to an enrichment in opaque minerals noted in thin section.

Discussion

Petrographic, mineralogical, and geochemical studies suggest that these rocks are mafic in nature and have had a complex history. The earliest minerals observed are porphyroclasts of clinopyroxene, orthopyroxene, and plagioclase, without spinel or magnetite (the rocks are very weakly magnetized, see "Paleomagnetism" section, this chapter).

The earliest pyroxene/plagioclase mineralogy, preserved in some porphyroclasts, has suffered high-temperature ductile deformation

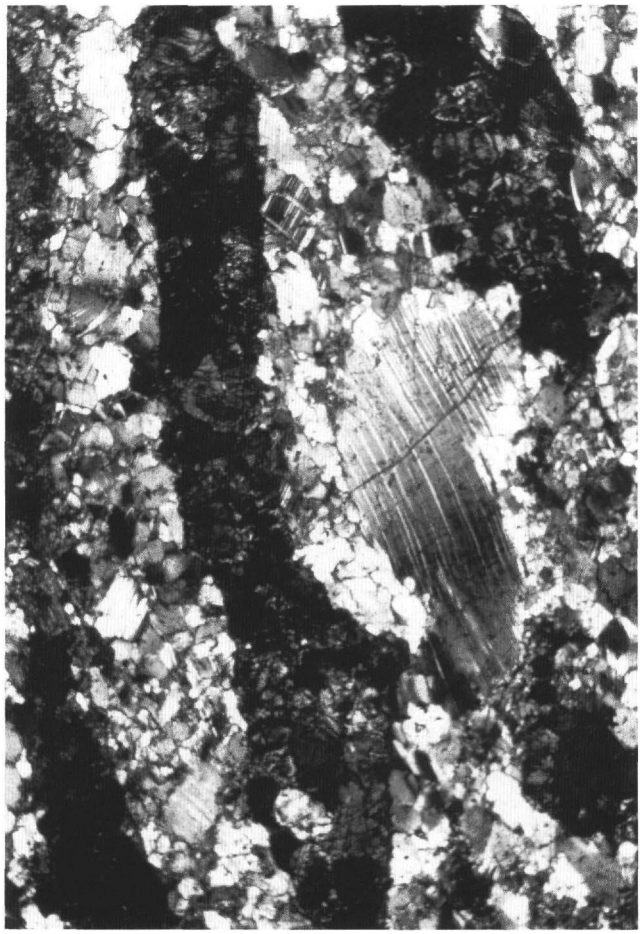

Figure 24. Photomicrograph of bent plagioclase porphyroclast in a felsic layer, which in turn has been bounded by mafic layers (149-900A-83R-2, 67-70 cm).

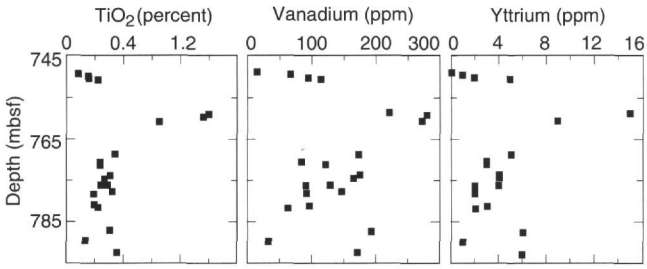

Figure 25. Vertical variation of the TiO_2, V, and Y composition of the metamorphosed mafic rocks revealing one zone with higher than normal concentrations.

accompanied by dynamic recrystallization of these two minerals. This ductile deformation was followed by a mainly static retrograde metamorphism in the amphibolite or greenschist facies with amphibole or chlorite replacing pyroxenes. A late brittle deformation event brecciated these rocks and filled voids and fractures with chlorite, epidote and clinozoisite, zeolite, then calcite.

At present, and without radiometric dates to constrain the events indicated, it is not possible to differentiate between an oceanic or continental origin for these rocks. They might be:

1. Cumulate gabbro, which either formed in the continental crust or possibly was underplated at the base of the crust, became deformed and metamorphosed during the last rifting stages of the margin (this explanation is favored by the chemical data).

Table 7. Major element composition of nine metamorphosed mafic rocks from Hole 900A.

Core, section, interval (cm)	SiO_2	TiO_2	Al_2O_3	Fe_2O_3	MnO	MgO	CaO	Na_2O	K_2O	P_2O_5	Total	LOI
80R-2, 28–31	45.98	0.12	17.36	10.17	0.41	17.10	6.29	1.41	0.41	0.03	99.28	9.27
81R-1, 16–18	53.48	1.11	14.45	8.91	0.16	11.07	7.03	3.65	0.28	0.02	100.16	2.83
82R-2, 128–132	45.81	0.19	16.47	10.60	0.14	16.82	6.55	1.95	0.23	0.00	98.76	6.50
83R-2, 88–90	47.28	0.15	20.88	7.21	0.11	9.37	10.98	1.61	0.56	0.00	98.15	3.22
84R-1, 18–21	48.14	0.23	20.35	8.38	0.13	10.74	9.23	2.07	0.74	0.01	100.01	4.95
84R-3, 135–138	50.31	0.17	22.52	5.95	0.08	8.41	10.18	1.83	0.78	0.00	100.21	3.33
85R-1, 54–56	48.17	0.27	15.17	7.99	0.14	13.05	14.52	0.99	0.05	0.00	100.35	2.70
85R-3, 50–54	46.92	0.07	21.56	9.51	0.11	12.31	7.28	0.84	1.29	0.00	99.89	5.57
85R-5, 76–79	48.67	0.32	18.24	7.03	0.12	11.11	12.49	1.70	0.29	0.00	99.97	2.98

Note: LOI = loss on ignition.

Table 8. Results of trace element analyses for 21 samples of metamorphosed mafic rocks from Hole 900A.

Core, section, interval (cm)	Depth (mbsf)	Zr	Y	Sr	Rb	Zn	Cu	Ni	Cr	V	TiO_2
80R-1, 22–25	749.1	16	0	416	10	15	0	158	10	16	757
80R-1, 70–73	749.6	14	1	309	12	19	16	113	234	67	1,472
80R-2, 28–31	750.5	11	2	172	10	62	104	391	410	95	1,603
80R-2, 43–46	750.6	13	5	188	11	45	33	239	460	115	2,173
81R-1, 16–18	758.7	22	15	213	7	39	5	200	393	220	10,117
81R-1, 83–86	759.3	24	15	245	15	40	10	225	405	279	9,788
81R-2, 74–77	760.7	15	9	191	8	59	58	162	428	271	6,596
82R-1, 87–90	768.7	17	5	236	11	17	2	184	931	173	3,459
82R-2, 128–132	770.5	12	3	135	6	29	0	361	280	85	2,356
82R-3, 52–55	771.1	18	3	339	11	17	0	218	397	122	2,377
82R-5, 54–57	773.6	24	4	437	19	17	5	192	433	176	3,122
83R-1, 46–49	774.5	12	4	116	9	32	18	210	774	166	2,632
83R-2, 81–83	776.1	17	4	247	8	21	0	176	563	131	2,784
83R-2, 88–90	776.2	17	2	248	8	23	0	245	309	92	2,461
84R-1, 18–21	777.7	17	2	306	9	35	5	230	531	147	3,201
84R-1, 81–84	778.3	14	2	281	10	33	11	194	297	92	1,913
84R-3, 77–80	781.1	15	3	290	13	24	23	170	177	97	1,922
84R-3, 135–138	781.7	16	2	302	11	13	2	196	192	64	2,275
85R-1, 54–56	787.2	15	6	167	5	33	2	261	1,074	195	3,092
85R-3, 50–54	789.6	11	1	179	17	29	0	337	52	35	1,348
85R-5, 76–79	792.5	19	6	242	7	27	4	213	737	173	3,692
Average		16	4.5	250	10	30	14	223	433	134	3,292

2. Pre-Mesozoic mafic rocks (Ordovician, Silurian, or older...) involved in the Hercynian orogeny(?), and stretched, metamorphosed, and brecciated during the Mesozoic rifting of the continental basement. Paleozoic mafic volcanic rocks subjected to probable Hercynian amphibolite facies metamorphism have been described from the Iberian Peninsula (Capdevila and Mougenot, 1988).

Microprobe analyses and isotopic studies are obviously required to constrain pressure, temperature, and ages to differentiate among these models.

STRUCTURAL GEOLOGY

Introduction

Site 900 lies about 20 km east of Site 899, above a basement high at the eastern edge of the Iberia Abyssal Plain. The basement was encountered at 748.9 mbsf, under a sedimentary sequence of Pleistocene to Paleocene age. Basement rocks were expected to be of continental origin, potentially reflecting both pre-rift and synrift deformation histories. It was also expected that the overlying sediments might display evidence for post-rift deformation along the western Iberia margin. However, few deformation structures were observed in the sedimentary sequence. Basement had been ductily deformed at high temperature and then sheared and fractured at low temperature.

Sediment Deformation

Sediments at Site 900 display a few discrete deformation structures, primarily in concentrated zones containing slumped bedding and microfaults. However, a systematic increase is seen in bedding dips through the deepest part of the sediment column.

Few structural features were observed in Hole 900A above 200 mbsf, where sediments were too soft and disturbed by drilling to preserve structures. The first evidence for structural disruption was observed between 234.1 and 240.0 mbsf (Cores 149-900A-26R and -27R), within an approximately 6-m-thick zone containing faulted and folded beds (Fig. 26) and locally high bedding dips (up to 28°). In places, microfaults offset color-banding in a normal sense; one offsets a *Zoophycus* of 0.8 cm (Fig. 27). The consolidation state of the sediments involved in this deformation is relatively uniform, suggesting that these features developed prior to sediment burial.

Slight differences in lithology above and below this zone of structural disturbance provide the basis for the subdivision of lithostratigraphic Unit II, posing the possibility that this zone of deformation marks a structural discontinuity (see "Lithostratigraphy" section, this chapter). Such a feature is not evident in seismic profiles that cross the site. Moreover, the excellent recovery through this zone (85%-90%) suggests that significant deformation features associated with a post-depositional structural discontinuity are not present. The observed deformation, therefore, is most likely to have occurred near the seafloor.

Sediments between 240 and 400 mbsf are relatively flat-lying and undisturbed. Below about 412 mbsf (Core 149-900A-45R), bedding dips steadily increase with depth to about 30° at 731 mbsf (Core 149-900A-78R) almost immediately above the basement. Although at that depth logging data indicate hole deviations of about 8°. The apparent dips are larger and thus must be real. Drilling biscuits from the deepest sediments break preferentially along the dipping bedding

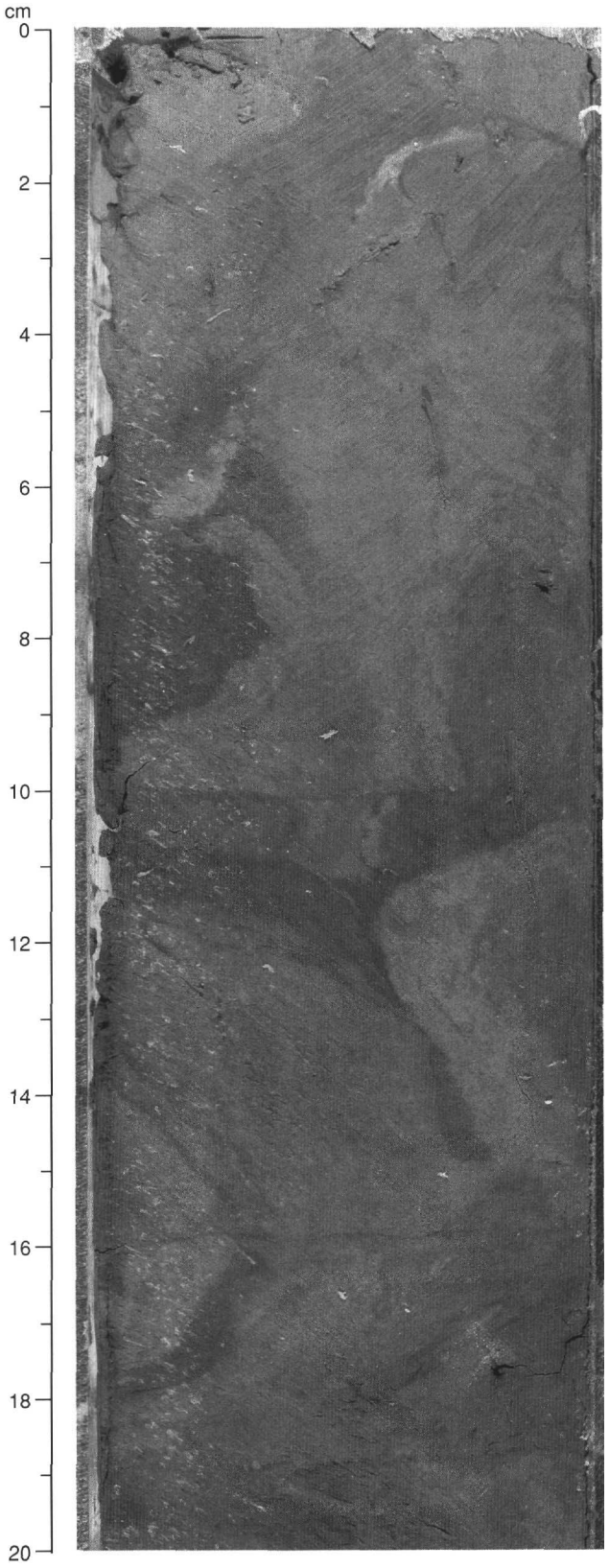

Figure 26. Folded and contorted sediments observed at Interval 149-900A-26R-6, 0-20 cm. Horizontal discontinuities represent boundaries of drilling biscuits.

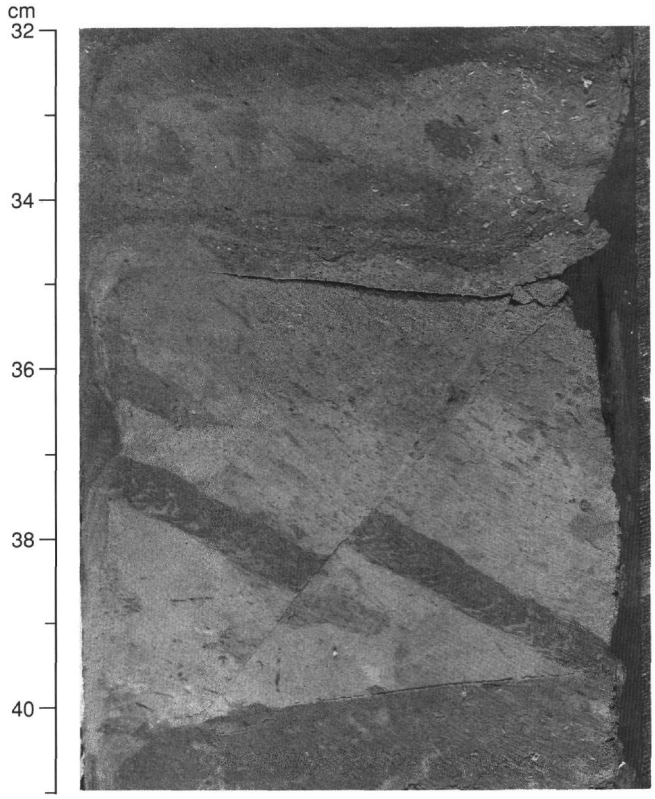

Figure 27. Microfault offsetting *Zoophycus* and color-banding at Interval 149-900A-27R-1, 32-41 cm.

planes. Rare microfaults occur in Intervals 149-900A-48R-1, 47-52 cm, to -48R-3, 130-136 cm, and display normal offsets of less than 1 cm and dips of about 47° (Fig. 28). As a result of the low magnetization of these sediments, it was not possible to orient these structures with respect to true north.

Seismic profiles that cross Site 900 do not show the high bedding dips observed in the deeper cores. These dips may reflect local structures associated with the basement high, but this cannot be established at this time.

Basement Rocks

The basement at Site 900A is made of fine- to locally coarse-grained metamorphic mafic rocks. Two main events of deformation can be distinguished in these rocks: (1) a high-temperature ductile deformation characterized by a well-marked foliation and (2) a later, low-temperature event expressed as narrow shear zones, with intense fracturing that evolves locally into brecciation.

High-temperature Ductile Deformation

This deformation is characterized macroscopically by a clear foliation marked by alternating narrow dark green layers and gray to pale orange elongated lenses. A thin section of a fresh, fine-grained facies (Sample 149-900A-85R-1, 22 cm) shows that the dark layers are made of plagioclase feldspar and the gray ones of pyroxene crystals. The rock texture is porphyroclastic to granoblastic. The plagioclase has been recrystallized in 0.5-mm-sized crystals, some having undulatory extinctions, which locally surround some relict-strained porphyroclasts. A few strained pyroxene porphyroclasts have been preserved in clusters, where they are more or less recrystallized. Such a deformation is classically described in flaser-gabbros. In some places, the rock displays a larger grain size, with porphyroclasts of 5 mm that have been

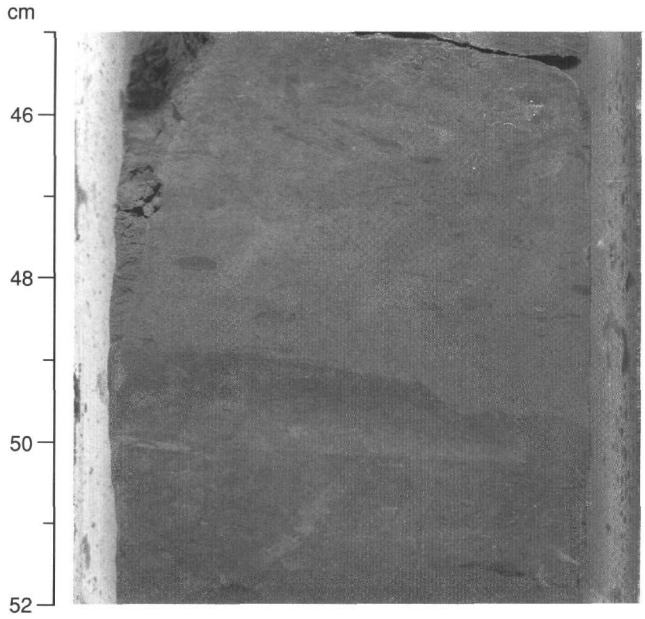

Figure 28. Microfault offsetting the color-banding at Interval 149-900 A-48R-1, 45-52 cm.

isolated in elongated bands of smaller pyroxene crystals that alternate with bands of fine-grained recrystallized plagioclase (e.g., Interval 149-900A-83R-2, 65-100 cm; Fig. 29). However, the heterogeneity of the grain-size distribution is also illustrated in such intervals, where layers of fine-grained facies are parallel to the foliation. This foliation is present in the overall basement section, even though it is hardly visible in some extremely fine-grained facies. It generally dips from 15° to 45°, but is locally higher and even becomes subvertical in Interval 149-900A-81R-2, 0-28 cm. However, the latter orientation might be a consequence of extensive fracturing and brecciation, which locally can be seen to deviate the foliation clearly.

The presence of amphibole and chlorite, both mainly derived from pyroxene, demonstrates a retrograde metamorphism and re-equilibration in the low amphibolite to greenschist facies (see "Igneous and Metamorphic Petrology and Geochemistry" section, this chapter). Textural evidence suggests that the high-temperature deformation occurred prior to the amphibole development.

Low-temperature Deformation

The low-temperature deformation clearly overprints the high-temperature deformation. It is expressed by three types of structural features:

1. Hairlike fractures that locally have bent or diverted the high-temperature foliation by a few degrees. These fractures appear to be filled with chlorite and epidote (e.g., Intervals 149-900A-82R-1, 100-112 cm, and -81R-1, 125-135 cm; Fig. 30).
2. Narrow shear zones are scattered along the whole basement section. Their expression varies from place to place. In Interval 149-900A-82R-1, 40-72 cm, a 15-cm-thick shear zone is localized in a microbreccia layer; the surrounding highly veined rock also has been affected, and the foliation has been locally diverted along its boundaries. Other narrower sheared microbreccia layers are present in Intervals 149-900A-82R-3, 75-80 cm; -82R-3, 112-113 cm; -82R-5, 39-42 cm; and-85R-3, 31-40 cm. In other places, narrow shear zones occur along crosscutting veins. The most common shearing occurs along veins filled mainly with chlorite and epidote (Intervals 149-900A-82R-1, 40-72 cm; -84R-4, 5-10 cm; and -86R-1, 0-15 cm, and Sample 149-900A-82R-1, 112 cm). A more diffuse shear zone was

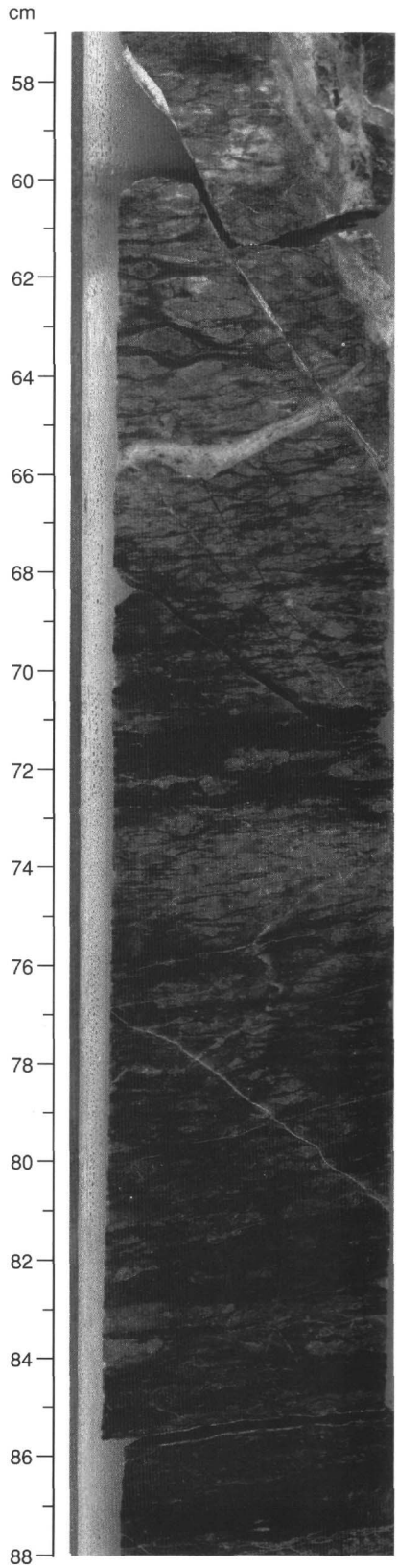

Figure 29. Foliated microgabbro in Interval 149-900A-83R-2, 57-88 cm, where the grain-size distribution is heterogeneous.

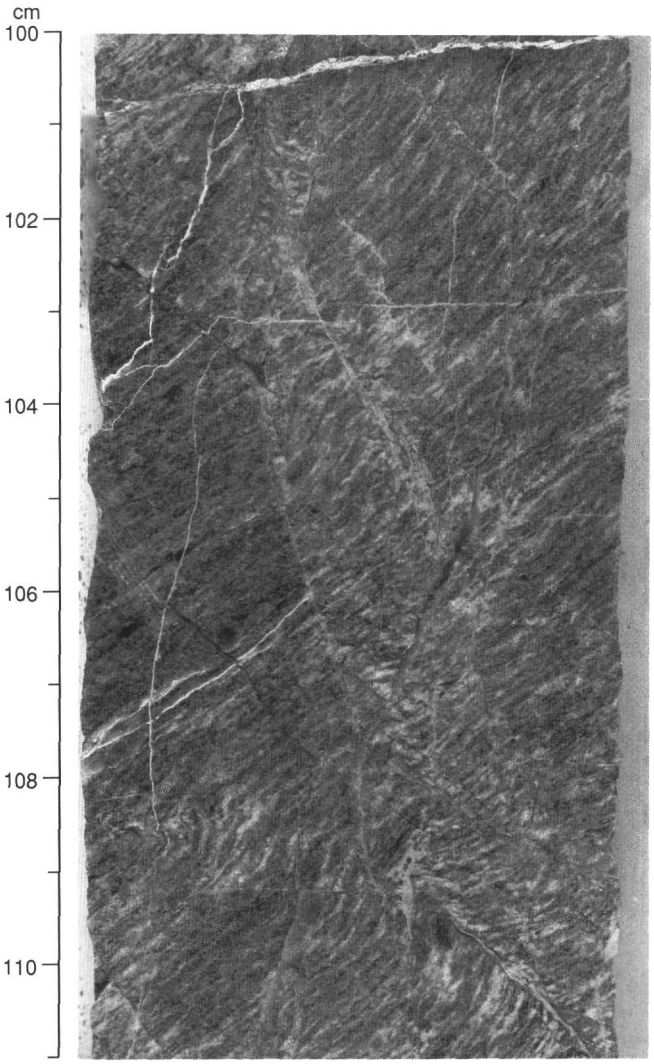

Figure 30. Hairlike fractures that have slightly diverted or bent the high-temperature foliation in Interval 149-900 A-82R-1, 100-111 cm.

recognized as anastomosing, thin, white veins that form a 5-cm-thick dipping band, where the foliation is slightly offset by the veins (Interval 149-900A-81R-1, 126-132 cm), or as numerous discrete, milky white, curved or straight veins, along which fragments of rock are isolated and rotated (Interval 149-900A-84R-1, 100-122 cm). These shear zones usually exhibit low dips and are subparallel or slightly oblique to the high-temperature foliation. In some cases, textural evidence suggests that these were displaced in a normal sense.

3. Fracturing is extensively but unevenly developed in the rocks. It led to a variety of veins and evolved locally into brecciation. The four main types of vein are described in the "Igneous and Metamorphic Petrology and Geochemistry" section (this chapter). Figure 31 illustrates the relationships between the different types of vein. The oldest brittle features are fine fractures having black marginal zones, which have been locally offset in a normal sense along epidote veins. Zoisite or clinozoisite veining then occurred, followed by gray calcite veining, which is the latest brittle event. The dip of the different fractures is generally 40° to 45°, or about 60°. The calcite veins often replace, or are parallel to, previous veins or tend to be subvertical. In Section 149-900A-82R-2, some large fractures filled in by epidote show two 45°-dipping conjugate sets and have an internal fabric that suggests a normal component of movement.

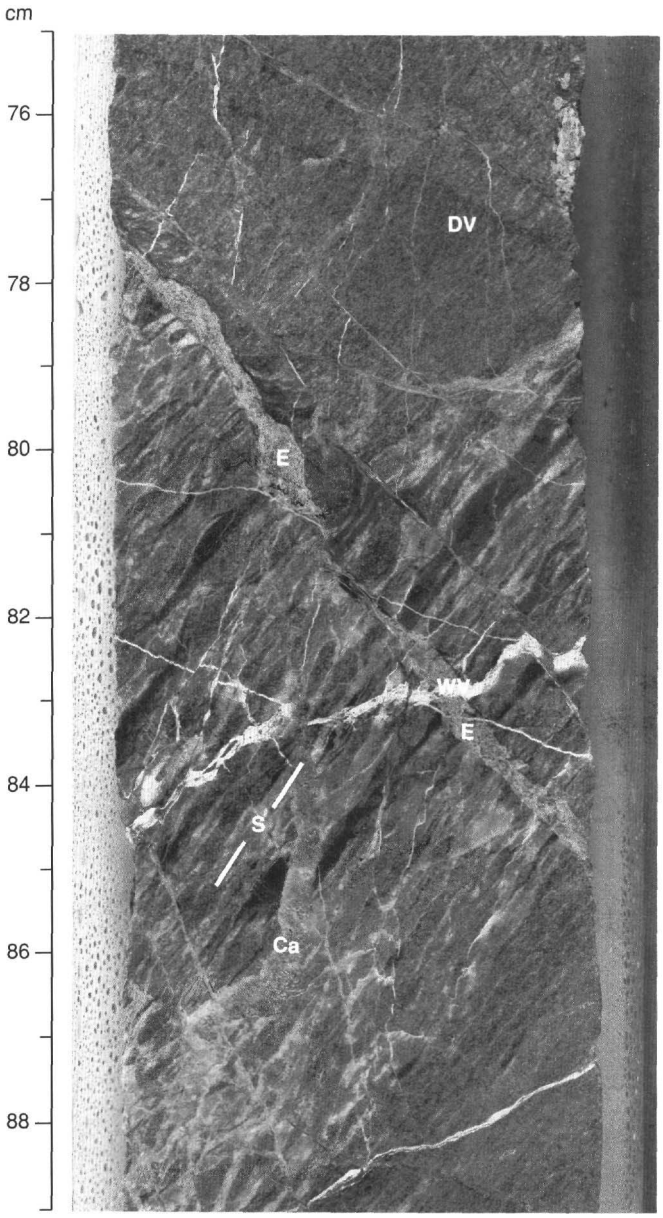

Figure 31. Vein relationships in Interval 149-900A-82R-1, 74-89 cm. DV = dark veins; E = epidote veins; WV = white veins; Ca = calcite veins; S = trace of the ductile foliation. See text for details.

Brecciation of the rocks develops in zones where a high degree of fracturing and veining has occurred. About 35% of the recovered basement rocks are brecciated; in particular, in Cores 149-900A-80R, -81R, and -84R. Two main types of breccia can be distinguished. The first type of breccia results from an intense fracturing by thin, contorted, and anastomosing veins of pale green material, in dipping zones a few centimeters thick (Interval 149-900A-81R-2, 15-20 cm; Fig. 32). With increasing vein density, the green color of the breccia suggests a pervasive fracturing and alteration possibly aided by fluid circulation (Fig. 33; Intervals 149-900A-81R-3, 0-15 cm, and -84R-2, 60-85 cm). This brecciation post-dates the zoisite veining, but pre-dates the calcite veins. The second type of breccia is made of angular blocks of fine-grained metamorphic mafic rocks embedded in a bright green chlorite and/or calcite matrix (e.g., Intervals 149-900A-83R-3, 0-50 cm; and -84R-1, 0-135 cm). In some places, the

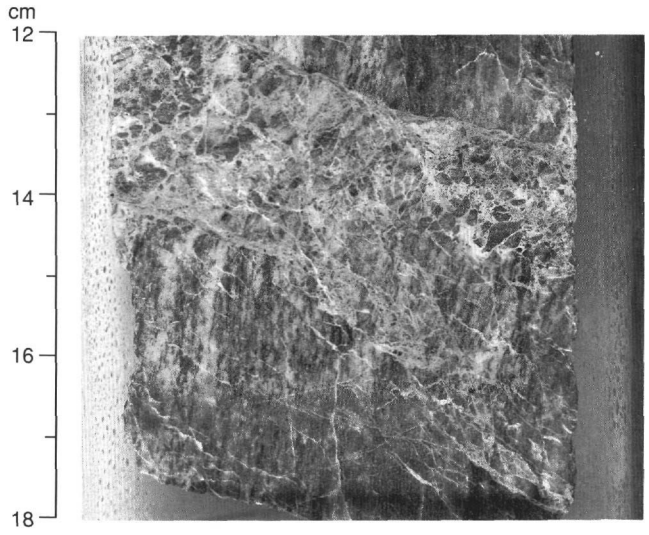

Figure 32. Intense fracturing expressed as thin, anastomosing pale green veins in Interval 149-900A-81R-2, 12-18 cm.

calcite appears to have replaced the chlorite after the formation of the breccia. In areas where the blocks are of reduced size, the texture of these breccias is mostly comparable to those of the Upper Breccia Unit described at Site 899 (e.g., Intervals 149-900A-80R-1, 47-70 cm, and -82R-5, 75-87 cm; see "Lithostratigraphy and Petrology" section, "Site 899" chapter, this volume). These breccias occur locally in 10-cm-thick bands that dip about 60° and may represent fault zones (Interval 149-900A-83R-2, 35-62 cm; Fig. 34). Finally, the proportion of epidote can be so high locally that angular clasts can be embedded in a primarily epidote matrix (Interval 149-900A-86R-1, 0-15 cm).

Discussion

The first tectonic event recognized in the rocks is an intense ductile deformation that developed a well-marked foliation. Textural evidence suggests that this deformation occurred at high temperature under dry conditions, likely during a shear event. Some intriguing thin fractures appear to have diverted or even bent the foliation. Such brittle features associated with "soft" deformation features might indicate either that (1) the conditions of deformation were close to the brittle/ductile transition during the formation of these fractures or (2) the foliation is progressively diverted or bent by closely spaced microfractures.

As the amphibole derived from primary pyroxene does not appear to be synkinematic, the retrograde metamorphism in low-amphibolite to greenschist facies seems to post-date the high-temperature ductile deformation event.

Next, a complicated structural evolution at low temperature affected the basement rocks. The most striking features associated with this late deformation are the successive types of vein and narrow shear zones unevenly distributed throughout the section. Most of the fractures, and particularly sets of conjugate 45°-dipping veins and brecciated zones having a 60°-dip, are in accordance with a horizontal extensional regime. The presence of shear zones in microbreccias and epidote-chlorite veins demonstrates that a shear event occurred during or after the formation of these veins and microbreccias. The calcite veining and fracturing clearly is the latest event to have occurred. The brecciation thus took place during or after the epidote veining and ended during the calcite veining.

Further petrostructural, geochemical, and geochronological studies may help to define the origin of these rocks, the sequence of the different tectonic and metamorphic events, and the kinematics of the deformations, and thus to constrain the evolution and emplacement

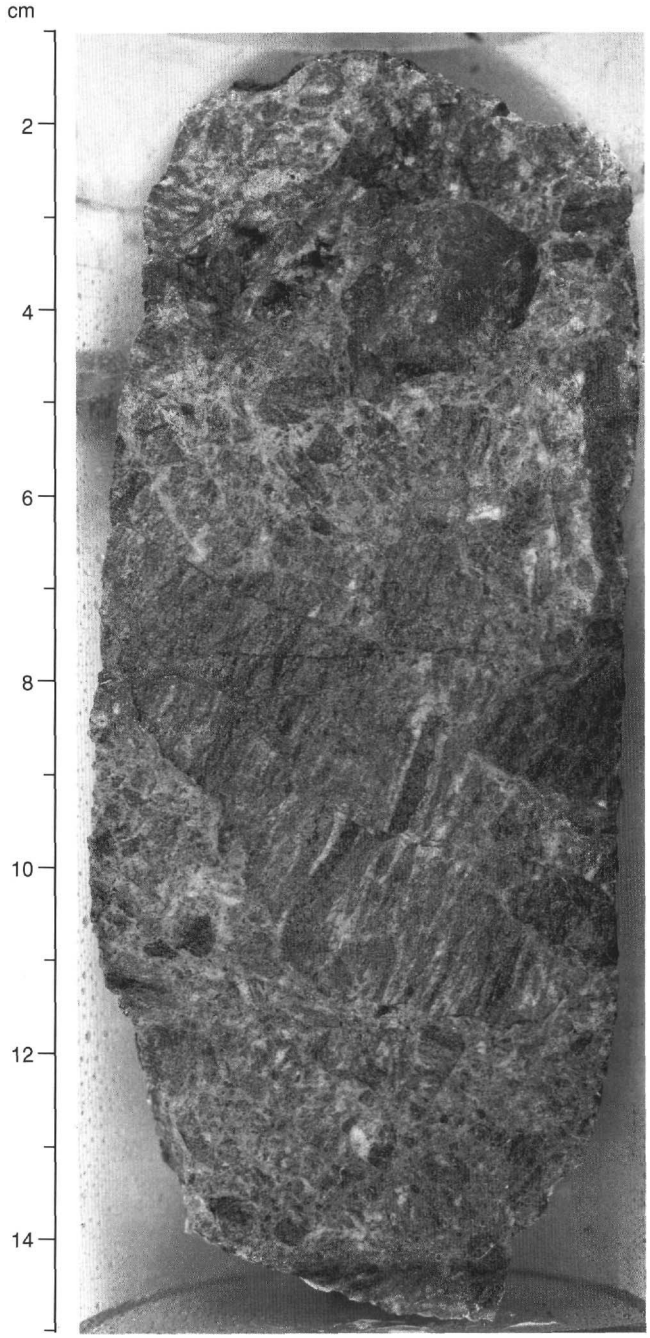

Figure 33. Brecciation of rock that results from the fracturing illustrated in Fig. 32 (Interval 149-900A-81R-3, 1-15 cm).

mechanism of this mafic body. Although the magnetization of these rocks is very low, possible reorientation of the structures in the geographic reference frame may be obtained from shore-based paleomagnetic data.

Site 900 is located between mantle rock outcrops (Site 897) and rocks having mantle affinities (Site 899) to the west and the continental crust of the passive margin farther to the east. The most likely hypotheses for the origin of these metamorphic basic rocks might be either to associate them with the Mesozoic rifting of the margin (underplated gabbros or atypical oceanic crust), or to consider them as older Hercynian units that have been incorporated in the passive margin. A preliminary comparison with the mantle rocks recovered at

Sites 897 and 899 suggests that the tectonometamorphic evolution of the ultramafic and mafic rocks may be comparable at the three sites (high-temperature ductile deformation in the peridotite and the mafic rocks, low-grade retro-metamorphism, late shear deformation and fracturing, similarities in the texture of some breccias, traces of fluid circulation; see "Structural Geology" sections, "Site 898" and "Site 899" chapters, this volume). As regards the synrift emplacement hypothesis, the Site 900 results show that the spatial transition between continental and oceanic crusts may occupy a large area made of transitional crust and serpentinized mantle. However, at present any conclusion would be premature. Further petrostructural studies and geochronological studies of the freshest basement samples will help to understand the presence of such rocks beneath the Iberia Abyssal Plain.

ORGANIC GEOCHEMISTRY

Concentrations of calcium carbonate were measured, on average, from three samples selected from each core in Hole 900A. Concentrations of organic carbon, C/N ratios, and Rock-Eval pyrolysis were employed to determine the type of organic matter contained within the upper sediment units. Routine monitoring of headspace gas contents, done for drilling safety, yielded information that is interesting to compare with Sites 897, 898, and 899.

Concentrations of Inorganic and Organic Carbon

Concentrations of carbonate carbon vary between 9.5% and essentially 0% in sediments from Site 900 (Table 9). These concentrations of carbonate carbon are equivalent to 78% to 0% $CaCO_3$ in the sediments, assuming that all of the carbonate is present as pure calcite. The variability in carbonate content reflects a history of generally low biological productivity and deposition of hemipelagic sediments below the CCD, combined with delivery of carbonate-rich turbiditic sediments initially deposited in shallower waters.

Concentrations of organic carbon were measured in a subset of sediment samples from the upper part of Hole 900A. The absence of significant amounts of headspace methane in Site 900 sediments suggested that organic carbon concentrations would be low, and therefore few organic carbon measurements were performed. Indeed, concentrations were low in nearly all of the Site 900 samples (Table 10). Unit I, a sequence dominated by Pleistocene to lower Pliocene turbidites, averages 0.3% organic carbon. This average is approximately the same as the average of 0.2% calculated from DSDP Legs 1 through 31 by McIver (1975). The equivalent lithological unit at Sites 897 and 898 contained 0.5% to 0.6% organic carbon (see "Site 897" and "Site 898" chapters, this volume). The two principal sources of organic matter in oceanic sediments are marine algal production and land plant detritus supplied by rivers and winds. Algal organic matter is typically oxidized and largely recycled during and shortly after settling to the seafloor (e.g., Suess, 1980; Emerson and Hedges, 1988). The land-derived organic matter that is delivered to deep-sea sediments is generally the less-reactive material that survives transport to the ocean. The organic carbon found in Unit I at Site 900 evidently has been substantially oxidized prior to sedimentation and, consequently, is not very reactive.

Characterization of Sources of Organic Matter

Organic C/N ratios were measured for selected Site 900 samples to determine the source of the organic matter. Algal organic matter generally has C/N ratios of between 5 and 10, whereas organic matter derived from land plants has values between 20 and 100 (e.g., Emerson and Hedges, 1988; Meyers, in press). Variable C/N ratios of samples

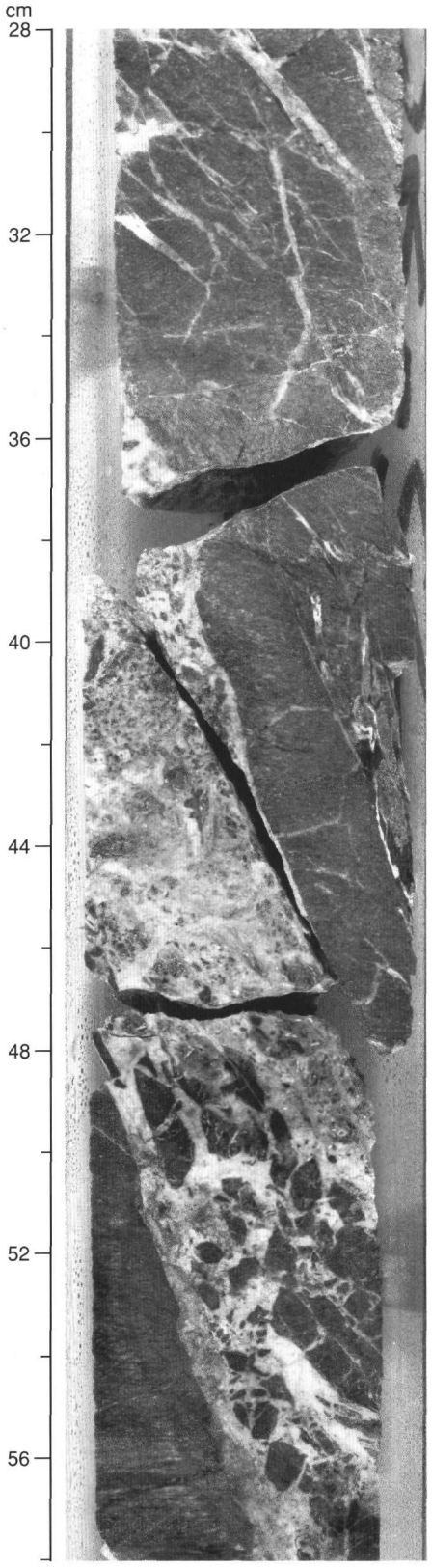

Figure 34. Band of brecciation having a 55°-dip, which may represent a normal fault zone (Interval 149-900A-83R-2, 22-58 cm).

Table 9. Concentrations of inorganic carbon in sediments and rocks from Hole 900A.

Core, section, interval (cm)	Depth (mbsf)	Inorg. C (%)	$CaCO_3$ (%)	Lithologic unit
149-900A-				
4R-1,47–48	21.30	8.07	67	Subunit IA: nannofossil clay and ooze with clay
4R-1, 54–57	21.30	3.39	28	
4R-1, 66–67	21.50	0.28	2	
4R-1, 129–130	22.10	8.15	68	
4R-2, 68–69	23.00	3.35	28	
6R-1, 29–30	40.30	6.76	56	
6R-4, 60–61	45.10	0.37	3	
6R-4, 83–84	45.30	6.62	55	
6R-5, 67–68	46.70	3.46	29	
6R-5, 119–120	47.20	1.78	15	
7R-3, 119–120	53.80	8.12	68	
8R-3, 42–43	62.70	7.11	59	
9R-1, 11–12	64.60	0.90	8	
9R-2, 25–26	66.30	8.04	67	
10R-1, 34–35	74.40	8.61	72	Subunit IB: nannofossil chalk and claystone
10R-2, 94–95	76.50	7.58	63	
10R-4, 25–27	78.90	8.46	71	
10R-4, 52–53	79.10	4.42	37	
10R-5, 3–4	80.10	4.68	39	
11R-1, 74–75	84.40	7.91	66	
11R-3, 90–91	87.60	4.55	38	
11R-4, 96–97	89.20	8.47	71	
12R-1, 49–50	93.90	6.42	54	
12R-2, 48–49	95.40	2.36	20	
12R-2, 107–108	96.00	3.21	27	
14R-1, 49–50	113.00	0.20	2	Subunit IC: nannofossil claystone and chalk with claystone
14R-5, 143–145	120.00	5.40	45	
15R-2, 72–73	125.00	7.97	66	
15R-3, 74–75	126.00	4.43	37	
15R-3, 108–109	127.00	8.12	68	
16R-2, 73–74	134.00	5.63	47	
16R-3, 61–62	136.00	4.09	34	
16R-5, 75–76	139.00	8.77	73	
17R-2, 15–16	143.00	3.43	29	
17R-2, 75–76	144.00	1.51	13	
17R-2, 90–91	144.00	6.56	55	
18R-1, 49–50	152.00	3.36	28	
18R-1, 84–85	152.00	6.90	58	
18R-2, 50–51	153.00	8.59	72	
18R-3, 89–90	155.00	9.57	80	
18R-4, 34–35	156.00	5.73	48	
20R-1, 18–19	171.00	5.9	49	
20R-1, 25–26	171.00	5.94	50	
20R-4, 58–59	176.00	4.88	41	
20R-7, 19–20	180.00	3.33	28	
21R-1, 58–59	181.00	0.34	3	
21R-2, 121–122	183.00	8.20	68	Subunit IIA: nannofossil claystone, claystone, and silty claystone
21R-3, 104–105	184.00	4.32	36	
21R-6, 84–85	189.00	3.93	33	
22R-1, 86–87	191.00	8.13	68	
22R-1, 101–102	191.00	4.56	38	
22R-2, 120–121	193.00	5.56	46	
22R-3, 11–12	193.00	0.19	2	
22R-5, 20–21	196.00	9.11	76	
23R-2, 101–102	202.00	3.93	33	
23R-3, 72–73	203.00	0.49	4	
23R-6, 83–85	208.00	9.46	79	
24R-3, 29–30	213.00	9.33	78	
24R-4, 59–60	214.00	2.72	23	
24R-6, 19–20	217.00	2.64	22	
25R-1, 70–71	220.00	0.90	8	
25R-3, 130–131	223.00	4.53	38	
25R-4, 22–23	224.00	5.79	48	
26R-1, 44–45	229.00	5.72	48	
26R-2, 34–35	230.00	1.47	12	
26R-2, 119–120	231.00	2.82	24	
26R-5, 37–38	234.00	3.70	31	Subunit IIB: nannofossil claystone and claystone
27R-4, 44–45	243.00	1.20	10	
27R-5, 2–3	244.00	4.64	39	
28R-1, 119–120	249.00	7.16	60	
28R-2, 55–56	250.00	3.20	27	
28R-4, 2–3	252.00	4.21	35	
29R-5, 29–30	263.00	4.86	41	
30R-2, 40–41	269.00	4.28	36	
30R-4, 83–84	272.00	6.48	54	
30R-6, 38–39	275.00	3.38	28	
30R-6, 82–83	275.00	1.70	14	
31R-1, 117–118	278.00	3.59	30	
31R-3, 40–41	280.00	3.67	31	
31R-5, 31–32	283.00	0.76	6	
32R-1, 59–60	287.00	3.64	30	
33R-6, 32–33	304.00	1.49	12	
34R-2, 82–83	308.00	4.35	36	
34R-2, 120–121	308.00	3.35	28	
34R-3, 122–123	310.00	4.34	36	
34R-4, 46–47	311.00	1.00	8	
35R-2, 71–72	318.00	5.61	47	
35R-3, 51–52	319.00	3.80	32	
35R-3, 112–113	319.00	0.71	6	
36R-2, 38–39	327.00	0.75	6	
36R-3, 90–91	329.00	5.62	47	
36R-6, 73–74	333.00	2.36	20	
37R-1, 48–49	335.00	8.28	69	
37R-1, 99–100	336.00	8.31	69	
37R-3, 107–108	339.00	2.09	17	
37R-4, 51–52	340.00	0.71	6	
38R-2, 17–18	346.00	3.29	27	
38R-2, 37–38	346.00	2.34	20	
38R-2, 133–134	347.00	3.16	26	
38R-3, 25–26	348.00	7.13	59	
39R-1, 40–41	354.00	2.67	22	
39R-2, 65–66	356.00	1.86	16	
39R-3, 31–32	357.00	1.99	17	
40R-2, 49–50	366.00	0.56	5	
40R-4, 71–72	369.00	3.64	30	
41R-2, 34–35	375.00	3.10	26	
41R-2, 38–39	375.00	0.51	4	
42R-1, 87–88	384.00	0.22	2	
42R-1, 97–98	384.00	2.34	20	
42R-3, 126–127	387.00	8.58	72	
42R-4, 90–91	388.00	2.52	21	
43R-1, 122–123	394.00	3.32	28	
43R-2, 59–60	395.00	1.66	14	
43R-3, 131–132	397.00	3.39	28	
43R-5, 48–49	399.00	4.95	41	
44R-1, 91–92	403.00	1.82	15	
44R-5, 73–74	409.00	3.65	30	
44R-5, 79–80	409.00	0.83	7	
44R-5, 87–88	409.00	6.28	52	
46R-1, 131–132	423.00	0.73	6	
46R-2, 8–9	423.00	2.93	24	
46R-3, 44–45	425.00	0.08	1	
46R-6, 28–29	429.00	5.78	48	
47R-3, 70–71	435.00	2.91	24	
47R-6, 68–69	439.00	5.09	42	
49R-1, 101–102	451.00	0.51	4	
49R-2, 98–99	453.00	0.53	4	
50R-1, 10–11	460.00	0.24	2	
50R-2, 64–65	462.00	0.28	2	
50R-3, 16–17	463.00	4.97	41	
51R-2, 98–99	472.00	0.14	1	
51R-4, 97–98	475.00	0.13	1	
52R-2, 79–80	482.00	0.33	3	
52R-5, 49–50	486.00	3.56	30	
52R-5, 75–76	486.00	1.49	12	
52R-5, 76–77	486.00	2.81	23	
52R-5, 80–81	486.00	5.09	42	
53R-1, 98–99	490.00	0.49	4	
53R-1, 114–115	490.00	7.46	62	
53R-3, 60–61	492.00	0.27	2	
53R-4, 96–97	494.00	1.95	16	
54R-1, 31–32	499.00	0.29	2	
54R-1, 36–37	499.00	1.97	16	
54R-3, 118–119	503.00	3.51	29	
56R-1, 36–37	518.00	2.67	22	
56R-4, 130–131	523.00	2.24	19	
56R-5, 63–64	524.00	1.07	9	
56R-5, 134–135	525.00	0.89	7	
57R-1, 57–58	528.00	0.26	2	
57R-1, 67–68	528.00	2.33	19	
57R-1, 126–127	529.00	0.78	7	
57R-2, 20–21	529.00	4.92	41	
57R-3, 25–26	531.00	2.90	24	
58R-2, 65–66	539.00	0.15	1	
58R-3, 65–66	541.00	2.95	25	
58R-3, 89–90	541.00	2.41	20	
59R-2, 52–53	549.00	4.43	37	
59R-5, 57–58	554.00	3.37	28	
59R-6, 130–131	556.00	3.68	31	
60R-2, 44–45	559.00	2.99	25	
60R-3, 100–101	561.00	2.84	24	
60R-4, 49–50	562.00	1.19	10	
60R-4, 117–118	562.00	2.80	23	
61R-2, 5–6	568.00	2.91	24	
61R-3, 91–92	570.00.	1.42	12	
64R-1, 41–42	596.00	0.27	2	
65R-1, 15–16	605.00	0.17	1	
65R-1, 78–79	605.00	1.29	11	
66R-1, 18–19	614.00	0.19	2	
67R-1, 31–32	624.00	2.53	21	
67R-1, 132–133	625.00	0.21	2	
68R-2, 52–53	635.00	0.22	2	
69R-1, 60–61	644.00	1.10	9	
69R-2, 60–61	645.00	5.40	45	
70R-1, 59–60	653.00	4.85	40	

Table 9 (continued).

Core, section, interval (cm)	Depth (mbsf)	Inorg. C (%)	$CaCO_3$ (%)	Lithologic unit
70R-2, 59–60	655.00	0.32	3	
70R-2, 76–77	655.00	5.29	44	
75R-1, 76–77	702.00	5.92	49	
76R-1, 16–17	711.00	0.23	2	
76R-1, 54–55	711.00	0.25	2	
76R-2, 44–45	712.00	0.09	1	
77R-1, 37–39	720.00	0.23	2	

Table 10. Concentrations of organic carbon and C/N ratios of selected samples from Site 900.

Core, section, interval (cm)	Depth (mbsf)	Tot. C (%)	Inorg. C (%)	Org. C (%)	Org. C/N	Org. C/S
149-900A-						
4R-1, 54–57	21.3	3.39	3.39	0.00	0.0	0.0
4R-1, 66–67	21.5	0.40	0.28	0.12	2.0	1.2
4R-1, 129–130	22.1	8.50	8.15	0.35	11.0	
4R-2, 68–69	23.0	3.88	3.35	0.53	10.0	6.6
6R-4, 60–61	45.1	0.85	0.37	0.48	12.0	3.2
6R-4, 83–84	45.3	6.89	6.62	0.27	9.0	
6R-5, 67–68	46.7	3.94	3.46	0.48	9.6	48.0
6R-5, 119–120	47.2	1.80	1.78	0.02	1.0	0.1
8R-3, 42–43	62.7	7.33	7.11	0.22	7.3	
9R-1, 11–12	64.6	1.43	0.90	0.53	13.0	
10R-4, 25–27	78.9	8.56	8.46	0.10	5.0	
10R-4, 52–53	79.1	4.46	4.42	0.04	1.0	0.6
14R-1, 49–50	113.0	0.20	0.20	0.00	0.0	
15R-3, 74–75	126.0	4.69	4.43	0.26	8.6	
16R-2, 73–74	134.0	5.72	5.63	0.08	2.0	
16R-3, 61–62	136.0	4.56	4.09	0.47	7.8	12.0

Note: Concentrations of organic carbon were estimated from the difference between total carbon and inorganic carbon values. C/N weight ratios were calculated from concentrations of organic carbon and total nitrogen, respectively.

Table 11. Results of headspace gas analyses from Hole 900A.

Core, section, interval (cm)	Depth (mbsf)	C_1 (ppm)	Core, section, interval (cm)	Depth (mbsf)	C_1 (ppm)
149-900A-			40R-4, 0–5	368.00	4
1R-2, 0–5	0.81	2	41R-4, 0–5	376.89	4
2R-1, 37–42	1.87	2	42R-4, 0–5	387.40	4
3R-2, 0–5	12.60	2	43R-4, 0–5	397.10	4
4R-4, 0–5	25.30	2	44R-5, 0–5	407.82	4
5R-4, 0–5	34.90	2	45R-4, 0–5	416.50	4
6R-5, 0–5	46.00	2	46R-5, 0–5	427.60	4
7R-4, 0–5	54.10	6	47R-4, 0–5	435.60	4
8R-2, 0–5	60.80	5	48R-6, 0–5	448.10	4
9R-2, 0–5	66.00	6	49R-6, 0–5	457.70	4
10R-2, 0–5	75.60	6	50R-5, 0–5	465.76	4
11R-4, 0–5	88.20	6	51R-5, 0–5	475.90	4
12R-3, 0–5	96.40	5	52R-4, 0–5	483.70	4
14R-3, 0–5	115.70	5	53R-3, 0–5	491.61	4
15R-3, 0–5	125.40	5	54R-2, 0–5	500.10	4
16R-4, 0–5	136.50	5	56R-2, 0–5	519.50	4
17R-2, 0–5	143.10	5	57R-3, 0–5	530.60	4
18R-3, 0–5	154.30	5	58R-2, 0–5	538.70	4
19R-2, 0–5	162.40	5	59R-6, 0–5	554.40	4
20R-6, 0–5	178.10	4	60R-4, 0–5	561.10	5
21R-5, 0–5	186.30	4	61R-3, 0–5	569.20	4
22R-5, 0–5	195.90	4	62R-3, 0–5	578.03	4
23R-6, 0–5	207.00	4	63R-2, 0–5	587.10	4
24R-5, 0–5	215.20	4	64R-2, 0–5	596.60	4
25R-5, 0–5	224.80	4	65R-3, 0–5	606.86	4
26R-4, 0–5	232.45	4	66R-2, 0–5	615.60	4
27R-4, 0–5	242.60	4	67R-2, 0–5	625.30	4
28R-4, 0–5	252.30	4	68R-3, 0–5	636.40	5
29R-4, 0–5	261.09	4	69R-2, 0–5	644.60	4
30R-4, 0–5	271.60	4	70R-2, 0–5	654.20	4
31R-4, 0–5	281.20	4	71R-4, 0–5	665.95	5
32R-4, 0–5	290.00	4	72R-1, 145–150	673.55	4
33R-4, 0–5	300.50	4	73R-1, 145–150	683.15	4
34R-3, 0-5	308.60	4	74R-1, 145–150	692.85	4
35R–4, 0-5	319.80	4	75R-1, 104–109	702.14	4
36R–5, 0-5	330.90	4	76R-2, 0–5	711.90	4
37R-5, 0–5	340.50	4	77R-3, 0–5	723.00	4
38R-5, 0–5	350.20	4	78R-1, 145–150	731.15	4
39R-5, 0–5	359.80	4			

Note: Concentrations of methane (C_1) are given in parts per million and are at the limit of detection. Heavier gases were not measurable in Site 900 headspace samples.

from Unit I (Table 10) indicate that some samples have a predominantly marine source for their organic matter, whereas other samples contain mostly terrigenous organic matter. The C/N ratios of some samples are low (<5). These values are probably an artifact of the low carbon contents, combined with the tendency of clay minerals to absorb ammonium ions generated during the degradation of organic matter (Müller, 1977). The C/N ratios in samples that are especially low in organic carbon consequently are not accurate indicators of the source of organic matter.

Headspace Gases

Concentrations of headspace methane were monotonously low throughout Site 900 (Table 11). These low concentrations contrast with the high levels of biogenic methane found in the upper, turbiditic units at Sites 897 and 898, but are similar to the low amounts present at Site 899 (see "Site 897," "Site 898," and "Site 899" chapters, this volume). The generally low amounts, and inferred inert character, of organic matter in sediments from Site 900 evidently preclude methanogenesis. In addition, Claypool and Kvenvolden (1983) observed that the presence of interstitial sulfate inhibits methanogenesis in marine sediments, and concentrations of sulfate are high throughout the recovered Site 900 sediments (see "Inorganic Geochemistry" section, this chapter).

Comparisons of Organic Matter Type from Rock-Eval Pyrolysis

Rock-Eval pyrolysis of organic matter from selected Unit I samples from Sites 897, 898, 899, and 900 provided insights into the differences in concentrations of headspace gas at these locations. Two Rock-Eval parameters are especially useful for characterizing sedimentary organic matter. The hydrogen index (HI) is the quantity of hydrocarbons generated from thermal decomposition of the organic matter, expressed as milligrams of hydrocarbons per gram of total organic carbon. Marine organic matter typically has high HI values (Espitalié et al., 1977). The oxygen index (OI) is the quantity of CO_2 generated during pyrolysis and is given in the same units. Cellulose-containing land plants produce organic matter having high OI and low HI values (Espitalié et al., 1977). Organic matter in Unit I samples from all four sites has high OI and low HI values (Table 12), which would normally indicate a land-derived origin. Relatively low C/N ratios, however, contradict this interpretation. It is likely that the organic matter in this turbiditic sedimentary unit has experienced considerable post-depositional oxidation, which would depress HI values while enhancing OI values. This evidence of alteration in the Rock-Eval source character implies that considerable microbial degradation of the marine organic matter in Unit I has occurred, which is consistent with an inferred history of downslope relocation of the Unit I sediments from a shallower site of initial accumulation. Sediments from Sites 899 and 900 have lower S_1, S_2, and HI values than those from Sites 897 and 898 and have been degraded to greater degrees. This difference in organic matter character in closely spaced locations on the Iberia Abyssal Plain implies different deliveries of turbidite components at the sites. Furthermore, the greater amount of degradation evident at Sites 899 and 900 appears to render the organic matter less supportive of methanogenic bacteria. The generally low T_{max} values (Table 10) suggest that thermal degradation of the organic matter can be excluded; the large range of T_{max} (309°-441°C) probably reflects heterogeneous mixtures of relatively fresh marine and detrital organic matter in the turbidites.

Table 12. Results of Rock-Eval pyrolysis of sediments selected from the turbidite-containing Unit I of Sites 897 through 900.

Core, section, interval (cm)	TOC	C/N	S_1	S_2	S_3	T_{max}	HI	OI
149-897C-								
4R-1, 45–46	1.37	11.4	0.41	1.63	2.63	413	118	191
6R-1, 53–54	0.64	8.1	0.26	0.41	2.20	391	64	343
8R-1, 49–50	1.52	11.1	0.44	1.77	2.58	409	116	170
10R-1, 56–57	0.79	9.7	0.25	0.45	1.76	400	56	222
12R-6, 34–35	0.63	8.2	0.15	0.36	1.43	397	57	226
14R-4, 64–65	1.21	11.8	0.30	1.07	2.05	408	88	169
16R-1, 75–76	1.20	11.7	0.29	1.51	2.03	414	125	169
19R-1, 10–11	0.77	9.7	0.16	0.62	1.70	408	77	212
21R-1, 124–125	2.74	13.9	0.24	0.94	2.27	414	34	82
23R-1, 69–70	1.81	3.3	0.53	2.54	2.43	416	140	134
25R-1, 122–123	0.56	16.3	0.11	0.27	1.17	394	40	200
149-898A-								
1H-5, 43–44	0.45	22.0	0.11	0.10	1.91	335	22	424
3H-4, 9–10	0.37	9.2	0.05	0.00	1.42		0	383
5H-5, 86–87	0.31	6.2	0.08	0.09	1.16	309	29	374
6H-6, 63–64	0.52	7.4	0.20	0.47	2.16	393	90	415
10H-3, 85–86	0.42	6.0	0.11	0.09	2.18	369	21	519
14H-5, 74–75	0.30	2.5	0.11	0.03	2.04	375	10	680
16X-1, 32–33	0.32	2.9	0.08	0.14	1.72	426	43	537
149-898B-								
1H-1, 22–23	0.27	9.0	0.22	0.36	1.96	441	133	729
149-899A-								
1R-1, 48–49	1.07	13.4	0.26	0.84	2.66	431	78	249
2R-1, 48–49	0.24	4.8	0.04	0.03	2.26	437	12	942
2R-1, 69–70	0.30	5.0	0.09	0.07	2.06	317	23	687
4R-1, 118–119	0.58	19.0	0.04	0.05	1.07		8	184
4R-2, 48–49	0.24	4.8	0.07	0.09	1.48		37	617
6R-4, 25–26	1.36	34.0	0.04	0.03	1.93		2	142
149-900A-								
4R-1, 129–130	0.35	11.0	0.06	0.04	2.25		11	643
4R-2, 68–69	0.53	10.0	0.06	0.05	2.25	309	9	424
6R-4, 60–61	0.48	12.0	0.06	0.07	0.64		14	133
6R-5, 67–68	0.48	9.6	0.15	0.09	1.99	340	18	414
9R-1, 11–12	0.53	13.0	0.06	0.03	1.30		5	245

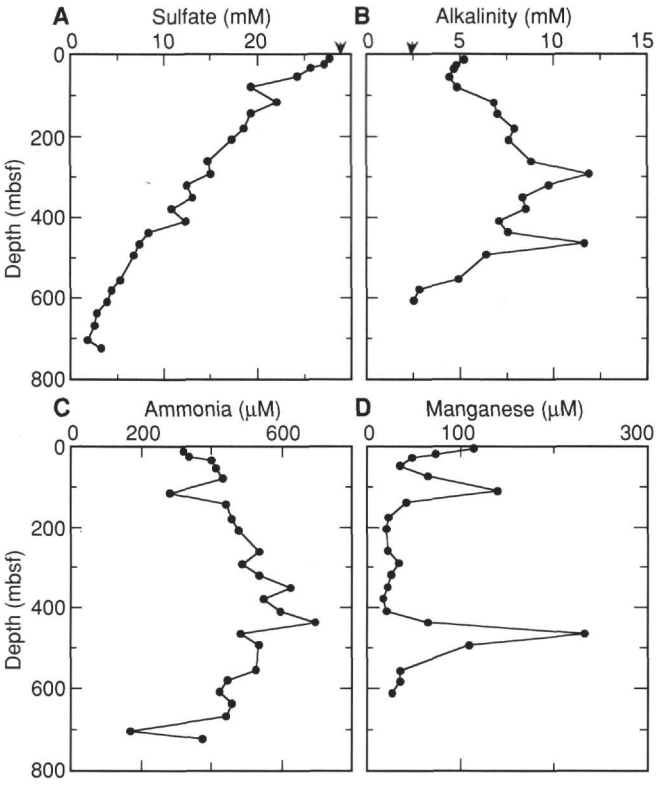

Figure 35. Interstitial-water profiles for Site 900. Arrows indicate typical bottom-water values. **A**. Sulfate. **B**. Alkalinity. **C**. Ammonia. **D**. Manganese.

INORGANIC GEOCHEMISTRY

Twenty-seven interstitial-water samples were collected at Site 900 between 12.6 and 721.5 mbsf. Whole-round samples were collected from each core in the interval from 12.6 to 34.9 mbsf (Cores 149-9OOA-3R to -5R) and from every third core thereafter (when recovery allowed). Interstitial-water samples spanned lithostratigraphic Units I and II. Results from shipboard interstitial-water analyses are presented in Table 13.

Concentrations of sulfate decreased from 27.9 mM in the first sample, at 12.6 mbsf, to a minimum of 1.9 mM at 702.2 mbsf (Fig. 35A). The sulfate profile is slightly convex upward, suggesting that some sulfate reduction occurred within the sediment sequence.

Values of alkalinity decrease slightly from 12.6 to 54.1 mbsf and then increase to a maximum of 11.9 mM at 289.9 mbsf (Fig. 35B). The increase in alkalinity results from anaerobic organic carbon degradation (Gieskes, 1974, 1983). Alkalinity decreases between 289.9 and 465.7 mbsf and then increases to a peak of 11.7 mM at 465.7 mbsf. Alkalinity decreases below 407.7 mbsf to a minimum of 2.5 mM at 606.8 mbsf. Sample size limitations prevented the analysis of alkalinity in the deeper samples.

Concentrations of ammonia generally increase with depth from a concentration of 321 μM at 12.6 mbsf to a maximum of 698 μM at 435.5 mbsf and decrease slightly thereafter (Fig. 35C). The maximum is consistent with a zone of active sulfate reduction within the interval between the surface and about 450 mbsf. Fluctuations in the profile indicate alternating zones of production and removal (the two anomalously low ammonia values at 116 and 702 mbsf probably reflect analytical problems).

The dissolved manganese profile shows three distinct zones of release and removal that produced maxima at 12.6, 115.7, and 465.7 mbsf (Fig. 35D). The high concentrations of manganese in the first sample probably result from the reduction of manganese oxides during the oxidation of organic carbon. The two deeper maxima may result from the reduction of manganese oxides and/or dissolution of some manganese carbonate phase.

Concentrations of calcium are slightly depleted with respect to typical concentrations of bottom water in the first four samples from 12.6 to 54.1 mbsf and then increase linearly to 31.5 mM at 289.9 mbsf (Fig. 36A). Below 289.9 mbsf, concentrations of calcium increase slightly to reach 36.0 mM by 636.3 mbsf and then increase rapidly to a maximum value of 46.5 mM by 721.5 mbsf. The profile suggests zones of calcium release at about 300 and below 636 mbsf. The release of calcium probably reflects regions of carbonate recrystalization (Gieskes, 1983).

Concentrations of magnesium generally decrease with depth from near typical bottom water to a minimum of 17.3 mM at 702.2 mbsf (Fig. 36B). The profile shows two zones where the gradient is steep, below 115.7 and below 606.8 mbsf. The steep negative gradient suggests that magnesium removal is greatest in these zones. The removal of magnesium probably results from clay mineral alteration (Gieskes, 1983).

Concentrations of strontium increase from a minimum of 125 μM in the first sample at 12.6 mbsf to a maximum of 846 μM at 465.7 mbsf and remain fairly constant below that depth (Fig. 36C). The strontium profile is slightly convex up between the surface and the maximum at 465.7 mbsf, indicating release of strontium from the solids through this sequence. Strontium release is probably associated with recrystalization of carbonate phases (Gieskes, 1974).

Concentrations of potassium generally decrease downhole, with some narrow zones of release and removal indicated by fluctuations in the profile (Fig. 36D). Potassium values decrease from a maximum of 10.3 mM in the first sample at 12.6 mbsf to a minimum of 0.7 mM at 702.2 mbsf. The profile is fairly linear, suggesting removal of potassium by means of interaction with basement rock.

Concentrations of silica remain near typical bottom-water values from 12.6 to 77.1 mbsf and then increase to a broad maximum, reaching 1188 μM between 143.0 and 435.5 mbsf (Fig. 37). Concen-

Table 13. Interstitial-water data for Site 900.

Core, section, interval (cm)	Depth (mbsf)	Alkalinity (mM)	Sulfate (mM)	Silica (µM)	Ammonia (µM)	Manganese (µM)	Strontium (µM)	Potassium (mM)	Chloride (mM)	Calcium (mM)	Magnesium (mM)	Sodium (mM)
149-900A-												
3R-1, 142–150	12.6	5.21	27.9	210	321	5.7	125	10.3	576	9.7	51.9	453
4R-3, 142–150	25.3	4.82	27.3	189	337	3.6	133	9.5	560	9.7	51.3	443
5R-3, 142–150	34.9	4.67	25.8	171	401	2.3	148	9.9	564	9.8	50.1	447
7R-3, 142–150	54.1	4.44	24.3	174	413	1.7	177	9.2	565	10.2	49.7	454
10R-2, 142–150	77.1	4.90	19.4	153	434	3.2	223	7.1	563	11.3	48.9	434
14R-2, 140–150	115.7	6.87	22.2	325	283	7.0	363	6.0	555	15.2	49.2	457
17R-1, 135–150	143.0	7.05	19.4	284	445	2.1	436	7.6	556	17.2	45.3	479
20R-5, 135–150	178.0	7.97	18.6	879	460	1.1	502	7.0	487	21.1	41.4	455
23R-5, 135–150	206.9	7.66	17.3	1052	478	1.0	575	7.0	556	23.6	40.3	446
26R-3, 87–105	232.4											
29R-3, 45–59	261.0	8.87	14.9	1098	536	1.0	600	6.1	569	27.8	35.8	451
32R-3, 44–60	289.9	11.94	15.1	1188	487	1.6	672	5.8	560	31.5	35.9	440
35R-3, 135–150	319.7	9.75	12.6	1111	538	1.2	678	5.0	557	32.4	33.7	432
38R-4, 135–150	350.1	8.35	13.1	1000	625	1.0	696	5.2	550	32.2	33.8	442
41R-3, 51–69	376.8	8.53	10.9	1103	549	0.8	663	4.7	541	33.2	32.1	397
44R-4, 86–102	407.7	7.08	12.4	1070	598	1.0	756	4.0	550	33.7	32.0	434
47R-3, 135–150	435.5	7.61	8.5	1067	698	3.2	786	4.8	552	33.2	32.2	443
50R-4, 116–136	465.7	11.70	7.5	879	484	11.7	846	3.1	552	37.9	32.7	419
53R-2, 102–121	491.5	6.46	6.9	647	538	5.4	792	3.3	546	34.7	30.9	422
56R-3, 56–75	521.7											
59R-5, 130–150	554.3	4.91	5.4	604	527	1.7	798	2.7	527	35.2	29.5	377
62R-2, 47–63	578.0	2.81	4.5	609	446	1.7	801	2.3	515	34.4	28.2	399
65R-2, 61–76	606.8	2.54	4.0	596	423	1.2	816	2.1	526	35.5	27.9	399
68R-2, 135–150	636.3		2.9	143	458		792	1.8	521	36.0	24.8	388
71R-3, 44–55	665.9		2.7	130	445		810	2.6	515	39.9	21.3	396
75R-1, 109–121	702.2		1.9	158	170		720	0.7		41.6	17.3	262
77R-1, 140–150	721.5		3.4	403	375		783	1.4	523	46.5	18.0	337

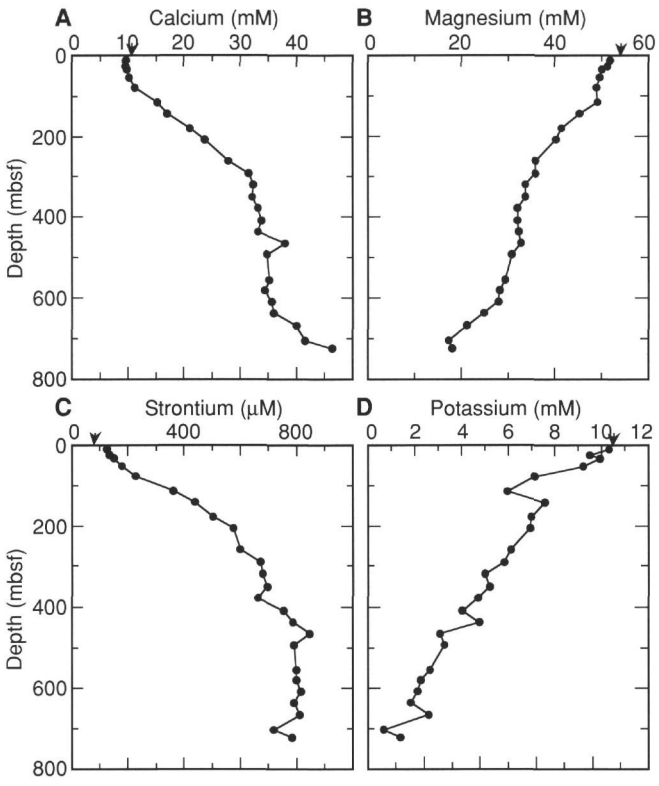

Figure 36. Interstitial-water profiles for Site 900. Arrows indicate typical bottom-water values. **A**. Calcium. **B**. Magnesium. **C**. Strontium. **D**. Potassium.

trations of silica decrease below 435.5 mbsf to a minimum of 130 µM at 665.9 mbsf.

Concentrations of chloride remain fairly constant with respect to typical bottom water through most of the sediment column, with the exception of the last six samples, which are lower (Table 13). In contrast to chloride, sodium is generally depleted with respect to typical bottom water throughout the sediment column (Table 13).

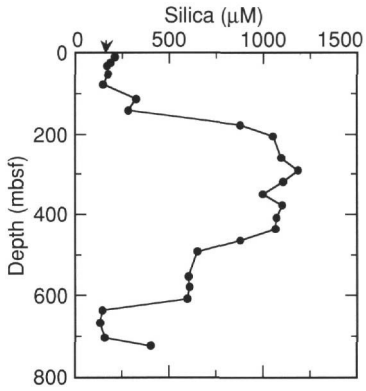

Figure 37. Interstitial-water profile for silica at Site 900. Arrow indicate; typical bottom-water value.

PHYSICAL PROPERTIES

Introduction

Whole-core measurements taken at Site 900 included magnetic susceptibility, Gamma-Ray Attenuation Porosity Evaluator (GRAPE) bulk density, P-wave logger (PWL) compressional-wave velocity, and thermal conductivity. Discrete velocity measurements were obtained in unlithified sediments using the Digital Sound Velocimeter (DSV) on split cores and within the more consolidated units and hard rock using the Hamilton Frame Velocimeter. Undrained shear strength was measured on split sediment cores, and electrical resistivity was measured on split sediment cores and drilled "minicores" from crystalline rock. Index properties were calculated from the wet and dry masses and wet and dry volumes of samples taken from each section of core.

Index Properties

Index properties were determined using gravimetric methods (Table 14; Fig. 38). Based on the nominal uncertainties of the raw mass and volume measurements, the estimated uncertainties for density and porosity are ±0.02 g/cm^3 and ±2%, respectively. The sedi-

Table 14. Index properties data for Site 900.

Core, section, interval (cm)	Depth (mbsf)	Sample wet mass (g)	Sample wet vol. (cm^3)	Sample dry mass (g)	Sample dry vol. (cm^3)	Bulk density (g/cm^3)	Grain density (g/cm^3)	Porosity (%)	Water content (% dry mass)
149-900A-									
1R-1, 24–25	0.24	12.61	7.53	7.65	2.75	1.68	2.80	63.35	68.80
1R-2, 30–32	1.11	15.54	9.36	9.37	3.37	1.66	2.80	64.14	69.90
2R-1, 30–31	1.80	12.89	7.65	7.91	2.86	1.69	2.78	62.42	66.79
3R-1, 80–81	11.90	9.68	5.77	5.78	2.08	1.68	2.80	63.15	71.65
3R-2, 64–65	13.24	9.04	5.08	5.79	2.02	1.78	2.88	59.33	59.37
4R-1, 120–121	22.00	8.00	4.63	4.88	1.73	1.73	2.84	61.22	67.90
4R-2, 62–63	22.92	9.33	5.32	5.89	1.90	1.75	3.12	65.23	61.84
4R-3, 60–61	24.40	9.73	5.67	5.96	2.11	1.72	2.85	62.00	67.09
4R-4, 80–81	26.10	8.46	4.91	5.16	1.80	1.72	2.89	62.50	67.79
4R-5, 50–51	27.30	10.27	5.82	6.58	2.36	1.77	2.81	58.41	59.33
5R-1, 65–66	31.05	9.94	5.54	6.50	2.30	1.79	2.84	57.56	55.91
5R-2, 74–75	32.64	8.56	4.60	5.77	2.04	1.86	2.84	54.00	51.01
5R-3, 100–101	34.40	9.53	5.03	6.61	2.31	1.90	2.88	53.00	46.50
5R-4, 90–91	35.80	12.15	6.91	7.87	2.81	1.76	2.81	58.96	57.49
5R-5, 50–51	36.90	10.35	5.80	6.80	2.43	1.78	2.81	57.45	55.14
6R-1, 85–86	40.85	12.96	7.38	8.39	3.02	1.76	2.79	58.56	57.56
6R-2, 80–81	42.30	9.48	5.22	6.31	2.24	1.82	2.83	56.16	53.05
6R-3, 80–81	43.80	9.24	5.16	6.01	2.13	1.79	2.83	57.66	56.76
6R-4, 82–83	45.32	11.98	6.56	8.11	2.86	1.83	2.85	56.07	50.31
6R-5, 81–82	46.81	10.56	5.93	6.88	2.46	1.78	2.81	57.63	56.52
6R-6, 60–61	48.10	11.72	6.41	7.91	2.82	1.83	2.81	55.13	50.83
7R-1, 67–68	50.27	11.32	6.27	7.61	2.70	1.81	2.83	56.81	51.45
7R-2, 70–71	51.80	11.72	6.33	8.04	2.83	1.85	2.85	54.74	48.24
7R-3, 75–76	53.35	11.43	6.28	7.70	2.75	1.82	2.82	55.54	51.08
7R-4, 80–81	54.90	11.06	5.97	7.56	2.70	1.85	2.81	53.62	48.80
7R-5, 83–84	56.43	11.97	6.18	8.70	3.12	1.94	2.80	48.56	39.49
7R-6, 22–23	57.32	11.68	6.07	8.41	3.01	1.92	2.81	49.46	40.89
8R-1, 100–101	60.30	11.52	6.19	7.93	2.79	1.86	2.86	54.29	47.68
8R-2, 80–81	61.60	11.96	6.66	7.95	2.84	1.80	2.81	56.84	53.26
8R-3, 50–51	62.80	13.41	7.32	9.19	3.28	1.83	2.81	54.82	48.40
9R-1, 84–85	65.34	9.24	5.01	6.28	2.26	1.85	2.79	53.58	49.67
9R-2, 74–75	66.74	10.27	5.35	7.31	2.58	1.92	2.84	50.81	42.62
9R-3, 27–28	67.77	8.73	4.80	5.83	2.06	1.82	2.85	56.35	52.47
10R-1, 74–76	74.84	11.75	6.68	7.62	2.72	1.76	2.81	58.93	57.31
10R-2, 112–114	76.72	14.59	8.22	9.69	3.49	1.78	2.79	57.48	53.36
10R-4, 84–86	79.44	13.29	7.41	8.84	3.21	1.79	2.76	55.80	53.11
11R-1, 30–32	84.00	11.38	6.23	7.66	2.72	1.82	2.82	55.51	51.26
11R-2, 26–28	85.46	14.68	8.13	9.87	3.53	1.81	2.81	56.22	51.40
11R-3, 24–26	86.94	12.24	6.75	8.21	2.93	1.81	2.81	55.89	51.80
11R-4, 42–44	88.62	12.71	7.10	8.45	3.01	1.79	2.82	57.33	53.20
11R-5, 22–24	89.92	13.53	7.45	9.21	3.32	1.82	2.78	55.04	49.46
12R-1, 34–36	93.74	10.64	5.78	7.21	2.55	1.84	2.84	55.08	50.16
12R-2, 23–25	95.13	12.93	6.94	8.99	3.25	1.86	2.77	52.09	46.14
12R-3, 23–25	96.63	14.61	7.95	10.04	3.64	1.84	2.77	53.36	47.96
12R-4, 14–16	98.04	13.25	7.33	8.93	3.21	1.81	2.79	55.71	51.05
14R-1, 36–38	113.06	12.71	6.63	9.11	3.29	1.92	2.78	49.08	41.55
14R-2, 49–51	114.69	17.68	9.55	12.41	4.61	1.85	2.70	50.67	44.68
14R-3, 48–50	116.18	17.74	9.63	12.38	4.59	1.84	2.71	51.36	45.57
14R-4, 48–50	117.68	18.13	9.82	12.66	4.54	1.85	2.80	53.70	45.50
14R-5, 49–51	119.19	15.78	8.49	11.02	3.95	1.86	2.80	53.00	45.46
14R-6, 51–53	120.71	14.65	7.83	10.32	3.72	1.87	2.78	51.89	44.15
14R-7, 35–37	122.05	14.91	7.98	10.51	3.78	1.87	2.79	52.23	44.05
15R-1, 69–71	123.09	14.36	7.46	10.45	3.76	1.92	2.79	48.92	39.30
15R-2, 49–51	124.39	13.20	7.33	8.89	3.18	1.80	2.81	56.45	51.13
15R-3, 49–51	125.89	14.16	7.69	8.75	3.54	1.84	2.48	43.79	65.56
15R-4, 34–36	127.24	16.57	8.93	11.70	4.27	1.86	2.75	51.84	43.80
16R-1, 94–96	132.94	12.04	6.49	8.31	3.02	1.85	2.76	52.17	47.28
16R-2, 101–103	134.51	16.77	9.02	11.80	4.28	1.86	2.77	52.11	44.31
16R-3, 100–102	136.00	12.51	6.99	8.35	3.04	1.79	2.76	55.88	52.56
16R-4, 19–51	136.69	17.39	9.27	12.42	4.51	1.88	2.76	51.00	42.07
16R-5, 45–47	138.45	16.82	8.98	11.96	4.37	1.87	2.75	50.72	42.75
16R-6, 59–61	140.09	16.01	8.62	11.34	4.11	1.86	2.77	52.27	43.31
17R-1, 81–82	142.41	11.14	5.85	7.87	2.78	1.90	2.84	51.60	43.74
17R-2, 60–61	143.70	11.89	6.03	8.86	3.23	1.97	2.75	45.10	35.90
17R-3, 28–29	144.88	11.40	5.80	8.31	3.03	1.96	2.75	45.47	39.08
18R-1, 80–81	152.10	9.93	5.21	7.02	2.50	1.90	2.81	50.83	43.62
18R-2, 90–91	153.70	9.60	4.86	7.05	2.55	1.98	2.78	45.65	37.98
18R-3, 75–76	155.05	10.50	5.68	7.21	2.61	1.85	2.78	52.91	48.09
18R-4, 84–85	156.64	12.87	7.15	8.69	3.14	1.80	2.78	55.77	50.71
18R-5, 23–24	157.53	15.22	8.28	10.60	3.88	1.84	2.75	52.64	45.88
19R-1, 108–111	161.98	11.51	6.06	8.19	3.01	1.90	2.73	48.72	42.66
19R-2, 49–50	162.89	9.17	4.56	6.82	2.43	2.01	2.81	44.86	36.17
20R-1, 133–134	171.93	10.97	5.56	8.07	2.87	1.97	2.82	47.19	37.74
20R-2, 67–68	172.77	10.36	5.11	7.88	2.79	2.03	2.83	44.56	32.99
20R-3, 73–76	174.33	12.22	6.35	8.78	3.14	1.92	2.80	49.48	41.20
20R-4, 73–74	175.83	12.19	6.14	9.12	3.29	1.99	2.78	45.29	35.31
20R-5, 87–88	177.47	11.90	6.26	8.46	3.02	1.90	2.81	50.91	42.75
20R-6, 85–86	178.95	11.67	5.97	8.56	3.08	1.96	2.79	47.24	38.14
20R-7, 33–34	179.93	9.43	5.05	6.42	2.31	1.87	2.79	52.30	49.44
21R-1, 83–84	181.13	10.43	5.38	7.58	2.70	1.94	2.81	48.97	39.51
21R-2, 83–84	182.63	9.81	5.09	7.02	2.56	1.93	2.75	47.71	41.80
21R-3, 80–81	184.10	10.56	5.72	7.25	2.64	1.84	2.75	52.53	48.12
21R-4, 56–59	185.36	12.34	6.64	8.64	3.15	1.86	2.75	51.75	45.09
21R-5, 63–64	186.93	12.81	6.84	9.08	3.28	1.87	2.78	51.59	43.20
21R-6, 77–78	188.57	12.15	6.51	8.64	3.21	1.87	2.70	49.72	42.73
22R-1, 98–99	190.88	9.94	5.35	6.98	2.60	1.86	2.70	50.07	44.64

Table 14 (continued).

Core, section, interval (cm)	Depth (mbsf)	Sample wet mass (g)	Sample wet vol. (cm^3)	Sample dry mass (g)	Sample dry vol. (cm^3)	Bulk density (g/cm^3)	Grain density (g/cm^3)	Porosity (%)	Water content (% dry mass)
22R-2, 80–81	192.20	10.37	5.46	7.46	2.71	1.90	2.76	49.67	41.03
22R-3, 80–83	193.70	14.34	7.57	10.35	3.77	1.89	2.75	49.70	40.53
22R-4, 84–85	195.24	9.92	5.19	7.19	2.66	1.91	2.72	47.45	39.90
22R-5, 79–80	196.69	10.85	5.99	7.25	2.67	1.81	2.73	53.74	52.41
22R-6, 60–61	198.00	14.26	7.54	10.25	3.71	1.89	2.78	50.43	41.11
23R-1, 29–31	199.79	14.36	7.33	10.71	3.90	1.96	2.75	45.94	35.77
23R-2, 27–29	201.27	11.50	5.99	8.28	2.97	1.92	2.79	49.47	40.89
23R-3, 24–26	202.74	12.32	6.54	8.68	3.13	1.88	2.78	51.11	44.15
23R-4, 50–52	204.50	13.97	7.19	10.28	3.71	1.94	2.78	47.67	37.68
23R-5, 46–48	205.96	12.09	6.19	8.96	3.24	1.95	2.77	46.88	36.67
23R-6, 33–34	207.33	10.55	5.41	7.74	2.81	1.95	2.77	46.79	38.13
23R-7, 34–36	208.84	13.91	7.31	10.09	3.69	1.90	2.74	48.90	39.78
24R-1, 31–33	209.51	12.18	6.49	8.69	3.19	1.88	2.74	50.14	42.25
24R-2, 29–31	210.99	14.03	7.53	9.83	3.59	1.86	2.75	51.32	44.95
24R-3, 54–56	212.74	13.59	6.92	10.33	3.70	1.96	2.80	47.08	33.09
24R-4, 38–40	214.08	13.62	7.02	10.04	3.62	1.94	2.78	47.86	37.45
24R-5, 33–35	215.53	11.13	5.61	8.42	3.07	1.99	2.75	44.42	33.75
24R-6, 22–23	216.92	9.10	4.69	6.49	2.33	1.94	2.79	48.26	42.32
25R-1, 49–51	219.29	11.21	5.94	7.93	2.88	1.89	2.76	50.33	43.50
25R-2, 50–52	220.80	14.91	7.70	11.05	4.04	1.94	2.74	46.95	36.67
25R-3, 51–53	222.31	14.38	7.29	10.83	3.94	1.97	2.76	45.28	34.36
25R-4, 55–57	223.85	11.35	5.56	8.74	3.18	2.04	2.75	41.23	31.29
25R-5, 17–19	224.97	12.31	6.55	8.89	3.28	1.88	2.72	49.53	40.45
25R-6, 19–21	226.49	13.58	7.17	9.95	3.54	1.89	2.82	51.56	38.32
26R-1, 31–33	228.71	12.48	6.32	9.56	3.52	1.98	2.72	44.06	32.02
26R-2, 30–32	230.20	12.78	6.59	9.32	3.42	1.94	2.73	46.46	38.98
26R-3, 41–43	231.81	13.47	6.79	10.21	3.68	1.98	2.78	45.40	33.48
26R-4, 21–23	232.66	12.74	6.67	9.25	3.40	1.91	2.73	48.02	39.62
26R-5, 30–32	234.25	14.73	7.41	11.18	4.10	1.99	2.73	43.64	33.30
26R-6, 20–22	235.65	14.17	7.30	10.54	3.86	1.94	2.73	46.47	36.15
26R-7, 22–23	236.12	11.03	5.48	8.34	3.04	2.01	2.75	42.78	33.83
27R-1, 21–23	238.31	14.16	7.04	10.84	3.92	2.01	2.77	43.56	32.09
27R-2, 14–16	239.74	14.45	7.22	11.01	4.03	2.00	2.74	43.01	32.76
27R-3, 20–22	241.30	14.13	7.45	10.34	3.77	1.90	2.75	49.49	38.51
27R-4, 20–22	242.80	10.84	5.40	8.36	3.11	2.01	2.69	41.08	31.09
27R-5, 21–23	244.31	12.52	6.40	10.39	3.47	1.96	3.00	52.85	21.40
27R-6, 22–24	245.82	14.06	7.16	10.64	3.87	1.96	2.76	45.76	33.69
28R-1, 73–74	248.53	12.19	6.27	8.97	3.27	1.94	2.75	46.73	37.70
28R-2, 85–86	250.15	12.98	6.75	9.47	3.45	1.92	2.75	47.99	38.92
28R-3, 90–91	251.70	12.19	6.38	8.96	3.29	1.91	2.73	48.06	37.83
28R-4, 68–69	252.98	9.18	4.68	6.75	2.45	1.96	2.76	46.10	37.78
28R-5, 49–52	254.29	11.04	5.74	8.06	2.98	1.92	2.72	46.77	38.82
28R-6, 64–65	255.94	10.47	5.33	7.73	2.79	1.96	2.77	46.39	37.22
29R-1, 78–79	258.28	12.67	6.73	8.98	3.27	1.88	2.76	50.43	43.23
29R-2, 107–110	260.07	13.37	7.09	9.55	3.52	1.89	2.72	49.26	42.06
29R-3, 27–28	260.77	10.88	5.76	7.74	2.82	1.89	2.75	50.00	42.69
29R-4, 74–75	261.83	11.91	6.15	8.84	3.27	1.94	2.71	45.89	36.46
29R-5, 80–81	263.39	10.85	5.62	7.92	2.87	1.93	2.77	48.01	38.84
29R-6, 71–72	264.80	10.56	5.46	7.74	2.84	1.93	2.73	46.76	38.28
29R-7, 40–41	265.99	11.17	5.81	8.17	3.00	1.92	2.73	47.38	38.55
30R-1, 68–69	267.78	12.32	6.35	9.04	3.32	1.94	2.73	46.36	38.10
30R-2, 79–80	269.39	10.80	5.60	7.85	2.87	1.93	2.74	47.39	39.47
30R-3, 80–83	270.90	10.67	5.52	7.87	2.92	1.93	2.71	45.89	37.36
30R-4, 75–76	272.35	10.95	5.77	7.80	2.83	1.90	2.77	49.86	42.45
30R-5, 62–63	273.72	13.51	7.13	9.70	3.58	1.89	2.71	48.56	41.31
30R-6, 70–71	275.30	11.29	5.90	8.28	3.07	1.91	2.70	47.07	38.18
31R-1, 87–88	277.57	8.52	4.22	6.44	2.27	2.02	2.84	45.35	33.87
31R-2, 100–103	279.20	9.01	4.63	6.57	2.38	1.94	2.76	47.13	39.01
31R-3, 92–93	280.62	11.88	6.12	8.75	3.13	1.94	2.81	48.52	37.57
31R-4, 100–101	282.20	12.37	6.38	9.12	3.35	1.94	2.73	46.35	37.40
31R-5, 87–88	283.57	13.08	6.69	9.82	3.59	1.95	2.74	45.80	34.81
32R-1, 39–40	286.79	6.79	3.36	5.12	1.88	2.02	2.73	41.62	34.22
32R-2, 83–96	288.73	9.32	4.67	6.97	2.53	1.99	2.76	44.08	35.36
32R-4, 83–84	290.83	11.15	5.59	8.52	3.14	1.99	2.72	42.73	32.33
32R-5, 80–81	292.30	9.34	4.78	6.74	2.40	1.95	2.82	48.20	40.55
32R-6, 82–83	293.82	12.04	6.12	9.00	3.25	1.97	2.78	46.19	35.44
34R-1, 92–93	306.52	11.50	5.86	8.56	3.08	1.96	2.79	46.82	36.03
34R-2, 103–106	308.13	13.62	6.98	10.16	3.73	1.95	2.73	45.66	35.73
34R-3, 88–89	309.48	13.03	6.64	9.79	3.61	1.96	2.72	44.67	34.73
34R-4, 48–49	310.58	11.95	6.21	8.67	3.15	1.92	2.76	48.16	39.75
33R-1, 36–37	296.36	10.86	5.38	8.40	3.03	2.02	2.78	43.37	30.69
33R-2, 40–41	297.90	10.87	5.45	8.15	2.93	2.00	2.79	45.08	35.03
33R-3, 39–42	299.39	12.50	6.49	9.14	3.34	1.93	2.74	47.56	38.60
33R-4, 86–87	301.36	11.65	5.90	8.69	3.15	1.97	2.77	45.46	35.74
33R-5, 70–71	302.70	11.19	5.72	8.35	3.04	1.96	2.76	46.16	35.67
33R-6, 77–78	304.27	10.54	5.24	7.96	2.86	2.01	2.79	44.15	33.98
35R-1, 30–32	315.60	10.76	5.29	8.23	2.95	2.04	2.80	43.09	32.23
35R-2, 33–35	317.13	10.25	5.06	7.77	2.78	2.03	2.80	43.72	33.47
35R-3, 21–23	318.51	14.42	7.05	11.31	4.10	2.04	2.76	41.32	28.77
35R-4, 18–20	319.98	12.54	6.17	9.60	3.45	2.03	2.79	42.88	32.08
35R-5, 31–33	321.61	13.76	6.86	10.52	3.79	2.01	2.78	44.19	32.29
36R-1, 41–43	325.31	13.05	6.41	10.13	3.83	2.04	2.65	37.79	30.20
36R-2, 30–32	326.70	13.25	6.44	10.34	3.74	2.06	2.77	40.88	29.47
36R-3, 32–34	328.22	13.49	6.52	10.64	3.86	2.07	2.76	39.87	28.03
36R-4, 30–32	329.70	9.74	4.63	7.62	2.71	2.10	2.82	39.86	29.13
36R-5, 27–29	331.17	12.98	6.16	10.32	3.73	2.11	2.77	38.06	26.96
36R-6, 25–26	332.65	8.83	4.33	6.63	2.38	2.04	2.79	42.64	34.82

Table 14 (continued).

Core, section, interval (cm)	Depth (mbsf)	Sample wet mass (g)	Sample wet vol. (cm^3)	Sample dry mass (g)	Sample dry vol. (cm^3)	Bulk density (g/cm^3)	Grain density (g/cm^3)	Porosity (%)	Water content (% dry mass)
37R-1, 54–55	335.04	12.57	6.20	9.70	3.51	2.03	2.77	42.55	31.01
37R-2, 50–52	336.50	12.22	5.82	9.56	3.46	2.10	2.77	38.41	29.14
37R-3, 43–45	337.93	12.48	6.14	9.58	3.40	2.03	2.83	44.06	31.72
37R-4, 25–47	339.25	13.30	6.54	10.32	3.77	2.03	2.74	41.29	30.25
37R-5, 28–29	340.78	11.21	5.31	8.77	3.18	2.11	2.77	37.58	29.12
37R-6, 41–43	342.41	12.06	5.86	9.35	3.38	2.06	2.77	40.89	30.34
38R-1, 30–32	344.50	10.61	5.15	8.14	2.94	2.06	2.78	40.89	31.78
38R-2, 28–30	345.98	11.95	5.81	9.29	3.40	2.06	2.74	39.81	29.98
38R-3, 29–31	347.49	11.90	5.69	9.35	3.39	2.09	2.76	38.65	28.56
38R-4, 21–22	348.91	13.19	6.41	10.41	3.88	2.06	2.69	37.92	27.94
38R-5, 28–30	350.48	12.45	6.01	9.83	3.52	2.07	2.80	41.01	27.89
38R-6, 46–47	352.16	9.87	4.55	7.98	2.85	2.17	2.81	35.77	24.77
39R-1, 17–18	353.97	11.26	5.36	8.97	3.26	2.10	2.75	37.86	26.71
39R-2, 22–24	355.52	12.51	5.97	9.91	3.57	2.09	2.78	39.03	27.45
39R-3, 26–28	357.06	11.93	5.58	9.50	3.39	2.14	2.81	37.63	26.76
39R-4, 20–22	358.50	12.82	6.17	10.05	3.61	2.08	2.79	40.36	28.84
39R-5, 26–27	360.06	11.13	5.30	8.82	3.18	2.10	2.78	38.70	27.42
39R-6, 29–30	361.59	11.24	5.09	9.34	3.37	2.21	2.77	32.40	21.23
40R-1, 25–27	363.75	11.15	5.37	8.26	2.98	2.08	2.78	40.12	36.72
40R-2, 32–34	365.32	10.41	4.97	8.14	2.93	2.10	2.79	39.24	29.19
40R-3, 20–22	366.70	12.28	5.82	10.40	3.60	2.11	2.89	41.93	18.85
40R-4, 25–26	368.25	10.59	5.05	8.42	3.05	2.09	2.76	38.39	26.97
40R-5, 31–33	369.81	12.76	6.41	9.89	3.60	1.99	2.76	44.14	30.39
40R-6, 35–37	371.35	13.69	6.21	11.18	4.08	2.20	2.74	31.39	23.45
41R-1, 95–97	374.15	15.65	8.26	11.35	4.16	1.89	2.73	49.16	39.82
41R-2, 67–69	375.37	13.72	6.52	11.02	4.00	2.10	2.76	37.79	25.63
41R-4, 56–57	377.45	13.87	7.00	10.45	3.81	1.98	2.75	44.57	34.31
41R-5, 90–91	379.29	13.14	6.52	10.12	3.68	2.02	2.76	42.82	31.27
41R-6, 115–116	381.04	11.07	5.37	8.62	3.12	2.06	2.77	40.55	29.78
41R-7, 36–37	381.75	11.13	5.32	8.80	3.24	2.09	2.72	37.10	27.71
42R-1, 61–62	383.51	14.47	7.05	11.53	4.31	2.05	2.68	37.90	26.67
42R-2, 70–71	385.10	12.60	5.99	10.15	3.70	2.11	2.75	37.44	25.23
42R-2, 97–99	385.37	7.79	3.03	7.10	2.56	2.57	2.78	11.71	10.11
42R-3, 103–104	386.93	11.54	5.42	9.26	3.39	2.13	2.74	35.51	25.74
42R-4, 74–75	388.14	12.40	6.05	9.63	3.50	2.05	2.76	40.90	30.13
42R-5, 100–101	389.90	13.83	6.73	10.84	3.94	2.06	2.76	40.56	28.87
42R-6, 62–63	391.02	16.12	7.98	12.56	4.63	2.02	2.72	41.23	29.67
43R-1, 74–75	393.34	10.90	5.44	8.29	2.99	2.00	2.78	44.26	33.01
43R-2, 78–79	394.88	10.28	4.92	8.04	2.90	2.09	2.78	39.34	29.15
43R-3, 70–73	396.30	9.65	4.65	7.51	2.74	2.08	2.75	39.04	29.85
43R-4, 68–69	397.78	9.32	4.06	7.89	2.87	2.30	2.76	26.51	18.91
43R-5, 55–56	399.15	7.10	3.17	5.82	2.06	2.24	2.83	32.74	22.98
43R-6, 47–48	400.57	11.97	5.73	9.53	3.47	2.09	2.75	38.37	26.79
44R-1, 77–79	403.07	13.41	6.37	10.75	3.88	2.10	2.77	38.29	25.86
44R-2, 74–77	404.54	9.49	4.27	7.87	2.82	2.22	2.80	32.37	21.49
44R-3, 60–61	405.90	13.79	6.68	10.93	3.95	2.07	2.77	40.55	27.38
44R-4, 57–58	407.37	11.38	5.30	9.16	3.32	2.15	2.77	35.49	25.33
44R-5, 53–54	408.35	15.66	7.75	12.20	4.50	2.02	2.72	41.15	29.69
45R-1, 90–91	412.90	14.90	7.23	11.78	4.27	2.06	2.77	40.47	27.71
45R-2, 73–74	414.23	12.95	6.33	10.18	3.71	2.05	2.75	40.84	28.48
45R-3, 47–50	415.47	15.39	7.98	11.35	4.15	1.93	2.74	47.40	37.38
45R-4, 88–89	417.38	12.07	5.76	9.61	3.50	2.09	2.75	37.95	26.79
45R-5, 70–72	418.70	15.43	7.54	12.07	4.37	2.05	2.77	41.42	29.14
46R-1, 20–23	421.80	13.85	6.67	10.80	3.88	2.07	2.79	40.40	29.58
46R-2, 21–23	423.31	11.50	5.39	9.07	3.20	2.13	2.84	38.98	28.05
46R-3, 22–24	424.82	11.01	5.06	8.96	3.20	2.18	2.81	35.39	23.91
46R-4, 28–29	426.38	13.74	6.64	10.76	3.86	2.07	2.80	41.00	28.99
46R-5, 20–22	427.80	10.42	4.85	8.38	2.99	2.15	2.81	37.02	25.46
46R-6, 22–24	429.32	11.86	5.88	9.05	3.17	2.02	2.86	46.01	32.54
47R-1, 36–38	431.46	12.30	5.52	10.30	3.71	2.23	2.78	31.49	20.27
47R-2, 30–32	432.90	13.14	6.15	10.61	3.82	2.14	2.79	36.80	24.92
47R-3, 31–33	434.41	14.84	7.06	12.00	4.38	2.10	2.74	37.35	24.74
47R-4, 36–38	435.96	14.56	6.70	11.96	4.31	2.17	2.78	34.54	22.71
47R-5, 26–28	437.36	12.88	5.98	10.46	3.77	2.15	2.78	35.64	24.17
47R-6, 22–24	438.82	11.01	5.12	8.89	3.12	2.15	2.86	38.56	24.94
48R-1, 18–20	440.78	9.25	4.18	7.53	2.70	2.21	2.79	32.81	23.87
48R-2, 25–27	442.35	10.76	4.93	8.76	3.15	2.18	2.79	34.29	23.86
48R-3, 25–27	443.85	9.97	4.58	8.02	2.78	2.18	2.89	38.31	25.44
48R-4, 25–27	445.35	10.45	4.94	8.22	2.88	2.12	2.86	40.61	28.39
48R-5, 20–22	446.80	12.28	5.77	9.73	3.48	2.13	2.80	37.89	27.42
48R-6, 23–25	448.33	12.23	5.80	9.64	3.49	2.11	2.77	37.84	28.11
49R-1, 27–29	450.47	12.08	5.74	9.54	3.41	2.10	2.80	39.30	27.87
49R-2, 32–34	452.02	12.21	5.79	9.67	3.49	2.11	2.78	38.16	27.49
49R-3, 18–20	453.38	11.22	5.17	9.01	3.24	2.17	2.78	34.96	25.65
49R-4, 25–27	454.95	12.06	5.60	9.64	3.48	2.15	2.78	35.54	26.26
49R-5, 39–41	456.59	14.38	6.74	11.61	4.19	2.13	2.78	36.69	24.93
49R-6, 23–25	457.93	12.54	5.83	10.08	3.61	2.15	2.80	36.51	25.52
49R-7, 38–39	459.58	9.41	4.30	7.58	2.72	2.19	2.79	34.19	25.25
50R-1, 13–15	460.03	13.06	6.07	10.52	3.77	2.15	2.79	36.38	25.25
50R-2, 29–31	461.69	12.25	5.68	9.94	3.60	2.16	2.77	35.02	24.28
50R-3, 24–26	463.14	13.71	6.18	11.41	4.14	2.22	2.76	31.24	21.04
50R-4, 26–28	464.66	12.02	5.63	9.59	3.45	2.13	2.78	36.92	26.50
50R-5, 24–25	466.00	12.46	5.84	9.92	3.52	2.13	2.83	38.39	26.77
51R-1, 50–52	470.40	13.22	6.09	10.77	3.85	2.17	2.80	35.53	23.78
51R-2, 50–52	471.90	13.07	6.19	10.74	3.88	2.11	2.77	37.84	22.66
51R-3, 46–48	473.36	12.20	5.68	10.31	3.71	2.15	2.78	36.12	19.12
51R-4, 52–54	474.92	12.00	5.41	9.88	3.51	2.22	2.82	33.57	22.42

Table 14 (continued).

Core, section, interval (cm)	Depth (mbsf)	Sample wet mass (g)	Sample wet vol. (cm^3)	Sample dry mass (g)	Sample dry vol. (cm^3)	Bulk density (g/cm^3)	Grain density (g/cm^3)	Porosity (%)	Water content (% dry mass)
51R-5, 67–68	476.57	13.01	5.93	10.76	3.81	2.19	2.83	35.21	21.83
51R-6, 52–54	477.92	12.81	5.91	10.44	3.70	2.17	2.83	36.63	23.72
52R-1, 81–82	480.01	13.37	6.18	10.83	3.83	2.16	2.83	37.02	24.51
52R-2, 114–115	481.84	12.70	5.97	10.17	3.65	2.13	2.79	37.60	26.03
52R-3, 107–110	483.27	10.96	5.16	8.68	3.14	2.13	2.77	37.04	27.48
52R-4, 73–74	484.43	10.12	4.58	8.33	2.98	2.21	2.80	33.27	22.43
52R-5, 83–84	486.03	10.81	4.91	8.87	3.18	2.20	2.80	33.50	22.84
52R-6, 55–56	487.25	9.82	4.46	7.99	2.81	2.20	2.85	35.48	23.94
53R-1, 83–85	489.73	12.31	5.66	10.06	3.59	2.17	2.81	35.47	23.37
53R-2, 52–53	490.92	9.38	4.41	7.42	2.66	2.13	2.80	37.75	27.64
53R-3, 63–64	492.24	9.93	4.56	7.93	2.81	2.18	2.83	36.07	26.38
53R-4, 54–57	493.65	10.35	4.86	8.18	2.91	2.13	2.81	38.33	27.75
53R-5, 64–65	495.25	13.48	6.65	10.36	3.79	2.03	2.74	41.54	31.54
53R-6, 51–53	496.62	14.40	6.84	11.47	4.10	2.11	2.81	39.28	26.71
54R-1, 91–92	499.51	14.43	6.81	11.58	4.18	2.12	2.77	37.50	25.74
54R-2, 39–41	500.49	12.74	6.06	10.14	3.62	2.10	2.81	39.53	26.81
54R-3, 68–69	502.28	9.80	4.48	7.86	2.81	2.19	2.80	34.58	25.81
54R-4, 69–70	503.79	10.49	4.74	8.61	3.11	2.22	2.78	32.07	22.80
56R-1, 53–54	518.53	8.89	4.10	7.07	2.51	2.17	2.83	36.45	26.92
56R-2, 80–83	520.30	12.38	6.00	9.62	3.46	2.06	2.79	41.09	30.04
56R-3, 19–20	521.19	12.82	6.14	10.03	3.57	2.09	2.81	40.62	29.13
56R-4, 68–69	522.43	14.29	6.81	11.39	4.14	2.10	2.76	38.02	26.62
56R-5, 84–85	524.09	12.31	5.94	9.60	3.48	2.07	2.77	39.81	29.55
57R-1, 51–52	528.11	12.87	7.07	9.81	3.56	1.82	2.76	54.20	32.71
57R-2, 66–68	529.76	11.55	5.51	9.09	3.29	2.10	2.77	38.56	28.32
57R-3, 82–83	531.42	13.69	6.89	10.32	3.73	1.99	2.77	44.99	34.23
57R-4, 100–102	533.10	11.68	5.74	8.85	3.17	2.03	2.80	43.07	33.52
57R-5, 104–105	534.64	16.17	7.89	12.61	4.58	2.05	2.76	40.91	29.56
58R-1, 63–66	537.83	14.96	6.77	12.61	4.60	2.21	2.74	31.11	19.45
58R-2, 64–65	539.34	14.49	6.87	11.59	4.17	2.11	2.78	38.37	26.16
58R-3, 70–71	540.90	8.42	3.90	6.59	2.33	2.16	2.83	37.35	29.07
59R-1, 59–60	547.49	13.93	6.74	10.83	3.90	2.07	2.78	40.75	29.98
59R-2, 85–87	549.25	13.73	6.54	10.79	3.90	2.10	2.77	38.53	28.51
59R-3, 131–132	551.21	13.06	5.97	10.73	3.84	2.19	2.80	34.45	22.68
59R-4, 79–81	552.19	10.28	5.16	7.63	3.75	1.99	2.03	3.97	36.46
59R-5, 73–74	553.63	11.92	5.67	9.27	3.29	2.10	2.83	40.17	29.95
59R-6, 25–27	554.65	12.47	5.83	9.91	3.57	2.14	2.78	36.59	27.04
60R-1, 31–32	556.91	11.99	5.23	10.19	3.64	2.29	2.80	28.71	18.42
60R-2, 17–18	558.27	16.05	7.32	13.17	4.75	2.19	2.78	33.36	22.84
60R-3, 23–24	559.83	16.19	7.17	13.73	4.94	2.26	2.79	29.90	18.68
60R-4, 52–53	561.62	13.00	6.07	10.34	3.68	2.14	2.81	37.63	26.90
60R-5, 22–24	562.82	8.37	3.82	6.64	2.29	2.19	2.91	38.09	27.26
61R-1, 51–52	566.71	10.66	5.00	8.38	2.94	2.13	2.86	39.62	28.47
61R-2, 26–27	567.96	11.93	5.50	9.63	3.39	2.17	2.85	37.20	24.98
61R-3, 30–32	569.50	11.75	5.15	9.88	3.58	2.28	2.76	27.73	19.76
61R-4, 39–41	571.09	11.35	5.40	8.88	3.15	2.10	2.82	40.20	29.13
62R-1, 86–88	576.76	9.29	4.31	7.34	2.61	2.15	2.82	36.97	27.81
62R-2, 31–33	577.71	12.32	4.78	11.58	4.26	2.58	2.72	8.38	6.64
62R-3, 54–55	578.57	11.82	5.77	8.98	3.24	2.05	2.78	41.60	33.15
63R-1, 42–44	586.02	11.85	5.44	9.58	3.47	2.18	2.77	33.76	24.78
63R-2, 43–45	587.53	12.02	5.54	9.66	3.44	2.17	2.81	36.02	25.55
64R-1, 29–31	595.39	10.73	4.93	8.67	3.08	2.18	2.82	35.84	24.82
64R-2, 18–19	596.78	11.84	5.56	9.32	3.38	2.13	2.76	36.47	28.31
65R-1, 43–44	605.03	11.74	5.38	9.46	3.46	2.18	2.74	32.50	25.20
65R-2, 11–12	606.21	11.78	5.35	9.58	3.46	2.20	2.77	32.68	24.00
65R-3, 28–30	607.14	12.44	5.59	10.23	3.69	2.23	2.78	31.51	22.57
66R-1, 66–68	614.76	13.42	6.36	10.66	3.90	2.11	2.74	36.65	27.10
66R-2, 10–12	615.70	11.80	5.24	9.89	3.60	2.25	2.75	28.94	20.15
67R-1, 117–118	624.97	13.29	5.66	11.64	4.24	2.35	2.75	23.21	14.76
67R-2, 57–59	625.87	10.45	4.60	8.72	3.14	2.27	2.79	29.05	20.70
67R-3, 52–54	627.32	10.19	4.43	8.62	3.09	2.30	2.79	27.87	19.00
68R-1, 110–112	634.50	9.20	4.17	7.45	2.66	2.21	2.81	33.69	24.54
68R-2, 111–112	636.01	12.93	6.35	9.80	3.54	2.04	2.78	42.25	33.49
68R-3, 28–30	636.68	10.08	4.39	8.39	2.99	2.30	2.81	28.82	21.02
69R-1, 40–41	643.50	7.16	3.17	5.76	2.01	2.26	2.87	33.20	25.43
69R-2, 132–133	645.92	10.09	4.14	8.89	3.18	2.43	2.79	20.35	14.06
70R-1, 66–69	653.36	10.45	4.78	8.37	2.98	2.19	2.82	35.14	25.98
70R-2, 71–73	654.91	9.13	3.65	8.18	2.91	2.50	2.81	17.44	12.08
71R-1, 19–20	662.59	14.74	6.46	12.57	4.52	2.28	2.78	28.57	18.01
71R-2, 21–23	664.11	17.91	6.76	17.33	6.40	2.65	2.71	3.51	3.47
71R-4, 18–20	666.13	14.28	6.09	12.37	4.44	2.34	2.79	25.20	16.09
72R-1, 123–125	673.33	14.16	6.35	11.77	4.19	2.23	2.82	32.67	21.20
72R-2, 29–31	673.89	9.65	3.55	9.24	3.32	2.72	2.79	3.75	4.60
73R-1, 54–56	682.24	9.90	4.30	8.25	2.93	2.30	2.82	28.88	20.88
73R-2, 29–31	683.49	8.26	2.92	7.99	2.90	2.83	2.76	-4.20	3.50
73R-3, 31–33	684.99	11.09	4.46	9.90	3.55	2.48	2.79	17.24	12.52
74R-1, 48–50	691.88	11.06	5.03	9.11	3.24	2.20	2.82	34.52	22.37
74R-2, 10–12	693.00	13.62	5.01	13.26	4.87	2.72	2.73	0.28	2.82
75R-1, 74–75	701.84	5.74	1.91	5.67	1.98	3.00	2.86	-7.68	1.28
75R-2, 51–53	702.82	9.13	3.93	7.64	2.70	2.32	2.83	28.27	20.36
76R-1, 103–105	711.43	11.80	5.42	9.60	3.44	2.18	2.80	34.94	23.95
76R-2, 92–93	712.82	13.88	5.76	12.39	4.49	2.41	2.76	20.29	12.52
77R-1, 87–90	720.87	10.43	4.84	8.43	3.08	2.16	2.75	34.22	24.79
77R-2, 127–129	722.77	10.44	4.87	8.38	3.10	2.15	2.71	33.56	25.71
78R-1, 70–71	730.40	7.61	3.41	6.18	2.19	2.23	2.83	33.04	24.17
78R-2, 51–53	731.71	9.49	4.43	7.43	2.66	2.14	2.80	37.05	29.03
80R-1, 70–73	749.60	23.53	9.27	22.25	8.34	2.54	2.67	7.94	5.97

Table 14 (continued).

Core, section, interval (cm)	Depth (mbsf)	Sample wet mass (g)	Sample wet vol. (cm^3)	Sample dry mass (g)	Sample dry vol. (cm^3)	Bulk density (g/cm^3)	Grain density (g/cm^3)	Porosity (%)	Water content (% dry mass)
80R-2, 43–46	750.60	21.00	8.56	19.10	6.97	2.45	2.74	16.83	10.35
80R-2, 108–111	751.25	26.63	9.72	26.29	9.63	2.74	2.73	–0.55	1.34
80R-2, 14–17	750.31	26.20	10.98	23.63	8.73	2.39	2.71	19.16	11.32
81R-1, 83–86	759.33	18.09	6.42	17.65	6.33	2.82	2.79	–1.64	2.59
81R-2, 74–77	760.66	23.47	8.50	22.69	8.37	2.76	2.71	–2.94	3.57
81R-3, 10–13	761.43	33.87	12.52	32.73	11.73	2.71	2.79	4.86	3.61
82R-1, 87–90	768.67	26.21	9.47	25.71	9.29	2.77	2.77	0.01	2.02
82R-3, 83–86	771.41	24.69	8.63	24.62	8.71	2.86	2.83	–1.90	0.29
82R-3, 52–55	771.10	23.55	8.58	23.08	8.43	2.74	2.74	–0.38	2.11
82R-5, 54–57	773.62	26.40	9.61	25.88	9.47	2.75	2.73	–0.81	2.08
83R-1, 46–49	774.46	25.76	9.47	24.99	8.94	2.72	2.80	4.28	3.20
83R-2, 81–83	776.14	25.85	8.95	25.71	8.98	2.89	2.86	–1.36	0.56
84R-1, 81–84	778.31	21.37	8.10	20.57	7.53	2.64	2.73	5.52	4.04
84R-2, 56–59	779.43	26.57	10.84	24.52	9.05	2.45	2.71	15.41	8.69
84R-3, 77–80	781.11	20.91	8.54	19.05	7.00	2.45	2.72	16.18	10.15
84R-4, 82–85	782.58	34.98	11.74	34.96	11.78	2.98	2.97	–0.61	0.06
85R-1, 56–59	787.26	30.08	10.04	30.03	10.04	3.00	2.99	–0.25	0.17
85R-2, 68–71	788.61	26.17	9.06	25.69	9.02	2.89	2.85	–2.19	1.94
85R-4, 75–78	791.15	29.54	10.73	28.91	10.46	2.75	2.76	0.65	2.26
85R-5, 41–44	792.18	29.84	10.17	29.59	10.17	2.93	2.91	–1.29	0.88
85R-6, 131–134	794.49	32.60	11.20	32.56	11.20	2.91	2.91	–0.19	0.13
85R-4, 109–112	791.49	34.85	12.06	34.50	12.04	2.89	2.87	–1.30	1.05
86R-1, 65–67	796.35	16.75	5.85	16.72	5.85	2.86	2.86	–0.28	0.19

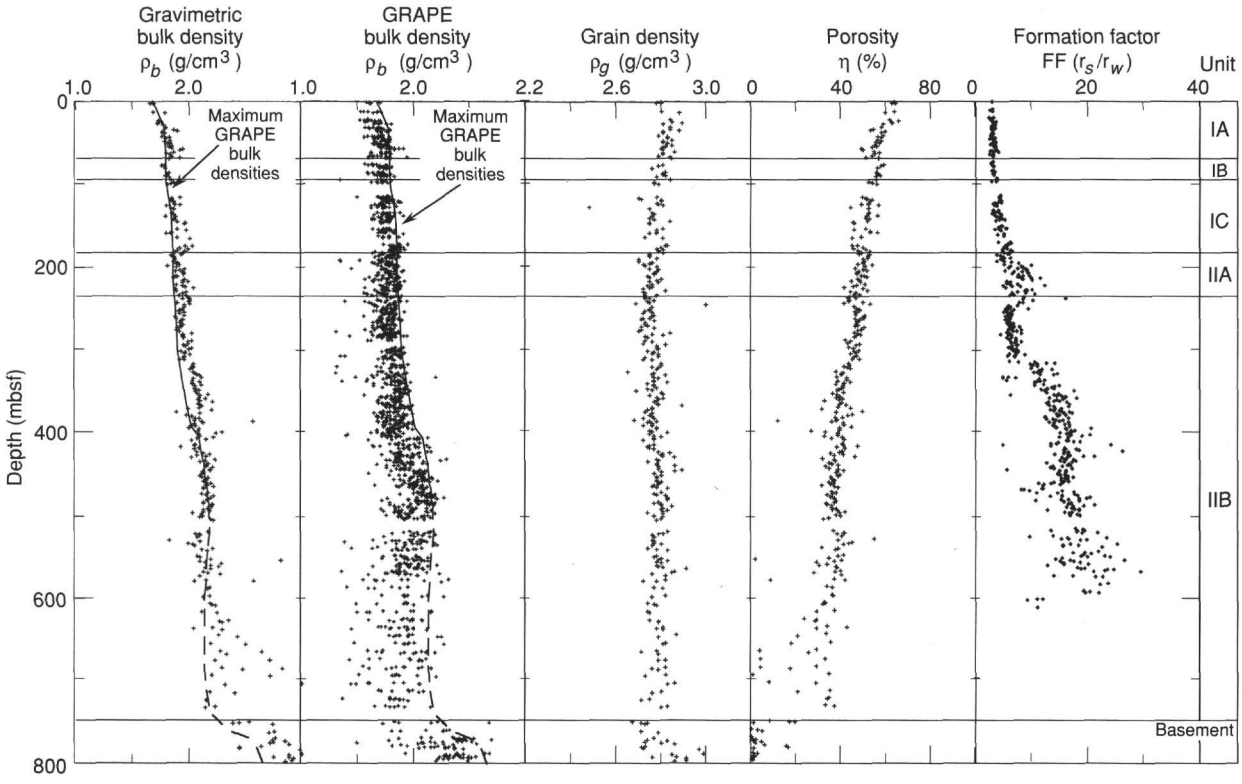

Figure 38. Gravimetrically determined and GRAPE-estimated bulk densities, grain density, porosity, and formation factor data for Hole 900A. The solid line indicates the maximum bulk density estimates from the GRAPE data.

mentary section at Site 900 yielded fairly smooth downhole trends in bulk density, grain density, and porosity. Minor offsets of these trends may be attributed to changes in lithology and degree of lithification. Gravimetrically determined bulk density increases nearly linearly from 1.7 g/cm^3 at the seafloor to about 2.2 g/cm^3 at a depth of 620 mbsf, while porosity decreases from about 65% to 32% (Fig. 38). Minor undulations in the trends were observed near 67, 180, and between 370 and 420 mbsf. The first of these corresponds to the boundary between lithostratigraphic Subunits IA and IB, and an associated downhole decrease in carbonate content (see "Lithostratigraphy" section, this chapter). The second corresponds to the boundary between Subunits IC and IIA, which show little difference in composition.

Below 180 mbsf, the sediments gradually become more lithified without major abrupt changes in bulk density and porosity. Minor changes in the downhole trend may be attributed to variations in the lithification state of the sediment. Below about 620 mbsf, the data exhibit considerable scatter with lower bulk density and higher porosity values. The highest bulk density and lowest porosity measurements (several near 0%) are associated with highly cemented calcareous sandstones interbedded with the silty claystones. Grain den-

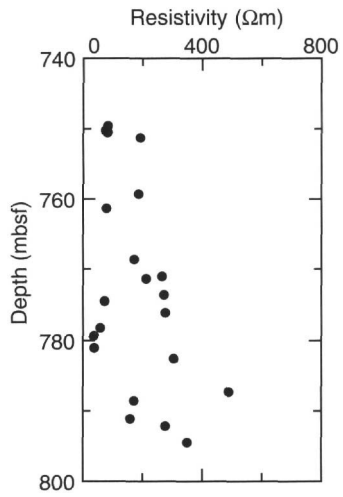

Figure 39. Electrical resistivity measurements on basement rocks from Hole 900A.

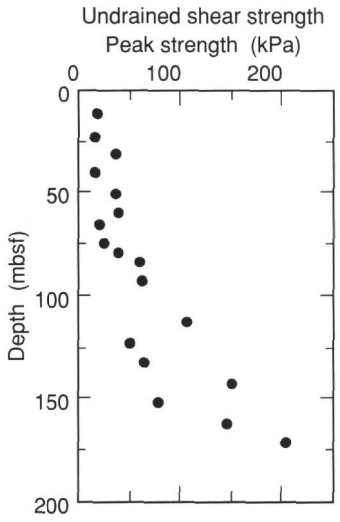

Figure 40. Undrained shear strength measurements on sediments from Hole 900A.

sities decrease from about 2.8 g/cm^3 near the seafloor to about 2.75 g/cm^3 at about 200 mbsf. Grain densities increase gradually between 200 and 420 mbsf, and maintain a relatively uniform value of 2.8 g/cm^3 below 420 mbsf.

Index properties below 748.9 mbsf reflect sampling of crystalline basement. Bulk density approaches 3.0 g/cm^3 (close to the grain density), and porosity is effectively 0%. Grain density increases sharply downward near the top of the crystalline basement, increasing from 2.8 g/cm^3 at 748.9 mbsf to about 3.0 g/cm^3 at 796.4 mbsf. This increase can be attributed to the downhole decrease in calcite veining and degree of alteration, with the deeper values reflecting the higher grain densities of the fine-grained metamorphosed gabbro (see "Igneous and Metamorphic Petrology and Geochemistry" section, this chapter).

GRAPE Measurements

Bulk densities were also estimated from whole-core GRAPE measurements taken in all sections recovered from Hole 900A (see "Explanatory Notes" chapter, this volume). In the sedimentary section, the curve defined by the maximum GRAPE density measurements best fit the corresponding gravimetrically determined bulk density (Boyce, 1973; Gealy, 1971).

The maximum GRAPE density measurements are indicated by the curve in Figure 38. In the sedimentary section, above approximately 300 mbsf, the GRAPE density estimates increase from 1.75 to 1.9 g/cm^3. The bulk density increases more rapidly with depth, from about 1.9 g/cm^3 near 300 mbsf to 2.2 g/cm^3 at 500 mbsf. The high degree of fracturing observed in the lower sedimentary section results in large scatter in the data below 500 mbsf, but the maximum densities are nearly constant at 2.2 g/cm^3. In basement cores, GRAPE bulk density increases from about 2.4 to 2.7 g/cm^3 at the base of the hole (796.4 mbsf).

Electrical Resistivity

Electrical resistivity was measured at intervals of 0.5 to 0.75 m in split cores from the sedimentary section above 655.5 mbsf (Cores 149-900A-2R to -71R), and in drilled minicores in the more lithified rocks in Cores 149-900A-80R to -86R. Formation factors were calculated for the interval down to 620 mbsf (see "Explanatory Notes" chapter, this volume). In the upper 320 mbsf, the formation factor increase linearly with depth from 2.5 to 7.0, although locally between 200 and 250 mbsf larger scattered values up to 12 were observed (Fig. 38). At 320 mbsf, an abrupt increase from 7 to 10 can be seen. Below this depth, the average formation factor increases downhole to 20 at 620 mbsf.

Electrical resistivity in the basement rocks (Fig. 39) ranges from 50 to 500 Ωm . Values lower than 100 Ωm were observed in altered breccias (748-755 mbsf) and microbreccias (778 and 782 mbsf; see "Igneous and Metamorphic Petrology and Geochemistry" section, this chapter). Electrical resistivity values higher than 100 Ωm generally were observed in microgabbros and strongly correlate inversely with the degree of veining and directly with the degree of metamorphism. The maximum resistivity (500 Ωm at 787 mbsf) was measured in a metamorphosed microgabbro without any veining.

Undrained Shear Strength

Undrained shear strength was measured in Cores 149-900A-3R to -20R using the shear vane apparatus (see "Explanatory Notes" chapter, this volume; Fig. 40). Peak shear strength increases downhole from 18 kPa at 12 mbsf to about 205 kPa at 172 mbsf. Between 12 and 80 mbsf, the measured peak strength oscillates between 15 and 45 kPa, showing only a slight net increase with depth. Below 80 mbsf, the measured values exhibit a much wider variation (possibly reflecting different degrees of lithification), but there appears to be a more pronounced trend of increasing peak strength with depth.

Acoustic Velocity

Discrete acoustic velocity was measured in Cores 149-900A-3R to -85R (Table 15). The DSV was used on Cores 149-900A-3R to -18R to measure velocity in sediment from depths shallower than 152 mbsf. The Hamilton Frame Velocimeter was used to measure velocities in more cohesive or indurated sediments and basement samples in Cores 149-900A-18R to -85R. The sedimentary samples were trimmed into cubes, and velocity was measured in three mutually orthogonal directions (see "Explanatory Notes" chapter, this volume). Compressional-wave velocity in basement rock was measured in the horizontal direction in minicores. Repeated measurements of selected samples and calibration standards suggest an accuracy of 2% to 3% for the velocity measurements.

Discrete acoustic velocity measurements in the sedimentary section show a general increase with depth, from about 1490 m/s at 10 mbsf to 2400 m/s at 730 mbsf (Fig. 41). Velocity measured in the vertical direction in the clays, silty clays, and claystones shows a linear trend with a slope of 1.06 s^{-1} and a correlation coefficient of 0.92. The horizontal velocities show similar downhole variations. Acoustic anisotropy in the intervals 180 to 240 mbsf and 340 to 460 mbsf is significantly higher than the estimated 4% uncertainty in the anisotropy calculation and can generally be attributed to slower propagation in the

Table 15. Discrete acoustic velocity measurements in cores from Site 900.

Core, section, interval (cm)	Depth (mbsf)	Velocity (m/s) V	H_x	H_y
149-900A-				
3R-1, 31–38	11.42	1492		
4R-1, 102–109	21.82	1492		
4R-4, 21–28	25.51	1492		
5R-1, 25–32	30.65	1525		
6R-1, 63–70	40.25	1529		
7R-1, 81–88	50.41	1525		
8R-1, 60–67	59.90	1525		
9R-1, 64–71	65.14	1525		
10R-1, 72–79	74.82	1529		
11R-1, 27–35	83.97	1560		
12R-1, 32–39	93.72	1574		
14R-1, 32–39	113.02	1618		
15R-1, 66–73	123.06	1596		
17R-1, 47–54	142.07	1596		
18R-1, 44–51	151.74	1525		
18R-2, 77–79	153.97	1735	1680	1763
19R-1, 108–111	161.98	1658	1693	1664
20R-3, 73–76	174.43	1660	1730	1727
21R-4, 56–59	185.36	1690	1783	1800
22R-3, 80–83	193.70	1779	1734	1667
23R-6, 31–33	207.33	1818	1706	1790
24R-6, 21–23	216.96	1714	1702	1774
25R-1, 49–50	219.29	1613	1795	1651
26R-7, 20–22	236.55	1625	1747	1773
27R-3, 20–22	241.30	1802	1776	1917
28R-5, 49–52	254.29	1770	1785	1767
29R-2, 107–110	260.07	1743	1670	1716
30R-3, 80–83	270.90	1765	1842	1791
31R-2, 100–103	279.20	1785	1790	1842
32R-2, 83–86	288.73	1778	1798	1800
34R-2, 103–106	308.13	1800	1835	1839
35R-2, 35–37	317.15	1894	1790	1784
36R-6, 23–25	332.63	1874	1841	1911
37R-1, 52–54	335.02	1873	1970	1966
38R-6, 48–50	344.68	1827	1823	1909
39R-1, 18–20	353.98	1776	1933	1835
40R-6, 37–39	371.37	1940	1919	2006
41R-4, 138–140	378.27	1816	1940	1938
42R-2, 93–96	385.33	3434	3594	3736
44R-2, 74–77	404.54	2248	2323	2348
45R-3, 47–50	415.47	1845	2087	1807
46R-1, 28–30	421.88	2137	2271	2034
46R-1, 142–144	423.02	2096		
47R-2, 67–69	433.27	1977	1842	2672
48R-5, 141–143	448.03	1848	1744	1528
49R-6, 21–23	457.91	1961	2077	2008
50R-5, 21–23	465.97	1958	1950	1957
51R-3, 44–46	473.34	1901	2028	2069
52R-3, 107–110	483.27	1931	2039	2070
53R-4, 54–57	493.65	1971	2030	1978
54R-2, 38–41	500.48	1996	2097	2075
56R-2, 80–83	520.30	1891	1910	1990
57R-4, 100–102	533.10	1933	1957	1862
58R-1, 63–66	537.83	2274	2372	2314
62R-1, 20–22	576.10	1877	2058	2314
65R-1, 43–44	605.03	2073	2089	2037
67R-2, 57–59	625.87	2213	2491	2443
67R-3, 52–54	627.32	2271	2560	2577
68R-1, 110–112	634.50	2299	2724	2636
69R-2, 132–133	645.92	2984	2682	3238
70R-1, 66–69	653.36	1999	2294	2266
70R-2, 71–73	654.91	2903	3411	3434
71R-1, 20–22	662.60	2022	2371	2517
72R-1, 45–47	672.55	3450	3249	3057
73R-2, 17–19	683.37	2352	2711	2701
75R-1, 74–75	701.84	5917	6337	6357
76R-1, 103–105	711.43			2130
77R-1, 127–129	721.27			2213
78R-1, 121–123	730.91			2395
80R-1, 70–73	749.60			5860
80R-2, 14–17	750.31			3738
80R-2, 43–46	750.60			4330
80R-2, 108–111	751.25			6858
81R-1, 83–86	759.33			5605
81R-2, 74–72	760.66			5010
81R-3, 10–13	761.43			5579
82R-1, 87–90	768.67			6910
82R-3, 52–55	771.10			5535
82R-3, 83–86	771.41			6853
82R-5, 54–57	773.57			5817
83R-1, 46–49	774.46			5388
83R-2, 81–83	776.14			6615
84R-1, 81–84	778.34			5604
84R-2, 56–59	779.43			3754
84R-3, 77–80	781.11			4325
84R-4, 82–85	782.58			7522
85R-4, 75–78	791.15			5616
85R-5, 41–44	791.18			5765
85R-1, 56–59	787.36			7575
85R-2, 68–71	788.61			6042
85R-6, 131–134	794.49			6310

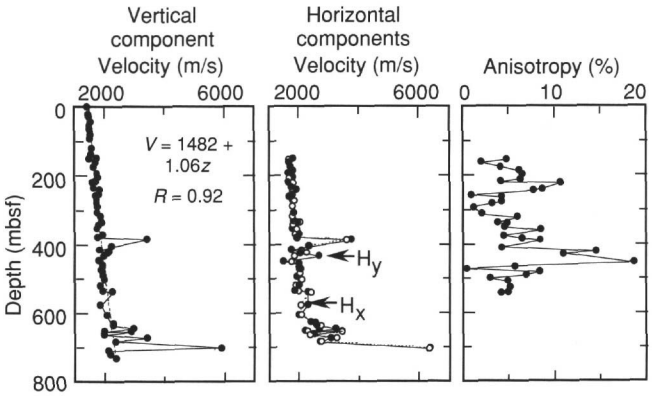

Figure 41. Acoustic velocity and anisotropy measurements made on cores from the sedimentary sequence in Hole 900A. The vertical velocity (V) was measured along the axis of the core. Horizontal velocities were measured perpendicular to the core axis, parallel to the split face of the core (H_x) and normal to the split face of the core (H_y). The downhole increase in the vertical velocity shows a linear trend (dashed line) with a correlation coefficient (R) of 0.92.

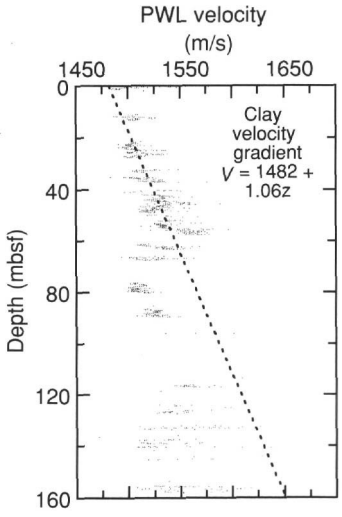

Figure 42. PWL velocity data from Hole 900A. Dashed line indicates linear clay velocity gradient estimated from discrete measurements shown in Figure 41.

vertical direction (Table 15). Acoustic anisotropy was not calculated for samples from cores below 550 mbsf (Cores 149-900A-62R to -78R) because horizontal fractures developed during sampling, resulting in an artificially slow velocity in the vertical direction. Velocities measured in the horizontal directions in these samples were not affected by the fracturing and are thought to be representative of the true horizontal velocity of the sample. Velocities greater than 3000 m/s in Figure 41 are from cemented siltstone (the sample at about 400 mbsf) or well-indurated silty claystone (the samples below 630 mbsf).

Compressional-wave velocity also was measured with the PWL in unsplit sections from Cores 149-900A-1R to -18R. This corresponds to the interval in which discrete velocity measurements were taken

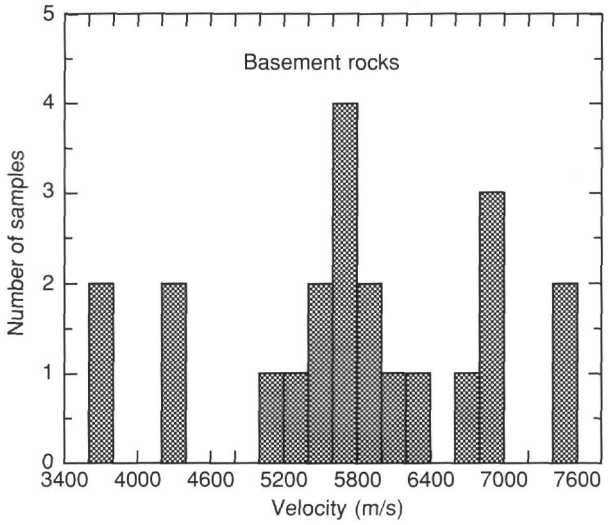

Figure 43. Histogram illustrating distribution of acoustic velocities measured in basement rocks from Hole 900A.

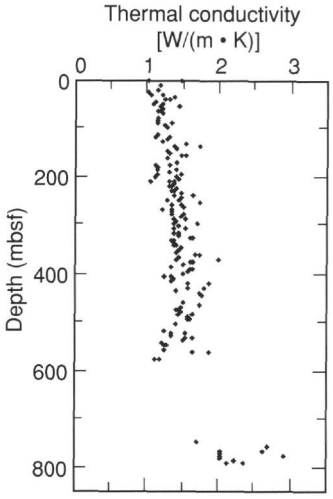

Figure 44. Thermal conductivity data of sediments and rocks from Hole 900A.

with the DSV. From 0 to 65 mbsf (Cores 140-900A-1R to -9R), the PWL velocities show a trend consistent with the linear increase in velocity with depth observed in the discrete velocity measurements of the clays and claystones (Fig. 42). The clay velocity gradient derived from the DSV measurements provides an upper bound on the PWL velocities below 110 mbsf (Cores 149-900A-14R to -19R). Average PWL velocities measured in cores from depths between 74 and 103 mbsf (Cores 149-900A-10R to -12R) are significantly lower than the discrete velocity measurements.

Acoustic velocities in the basement rocks show wide scatter that ranges from 3750 to 7600 m/s (Table 15). The velocities show some clustering about 5700 m/s (Fig. 43). No systematic variation of velocity with depth was observed in the basement rocks (Table 15).

Magnetic Susceptibility

Magnetic susceptibility was measured at intervals of 3 to 5 cm in all cores collected at Site 900. The results are discussed in the "Paleomagnetism" section (this chapter).

Thermal Conductivity

Thermal conductivity for Site 900 was measured in every other section of Cores 149-900A-1R to -60R within the sediments and in the basement Cores 149-900A-80R to -85R (Fig. 44; Table 16). The mean uncertainty associated with these measurements was estimated as ±0.2 W/(m·K). In the sedimentary section, the thermal conductivity values show only a slight increase with depth. Between 0 and 115 mbsf, the average thermal conductivity is 1.2 W/(m·K) (Fig. 44; Table 16). In the interval between 115 and 370 mbsf, the mean value is 1.4 W/(m·K) and a slight increase with depth can be observed. The data points show larger scatter around a mean value of 1.5 W/(m·K) from 370 to 563 mbsf, whereas the crystalline rocks exhibit much higher thermal conductivity values that range between 1.7 and 2.9 W/(m·K) in the depth interval from 749 to 794 mbsf.

DOWNHOLE LOGGING

Logging Operations

Three logging runs were made in Hole 900A using two different tool strings that obtained data from only part of the total depth of the hole. Total penetration in Hole 900A was 805.0 mbsf (5853.5 mbrf). The wiper trip made in preparation for logging encountered drag during the upward trip in the intervals 770-763, 753, and 600-543 mbsf. The subsequent wiper trip downward had to ream through the interval from 563 to 568 mbsf and a tight spot at 588 mbsf.

The geophysical combination was run first. Data were recorded on two passes, the first upward from a bridge encountered in the hole at 238 mbsf to the drill pipe at 137 mbsf. The pipe then was lowered through this bridge to 330 mbsf, and a second pass run upward from a lower bridge at 451 mbsf to the drill pipe at 330 mbsf.

The Formation Microscanner (FMS) combination was used for the third and final run. We also used the conical side-entry sub (CSES) for this run because of the bridges previously encountered in the hole. The CSES was assembled on the drill string so as to allow logging up to 220 mbsf. The pipe was then worked down to 753 mbsf. FMS data were acquired upward from 785 to 712 mbsf. A bridge at 731 mbsf prevented lowering the tool for a repeat run. A second pass from the bridge at 731 mbsf upward ended at 646 mbsf, when the tool became stuck. We freed the tool by lowering the drill string down over it. We raised the drill string above this bad spot in the hole and attempted again to obtain FMS data, but it became apparent that the cable had been damaged when we freed the tool at 646 mbsf. The tool became stuck again during these attempts and, again, was freed by lowering the pipe over the tool. Cable problems and deteriorating hole conditions forced us to abandon further efforts to log this hole.

The Lamont-Doherty temperature tool was not used in this hole. A "hole finder" was substituted at the bottom of the geophysical combination to try to increase the possibility of passing hole constrictions. The temperature tool was omitted from the FMS combination because the CSES was deployed. Following is a summary of the logging runs.

Run 1

Pass 1: Geophysical combination; drill-pipe depth, 137 mbsf (5185.4 mbrf).

Logged interval: 137-238 mbsf; speed, 600 ft/hr (190 m/hr).

Tools: natural gamma-ray/shear sonic/resistivity.

Pass 2: Geophysical combination; drill-pipe depth, 330 mbsf (5378.7 mbrf).

Logged interval: 330-451 mbsf; speed, 600 ft/hr (190 m/hr).

Tools: natural gamma-ray/shear sonic/resistivity.

Run 2

FMS combination; drill-pipe depth, variable (using CSES).

Logged intervals: 646-731 and 712-785 mbsf; speed, 600 ft/hr (190 m/hr).

Tools: natural gamma-ray /FMS.

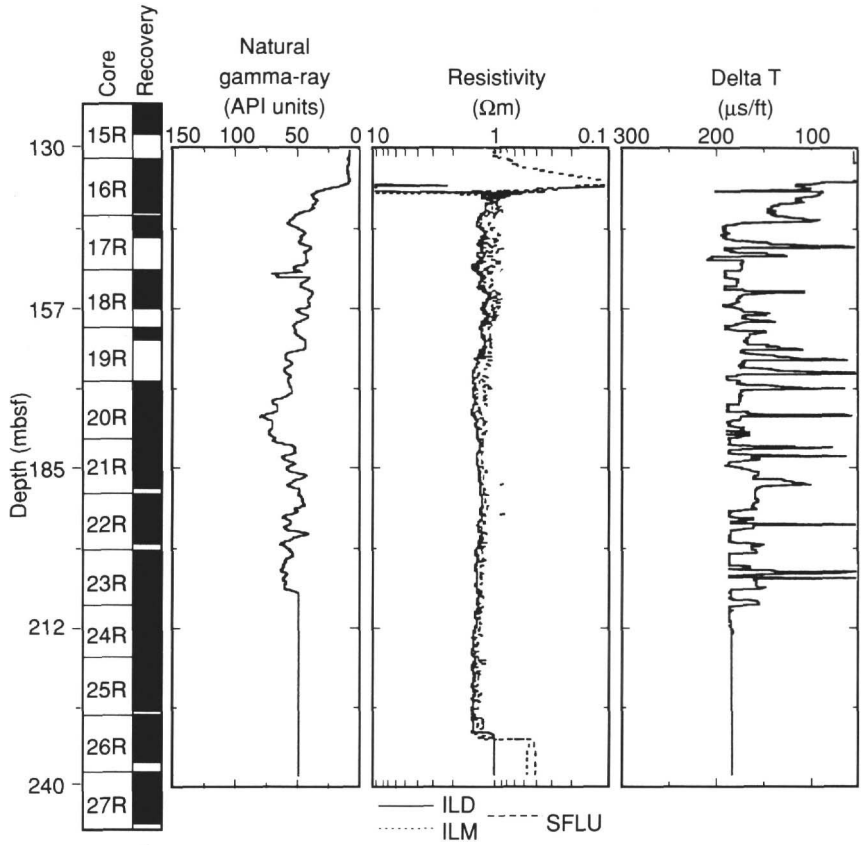

Figure 45. Composite plot of downhole logging data recorded at Hole 900A from the interval at 130-240 mbsf. Natural gamma-ray, resistivity, and sonic data are from the nuclear-sonic combination tool string. A five-point linear moving-average filter was applied to the natural gamma-ray data.

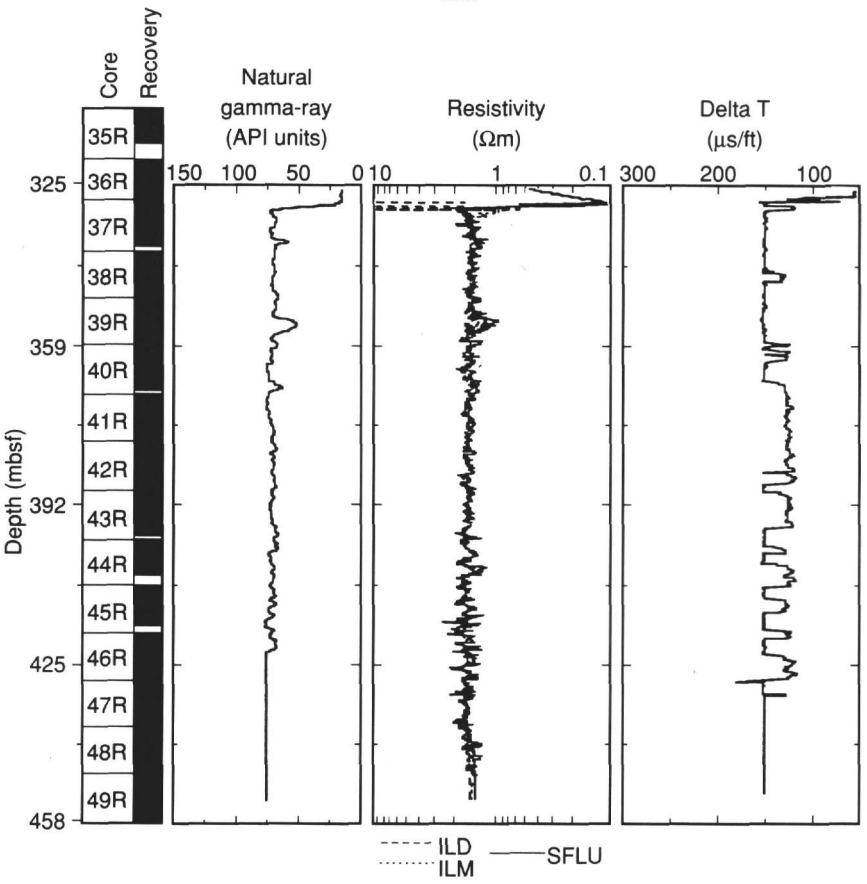

Figure 46. Composite plot of downhole logging data recorded at Hole 900A from the interval at 325-460 mbsf. Natural gamma-ray, resistivity, and sonic data are from the nuclear-sonic combination tool string. A five-point linear moving-average filter was applied to the natural gamma-ray data.

Table 16. Thermal conductivity data from Site 900.

Core, section	Depth (mbsf)	Thermal conductivity (W/m·K)
149-900A-		
1R-1	0.25	1.48
2R-1	1.75	1.02
3R-1	11.85	1.20
4R-1	21.55	1.17
4R-3	24.55	1.03
4R-5	27.30	1.07
5R-1	31.15	1.23
5R-3	34.15	1.37
5R-5	37.00	1.24
6R-1	40.75	1.31
6R-3	43.75	1.13
6R-5	46.75	1.08
7R-1	50.35	1.24
7R-3	53.35	1.20
7R-5	56.35	1.43
8R-1	60.05	1.23
8R-3	63.05	1.14
9R-1	65.25	1.19
9R-3	67.75	1.23
10R-3	77.85	1.15
11R-1	84.45	1.15
11R-3	87.45	1.35
11R-5	90.10	1.15
12R-1	94.15	1.24
12R-3	97.15	1.29
14R-1	113.40	1.17
14R-1	113.40	1.17
14R-3	116.40	1.11
14R-5	119.40	1.30
15R-1	123.10	1.27
15R-3	126.10	1.21
16R-1	132.70	1.55
16R-3	135.70	1.39
16R-5	138.70	1.74
17R-1	142.30	1.43
17R-3	144.90	1.27
18R-1	152.00	1.32
18R-3	155.00	1.48
18R-5	157.60	1.54
19R-1	161.65	1.27
20R-1	171.35	1.42
20R-3	174.35	1.11
20R-5	177.35	1.33
21R-1	181.05	1.17
21R-3	184.00	1.40
21R-5	187.05	1.15
22R-1	190.65	1.33
22R-3	193.65	1.47
22R-5	196.65	1.15
23R-1	200.25	1.41
23R-3	203.25	1.12
23R-5	206.15	1.46
23R-7	208.90	1.05
42R-1	383.50	1.53
24R-1	209.95	1.37
24R-3	212.95	1.32
24R-5	215.95	1.38
25R-1	219.55	1.34
25R-3	222.55	1.32
25R-5	225.55	1.40
26R-1	229.00	1.35
26R-3	231.88	1.37
26R-5	234.66	1.47
27R-1	238.64	1.63
27R-3	241.79	1.37
27R-5	244.79	1.47
28R-1	248.48	1.43
28R-3	251.60	1.29
28R-5	254.48	1.73
29R-1	258.20	1.37
29R-3	260.73	1.47
29R-5	262.98	1.50
30R-1	267.69	1.35
30R-3	270.68	1.23
30R-5	273.72	1.37
31R-1	277.40	1.53
31R-3	280.40	1.36
31R-5	283.45	1.46
32R-1	287.15	1.54
32R-3	289.75	1.37
32R-5	292.25	1.41
33R-1	296.75	1.71
33R-3	299.75	1.39
33R-5	302.75	1.45
34R-1	306.30	1.40
34R-3	309.30	1.54
35R-1	316.05	1.43
35R-3	319.05	1.39
35R-5	321.55	1.46
36R-1	325.65	1.60
36R-3	328.60	1.63
36R-5	331.65	1.38
37R-1	335.25	1.36
37R-3	338.20	1.38
37R-5	341.25	1.39
38R-1	344.90	1.42
38R-3	347.90	1.47
39R-1	354.34	1.46
39R-3	356.97	1.41
39R-5	360.50	1.74
40R-1	364.17	1.69
40R-3	367.24	1.45
40R-5	370.30	1.42
41R-1	373.79	1.99
41R-3	376.79	1.62
41R-5	379.07	1.66
42R-1	383.50	1.53
44R-3	406.33	1.24
44R-5	408.34	1.36
45R-1	412.75	1.39
45R-3	415.57	1.34
45R-5	419.02	1.88
46R-1	422.31	1.57
46R-5	428.50	1.79
47R-1	431.85	1.56
47R-3	434.59	1.40
48R-2	442.45	1.75
48R-4	446.40	1.76
50R-1	460.39	1.50
50R-5	466.66	1.75
51R-1	470.67	1.47
51R-3	473.59	1.42
51R-5	476.66	1.43
52R-1	480.11	1.46
52R-3	482.96	1.44
52R-3	483.05	1.66
53R-1	489.46	1.58
53R-3	492.38	1.61
53R-5	495.37	1.56
54R-3	502.34	1.41
56R-1	518.77	1.27
56R-3	521.20	1.35
56R-5	524.05	1.53
57R-1	528.35	1.35
57R-3	531.45	1.55
57R-5	534.30	1.64
58R-1	538.18	1.51
58R-3	541.26	1.21
59R-1	547.65	1.29
59R-3	550.35	1.24
60R-1	557.60	1.24
60R-3	560.40	1.87
60R-5	563.15	1.65
80R-1	749.16	1.72
81R-1	759.23	2.68
82R-2	770.00	2.05
82R-2	770.47	2.62
82R-4	772.98	2.03
83R-3	776.97	2.91
84R-1	778.19	2.03
84R-3	781.06	2.02
85R-3	789.70	2.22
85R-5	792.42	2.13
85R-6	794.24	2.35

Quality of Logs

The wire-line heave compensator was used during all logging runs; sea conditions were calm with minimal swell.

The quality of the sonic waveforms from the monopole transmitters for both passes generally was good, except for the shear waves. Real-time slowness-time coherence processing, however, proved problematic for all waveforms, resulting in unreliable P-wave velocity computations in both sections. This was observed as the "skipping" in delta T (velocities) in Figures 45 and 46; shore-based processing will be required to improve these data. The amplitude of the recorded signals from the dipole transmitter in both logged sections was very low, thereby rendering the shear-wave data in the upper, "softer," logged interval useless. Shear-wave data from the lower

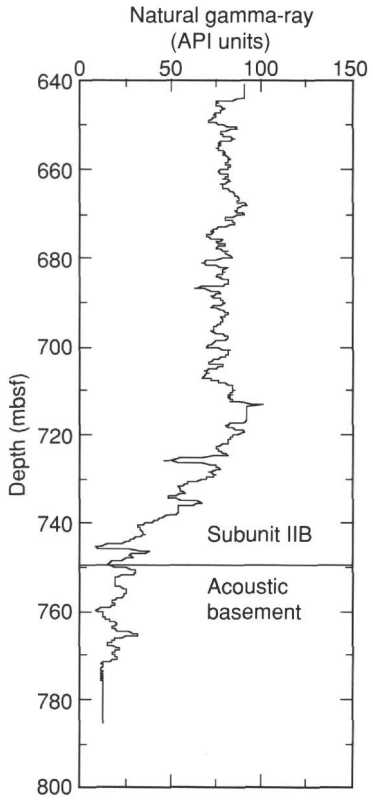

Figure 47. Natural gamma-ray data from the third run through the base of Subunit IIB and into basement (interval at 640-800 mbsf). A five-point linear moving-average filter was applied to these data.

section will require careful processing to obtain useful shear-wave velocities. Resistivity data from the induction phaser tool are good, and the correlation among shallow, medium, and deep resistivity over the interval also is good.

The quality of FMS data was poor in the lower pass, because the tool had problems with fully opening its arms and contacting the borehole wall. Good data were obtained from the second run between 646 and 731 mbsf. Good natural gamma-ray data were acquired from both passes and have been combined in Figure 47.

Depth Shifting

No intervals of the hole were logged with more than one tool string, so depth shifting of the logs is not necessary.

Logging Results

Interval at 137-238 mbsf

This section has natural gamma-ray values that range from 35 to 70 API units. The section has a uniform resistivity that averages 1.5 Ωm and tentative estimates of P-wave interval transit time are on the order of 160 to 175 µs/ft (1.7-1.9 km/s), all of which are typical of a sequence of relatively unconsolidated sediments. A slight peak in the natural gamma-ray log at 180 mbsf corresponds to the boundary between Units I and II in Core 149-900A-21R. The DSI sonic tool indicates a poor shear-wave response from the dipole source, which indicates both weak dipole source energy from the DSI and a poorly consolidated sedimentary formation.

Interval at 330-451 mbsf

This interval has constant values of natural gamma-ray and resistivity (a mean of 70-75 API and 1.5 Ωm, respectively). Tentative first estimates of P-wave interval transit time are on the order of 150 µs/ft (2.0 km/s). The log data suggest that the lithology in this section is similar to that of the upper section. A slightly higher natural gamma-ray value suggests a small change in lithology, although resistivity appears unchanged.

Interval at 646-785 mbsf

Natural gamma-ray data over this interval show a marked decrease from a high average of 80 API units above 710 mbsf, through a transitional zone (710-740 mbsf) to a low average of 15 API units below 740 mbsf. This corresponds to the change from the basal sedimentary Subunit IIB to acoustic basement; the contact is located somewhere between 740 and 750 mbsf. Given the nature of the acoustic basement, this sediment/basement contact probably is a sharp contact at the very base of the transitional zone. The transitional zone is likely to be the result of the change from the dominant clayey lithology of Subunit IIB to the sandy basal sediments, as observed in the cores. FMS data show that the hole is deviated (from vertical) by 12° through the basement section (azimuth 272°). In the section immediately above, the basement deviation is seen to decrease relatively steadily from 12° to 8° (azimuth 272°-273°) at the top of the logged interval.

INTEGRATION OF SEISMIC PROFILES WITH OBSERVATIONS FROM THE SITE

Two multichannel seismic-reflection profiles were obtained across the site before the cruise. Lusigal Line 12 crosses the site in an east-west direction (Fig. 1) and Sonne Line 75-21 crosses the site in a north-south direction (Fig. 3). The profiles indicate a number of sedimentary reflectors that have been recognized on a regional scale in the vicinity of the Iberia Abyssal Plain; these have been dated by tracing them back to Leg 103 sites west of Galicia Bank (Mauffret and Montadert, 1988) and to Site 398 near Vigo Seamount (Groupe Galice, 1979). One of these reflectors, which separates acoustic formations 1B and 2 (Groupe Galice, 1979; Fig. 1), crosses the site. The reflection profile across the site is also characterized by two unusual acoustic facies in the interval between 0.58 s two-way traveltime and the seabed. The interval from 0 to 0.38 s two-way traveltime consists of hummocky sediment waves, and the interval from 0.38 to 0.58 s two-way traveltime consists of a series of inclined reflectors (Fig. 1).

Downhole sonic logs were obtained at Site 900 over just two intervals: between 137 and 238 and from 330 to 451 mbsf. This was insufficient to compute the depths of seismic reflectors. However, the results of two sonobuoy lines shot over the Iberia Abyssal Plain (Whitmarsh, Miles, and Mauffret, 1990) were used to convert from two-way traveltime to depth (Fig. 66, "Site 897" chapter, this volume). Thus, we were able to estimate the downhole depths of the 1B/2 and basement reflectors seen in the Lusigal 12 seismic-reflection profile and the depths downhole of the two acoustic facies described above. These are summarized in Table 17.

1. The hummocky sediment wave and the inclined reflector acoustic facies both lie within the 515-m-thick Subunit IIB (see "Lithostratigraphy" section, this chapter). The sediments of Subunit IIB show signs of reworking by contour currents, as well as some mud turbidites and contourites. No marked lithological variations are evident within Subunit IIB, but the appearance of thin beds of hard calcite-cemented sandstone in most cores below 296 mbsf, although much more closely spaced than the wavelength of the seismic energy, may well be the explanation for the pattern of inclined reflectors observed between 0.38 and 0.58 s two-way traveltime. Were the top of these reflectors to correlate with the top of the sandstones, then the interval velocity would be 1.59 km/s. This may not be the full explanation, however, because the sandstone beds occur well below the depth of the base of the inclined reflectors. Other explanations may exist for these reflectors that remain to be investigated.

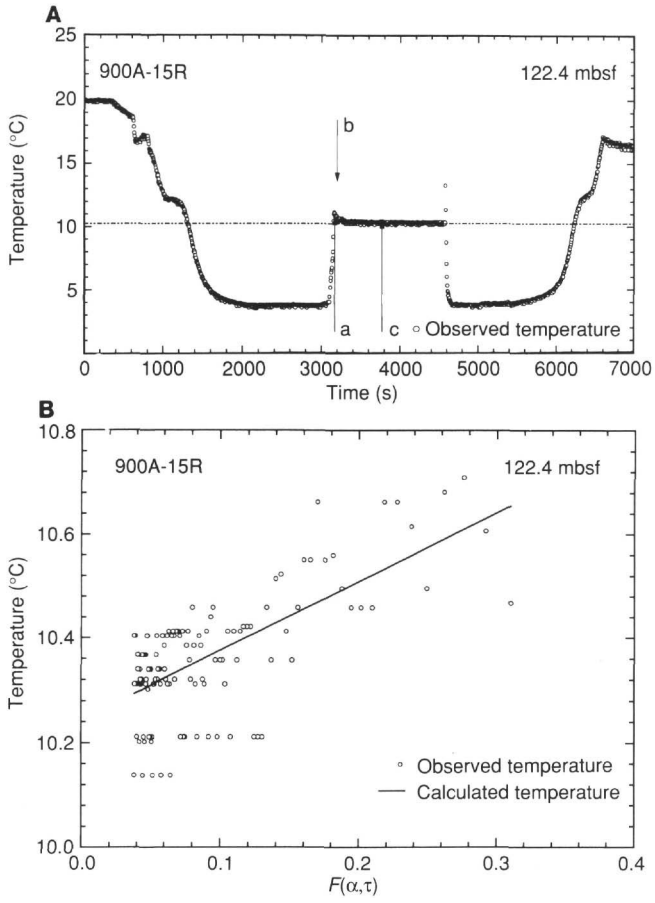

Figure 48. WSTP deployment at 122.4 mbsf in Hole 900A. **A**. Observed temperature as a function of time. The bottom-water temperature is interpreted to be 3.8 ± 0.1 °C, and the in-situ temperature is interpreted to be 10.2 ± 0.1 °C. The insertion time used for curve fitting is indicated by arrow a. The portion of the temperature data used in the extrapolation is between arrows b and c. **B**. Observed temperature plotted against Bullard's "F" function (Bullard, 1954). The quality of the temperature extrapolation is reflected in the linearity of the plotted data.

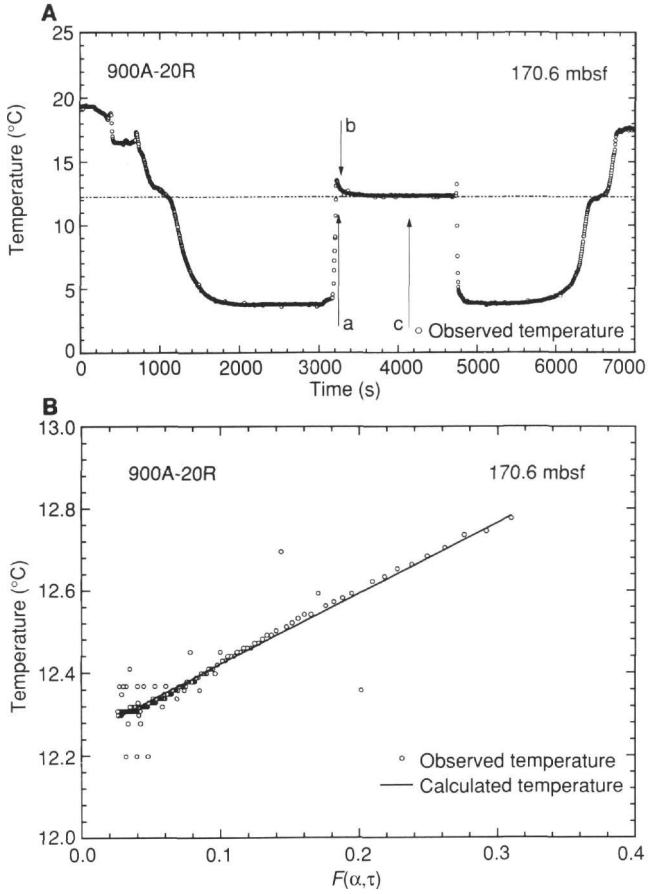

Figure 49. WSTP deployment at 170.6 mbsf in Hole 900A. **A**. Observed temperature as a function of time. The bottom-water temperature has been interpreted to be 3.8 ± 0.1 °C, and the in-situ temperature has been interpreted to be 12.2 ± 0.1°C. The insertion time used for curve fitting is indicated by arrow a. The portion of the temperature data used in the extrapolation is between arrows b and c. **B**. Observed temperature plotted vs. Bullard's "F" function (Bullard, 1954). The quality of the temperature extrapolation is reflected in the linearity of the plotted data.

2. Reflector R1 (Table 17) was computed as being at 540 mbsf. No clear explanation for the R1 reflector exists in terms of a lithologic or physical change at this depth.

3. The acoustic basement reflector was computed as being at a depth of 770 mbsf. It correlates with the top of the sequence of metamorphosed mafic igneous rock encountered at 748.9 mbsf. The computed interval velocity from 0 to 748.9 mbsf is 1.87 km/s.

IN-SITU TEMPERATURE MEASUREMENTS

A WSTP tool was deployed to collect in-situ temperature data at 122.4, 170.6, and 218.7 mbsf in Hole 900A (WSTP depth is based on the depth of the bottom of the previous cored interval). The general shape of the temperature vs. time curves for each deployment suggests that the tools were inserted in a single movement and were stationary during the measurements. The individual temperature measurements showed much more scatter about the typical cooling curve than is usual (Figs. 48B-50B). We suspect that this was a problem with the tool, but do not think that it renders the measurements invalid.

Analyses of the WSTP measurements at 122.4 mbsf, obtained immediately prior to Core 149-900A-15R, yielded a bottom-water temperature of 3.8 ± 0.1°C and an in-situ temperature of 10.2 ± 0.1°C (Fig. 48). The bottom-water temperature was obtained by averaging temperature readings between 2400 and 2900 s, when the tool had stopped just above the seafloor. The in-situ temperature was estimated by using 3171 s as the insertion time and by modeling the temperature decay over the interval from 3202 to 3770 s.

Analyses of the WSTP measurements at 170.6 mbsf, obtained immediately prior to Core 149-900A-20R, yielded a bottom-water temperature of 3.8 ± 0.1°C and an in-situ temperature of 12.2 ± 0.1°C (Fig. 49). The bottom-water temperature was obtained by averaging temperature readings between 2000 and 2200 s, when the tool had stopped just above the seafloor. The in-situ temperature was estimated by using 3250 s as the insertion time and by modeling the temperature decay over the interval from 3281 to 4150 s.

Analyses of the WSTP measurements at 218.7 mbsf, obtained immediately prior to Core 149-900A-25R, yielded a bottom-water temperature of 3.8 ± 0.1°C and an in-situ temperature of 14.4 ± 0.1°C (Fig. 50). The bottom-water temperature was obtained by averaging temperature readings between 2200 and 2400 s, when the tool had stopped just above the seafloor. The in-situ temperature was estimated by using 3198 s as the insertion time and by modeling the temperature decay over the interval from 3289 to 4023 s.

The slope of a linear least-squares fit of the temperature to depth (Table 18) yields an estimate of 49 ± 3 mK/m (95% confidence level)

Table 17. Depths of reflectors in Hole 900A.

Reflector	Time (s TWT)	Computed depth (mbsf)	Estimated depth (mbsf)	Origin of reflector
Hummocky sed. waves	0.00–0.38	0–355	0–296	
Inclined reflectors	0.38–0.58	355–540	296–?	Dipping sandstone beds
R1	0.58	540	?	late Eocene
Basement	0.80	770	749	Top of series of mafic rocks; interval velocity 1.87 km/s

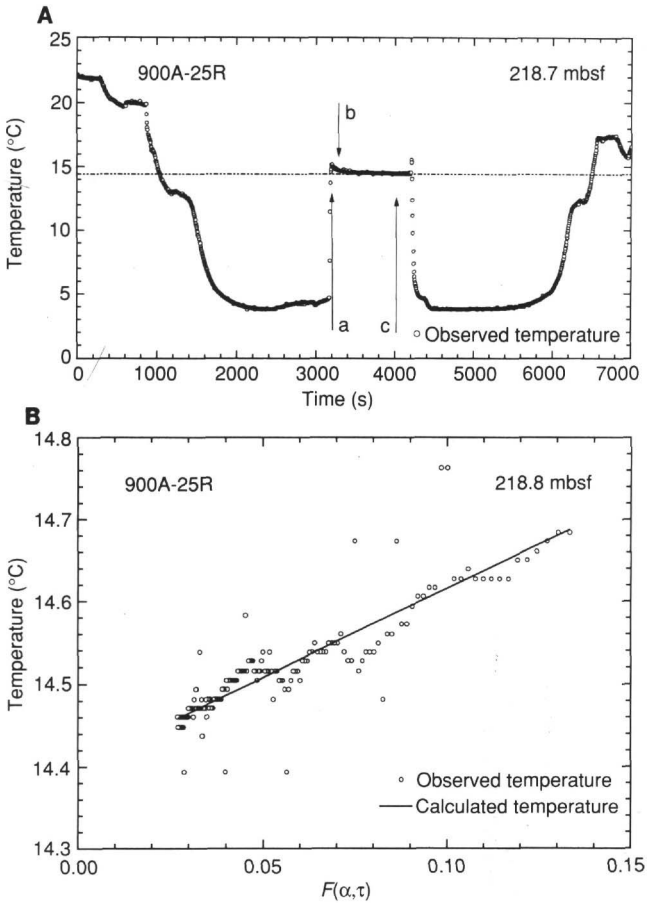

Figure 50. WSTP deployment at 218.7 mbsf in Hole 900A. **A**. Observed temperature as a function of time. The bottom-water temperature was interpreted to be 3.8 ± 0.1°C, and the in-situ temperature was interpreted to be 14.4 ± 0.1 °C. The insertion time used for curve fitting is indicated by arrow a. The portion of the temperature data used in the extrapolation is between arrows b and c. **B.** Observed temperature plotted vs. Bullard's "F" function (Bullard, 1954). The quality of the temperature extrapolation is reflected in the linearity of the plotted data.

for the temperature gradient in the upper 218 mbsf at Site 900. The slope of a linear least-squares fit of the temperature to vertically integrated thermal resistivity (Table 18), yields an estimate of 59 ± 8 mW/m^2 (95% confidence level) for the heat flow (see "Explanatory Notes" chapter, this volume).

SUMMARY AND CONCLUSIONS

Site 900 is situated in the Iberia Abyssal Plain over a roughly circular basement high (Fig. 2 in "Site 897," this volume) within the presumed ocean/continent transition (OCT) zone off western Iberia (see "Introduction" chapter, this volume). The site is one of a transect

Table 18. WSTP temperature measurements and vertically integrated thermal resistivity in Hole 900A.

Depth (mbsf)	Temperature (°C)	Vertically integrated thermal resistivity (m^2 K/W)
0	3.8 ± 0.1	0
122.4	10.2 ± 0.1	107.4
170.6	12.2 ± 0.1	142.4
218.7	14.4 ± 0.1	180.0

of drill sites across the OCT designed to study the petrologic changes in the basement rocks within the OCT as a means of identifying the processes that accompanied continental breakup and the onset of steady-state seafloor spreading. The site is in a region of weakly magnetized, presumed thinned continental crust (see Fig. 4 in "Introduction" chapter, this volume). An RCB hole was drilled with the primary scientific objective of penetrating basement to a depth sufficient to firmly establish its character. The hole was drilled and cored to 805 mbsf and passed through Pleistocene to late Paleocene age sediments and 56 m of mafic igneous rock. Coring was terminated when the rate of penetration slowed to 1 m/hr and bit failure was imminent. A total of 380 m of sonic, resistivity, and FMS logs was acquired from three separate intervals in the sediments and basement.

The first event in the history of Site 900, which we can deduce from the cores, is the formation of the mafic igneous rock that now forms the basement here. At present, we can only speculate about the origin of this rock. It may be (1) cumulate gabbro (of any pre-late Paleocene age) either formed in, or possibly underplated at the base of, continental crust, or (2) pre-Mesozoic mafic rock involved in the Hercynian orogeny and later incorporated in the passive margin. The rock subsequently experienced a series of deformation and metamorphic events. The rock has a well-marked foliation, which attests to high-temperature shear deformation. This was followed by retrograde metamorphism to low-grade amphibolite or greenschist facies. An ensuing lower-temperature deformation is expressed in narrow shear zones, fractures and veins, and brecciation. The density of the basement rocks is about 2.6 to 2.9 g/cm^3; their velocity ranges from 3.7 to 7.5 km/s, with a cluster of observations at 5.7 km/s. One effect of the metamorphism seems to have been the virtual destruction of any remanent magnetization.

Preliminary comparison with basement rocks from Sites 897 and 899 suggests that this tectono-metamorphic evolution may be common to each site, although the primary lithologies are different. Finally, the metamorphosed mafic igneous rocks were exposed at the seafloor prior to the late Paleocene, probably by the Early Cretaceous rifting.

The sediments cored at this site reveal a late Paleocene to Pleistocene history of sedimentation on an evolving continental margin, starting with predominantly contour current reworking of turbidites, followed by the dominance of turbidite deposition from the middle Miocene onward. Sedimentation over this interval ranged between 13 and 27 m/m.y.

From the late Paleocene until the early Miocene, a sequence of clay or silt with nannofossil clay was deposited. Sedimentation was interrupted for about 7 m.y. during the early Eocene. An important characteristic of these sediments is the presence of upward-darkening sequences. These range in thickness from 10 to 30 cm, usually have sharp bases and tops, and are intensely bioturbated. These features and

small-scale structures in the cores point to reworking by contour currents. At the same time, evidence of downslope sediment movement can be seen in the form of scattered mud turbidites. A series of calcite-cemented sandstones, deposited until the earliest Miocene, may represent a combination of turbidity and contour-current deposition. Above a fault of unknown displacement in the early Miocene sequence, possibly the result of synsedimentary deformation, upward-lightening sequences appear that are indicative of turbidite deposition. Pervasive bioturbation indicates deposition above the CCD.

The sequence from the early Miocene to the Pleistocene is principally nannofossil clay and ooze. The turbidites were dominated by mud, and sandy bases are uncommon. The turbidite bases are mostly siliciclastic, but occasionally carbonate-rich, suggesting two distinct provenances. Turbidite deposition ceased from late Miocene to late Pliocene. Bioturbation is pervasive. A 4.0-m.y. hiatus, beginning in the middle Miocene (around 12 Ma), correlates with a regional angular unconformity in seismic-reflection profiles; this may be related to northwest-southeast compression on this margin during a compressional phase in the Betic Mountains in southern Spain and structural inversion in the Lusitanian Basin of Portugal.

Until more work is done on the basement rocks from this site, it is not possible to recognize the extent to which they will contribute to our understanding of the ocean/continent transition on this margin. Post-cruise studies may be expected to produce new understanding of these complex rocks.

REFERENCES*

Beslier, M.-O., Ask, M., and Boillot, G., 1993. Ocean-continent boundary in the Iberia Abyssal Plain from multichannel seismic data. *Tectonophysics,* 218:383-393.

Boyce, R.E., 1973. Physical properties—methods. *In* Edgar, N.T., Saunders, J.B., et al., *Init. Repts. DSDP,* 15: Washington (U.S. Govt. Printing Office), 1115-1128.

Bullard, E.C., 1954. The flow of heat through the floor of the Atlantic Ocean. *Proc. R. Soc. London A,* 222:408-429.

Capdevila, R., and Mougenot, D., 1988. Pre-Mesozoic basement of the western Iberian continental margin and its place in the Variscan Belt. *In* Boillot, G., Winterer, E.L., et al., *Proc. ODP, Sci. Results,* 103: College Station, TX (Ocean Drilling Program), 3-12.

Claypool, G.E., and Kvenvolden, K.A., 1983. Methane and other hydrocarbon gases in marine sediment. *Annu. Rev. Earth Planet. Sci,* 11:299-327.

Emerson, S., and Hedges, J.I., 1988. Processes controlling the organic carbon content of open ocean sediments. *Paleoceanography,* 3:621-634.

Espitalié, J., Madec, M., Tissot, B., Mennig, J.J., and Leplat, P., 1977. Source rock characterization method for petroleum exploration. *Proc. 9th Annu. Offshore Technol. Conf,* 3:439-48.

Folk, R.L., 1980. *Petrology of Sedimentary Rocks:* Austin (Hemphill Publ.).

Gealy, E.L., 1971. Saturated bulk density, grain density, and porosity of sediment cores from the western Equatorial Pacific: Leg 7, *Glomar Challenger. In* Winterer, E.L., Riedel, W.R., et al., *Init. Repts. DSDP,* 7 (Pt. 2), Washington (U.S. Govt. Printing Office), 1081-1104.

Gieskes, J.M., 1974. Interstitial water studies, Leg 25. *In* Simpson, E.S.W., Schlich, R., et al., *Init. Repts. DSDP,* 25: Washington (U.S. Govt. Printing Office), 361-394.

————, 1983. The chemistry of interstitial waters of deep-sea sediments: interpretation of deep-sea drilling data. *In* Riley, J.P., and Chester, R. (Eds.), *Chemical Oceanography* (Vol. 8): London (Academic Press), 222-269.

Groupe Galice, 1979. The continental margin off Galicia and Portugal: acoustical stratigraphy, dredge stratigraphy and structural evolution. *In* Sibuet, J.-C., Ryan, W.B.F., et al., *Init. Repts. DSDP,* 47 (Pt. B): Washington (U.S. Govt. Printing Office), 633-662.

Keen, C.E., and de Voogd, B., 1988. The continent-ocean boundary at the rifted margin off eastern Canada: new results from deep seismic reflection studies. *Tectonics,* 7:107-124.

Martini, E., 1971. Standard Tertiary and Quaternary calcareous nannoplankton zonation. *In* Farinacci, A. (Ed.), *Proc. 2nd Int. Conf. Planktonic Microfossils Roma:* Rome (Ed. Tecnosci.), 2:739-785.

Mauffret, A., and Montadert, L., 1988. Seismic stratigraphy off Galicia. *In* Boillot, G., Winterer, E.L., et al., *Proc. ODP, Sci. Results,* 103: College Station, TX (Ocean Drilling Program), 13-30.

McIver, R., 1975. Hydrocarbon occurrence from JOIDES Deep Sea Drilling Project. *Proc. Ninth Petrol. Congr.,* 269-280.

Meyers, P.A., in press. Preservation of source identification of sedimentary organic matter during and after deposition. *Chem. Geol.*

Müller, P. J., 1977. C/N ratios in Pacific deep sea sediments: effect of inorganic ammonium and organic nitrogen compounds sorbed by clays. *Geochim. Cosmochim. Acta,* 41:765-776.

Rio, D., Fornaciari, E., and Raffi, I., 1990. Late Oligocene through early Pleistocene calcareous nannofossils from western equatorial Indian Ocean (Leg 115). *In* Duncan, R.A., Backman, J., Peterson, L.C., et al., *Proc. ODP, Sci. Results,* 115: College Station, TX (Ocean Drilling Program), 175-235.

Rio, D., Raffi, I., and Villa, G., 1990. Pliocene-Pleistocene calcareous nannofossil distribution patterns in the Western Mediterranean. *In* Kastens, K.A., Mascle, J., et al., *Proc. ODP, Sci. Results,* 107: College Station, TX (Ocean Drilling Program), 513-533.

Sibuet, J.-C, Ryan, W.B.F., et al., 1979. *Init. Repts. DSDP,* 47(Pt. 2): Washington (U.S. Govt. Printing Office), 25-233.

Stow, D.A.V., and Piper, D.J.W., 1984. Deep-water fine-grained sediments: facies models. *In* Stow, D.A.V., and Piper, D.J.W. (Eds.), *Fine-grained Sediments: Deep-Water Processes and Facies:* Oxford (Blackwell), 15:611-645.

Suess, E., 1980. Particulate organic carbon flux in the oceans—surface productivity and oxygen utilization. *Nature,* 288:260-263.

Tucholke, B.E., Austin, J.A., and Uchupi, E., 1989. Crustal structure and rift-drift evolution of the Newfoundland Basin. *In* Tankard, A.J., and Balkwell, H.R. (Eds.), *Extensional Tectonics and Stratigraphy of the North Atlantic Margins.* AAPG Mem., 46.

Whitmarsh, R.B., Miles, P.R., and Mauffret, A., 1990. The ocean-continent boundary off the western continental margin of Iberia, I. Crustal structure at40°30'N. *Geophys. J. Int.,* 103:509-531.

Whitmarsh, R.B., Pinheiro, L.M., Miles, PR., Recq, M., and Sibuet, J.C, 1993. Thin crust at the western Iberia ocean-continent transition and ophiolites. *Tectonics,* 12:1230-1239.

*Abbreviations for names of organizations and publication titles in ODP reference lists follow the style given in *Chemical Abstracts Service Source Index* (published by American Chemical Society).

Ms 149IR-107

NOTE: For all sites drilled, core-description forms ("barrel sheets") and core photographs have been reproduced on coated paper and can be found in Section 3, beginning on page 271. Forms containing smear-slide data can be found in Section 4, beginning on page 657. Thin-section data are given in Section 5, beginning on page 679. GRAPE, Index Property and MAGSUS data are presented on CD-ROM (back pocket).

Hole 900A: Resistivity-Natural Gamma Ray Log Summary

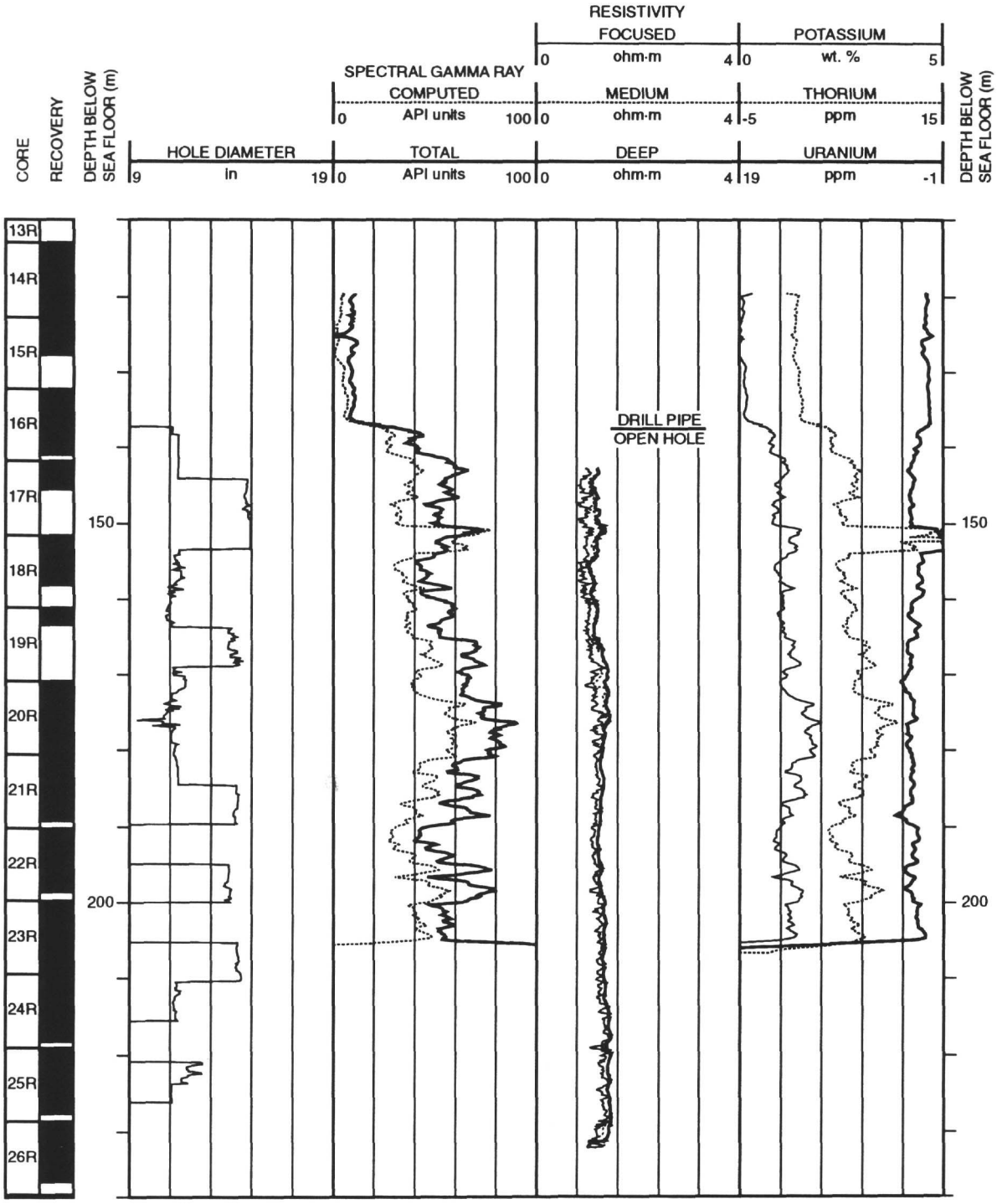

Note: These data were reprocessed post-cruise by the Borehole Research Group, Lamont-Doherty Earth Observatory of Columbia University.

Hole 900A: Resistivity-Natural Gamma Ray Log Summary (continued)

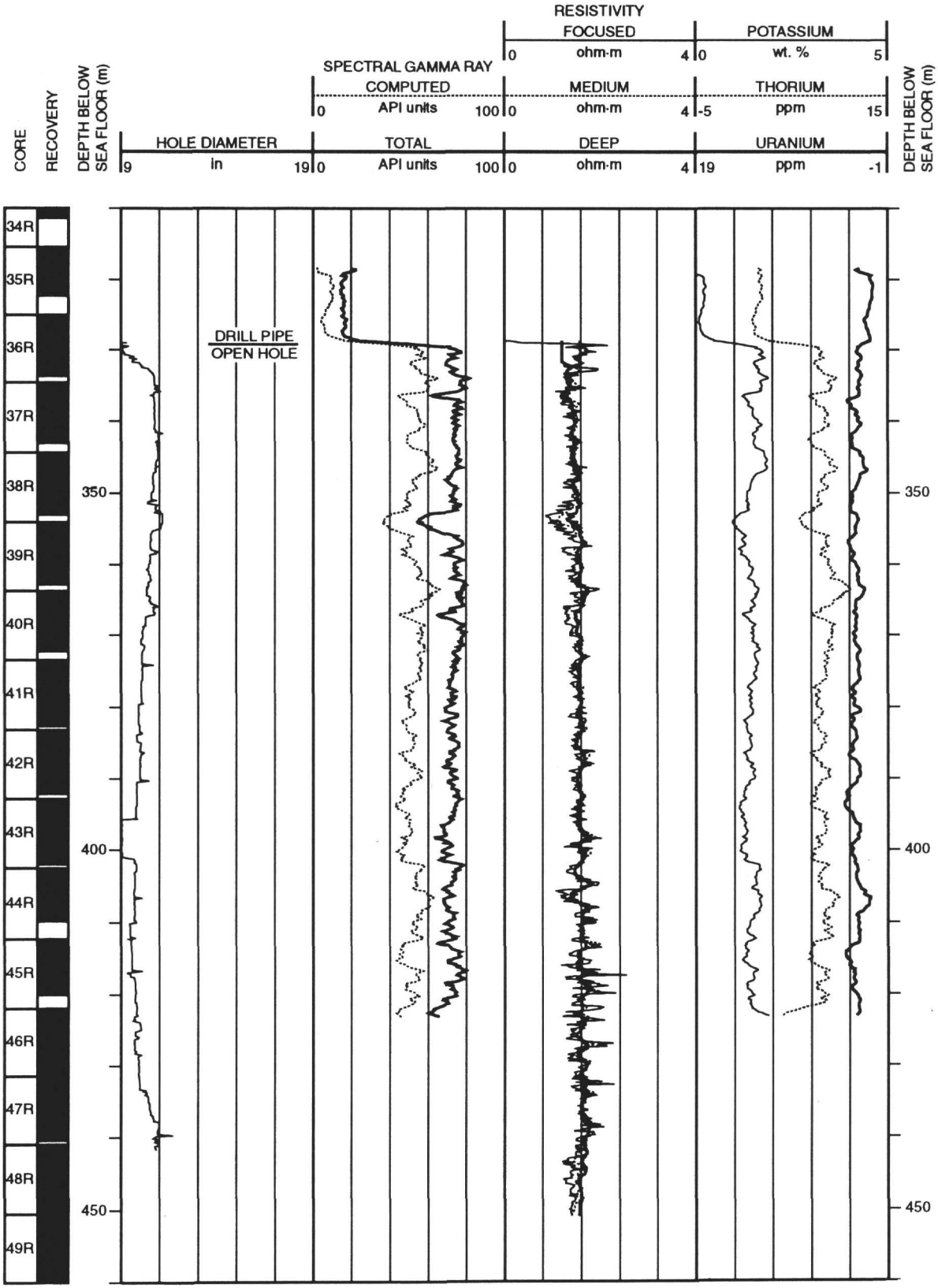

Hole 900A: Natural Gamma Ray Log Summary (continued)